Self-assembly of noble metal monolayers on transition metal carbide nanoparticle catalysts

Citation: Hunt, S. T., M. Milina, A. C. Alba-Rubio, C. H. Hendon, J. A. Dumesic, and Y. Roman-Leshkov. "Self-Assembly of Noble Metal Monolayers on Transition Metal Carbide Nanoparticle Catalysts." Science 352, no. 6288 (May 19, 2016): 974–978.

As Published: http://dx.doi.org/10.1126/science.aad8471

Publisher: American Association for the Advancement of Science (AAAS)

Persistent URL: http://hdl.handle.net/1721.1/103123

Version: Author's final manuscript: final author's manuscript post peer review, without publisher's formatting or copy editing

Self-assembly of noble metal monolayers on transition metal carbide nanoparticle catalysts

Sean T. Hunt[1], Maria Milina[1], Ana C. Alba-Rubio[2†], Christopher H. Hendon[1], James A. Dumesic[2], Yuriy Román-Leshkov[1]*

Affiliations:
[1]Department of Chemical Engineering, Massachusetts Institute of Technology, Cambridge, MA 02139, USA.
[2]Department of Chemical and Biological Engineering, University of Wisconsin-Madison, Madison, WI 53706, USA.
[†]Current Address: Department of Chemical and Environmental Engineering, University of Toledo, Toledo, OH 43606, USA.
*Correspondence to: yroman@mit.edu

Abstract: We demonstrate the self-assembly of transition metal carbide nanoparticles coated with atomically-thin noble metal monolayers by carburizing mixtures of noble metal salts and transition metal oxides encapsulated in removable silica templates. This approach allows for control of the final core-shell architecture, including particle size, monolayer coverage, and heterometallic composition. Carbon-supported $Ti_{0.1}W_{0.9}C$ nanoparticles coated with Pt or bimetallic PtRu monolayers exhibited enhanced resistance to sintering and CO poisoning, achieving an order of magnitude increase in specific activity over commercial catalysts for methanol electrooxidation after 10,000 cycles. These core-shell materials provide a new direction to reduce the loading, enhance the activity, and increase the stability of noble metal catalysts.

One Sentence Summary: The self-assembly of transition metal carbide nanoparticles coated with atomically-thin noble metal monolayers results in a highly active, stable, and tunable catalytic platform.

Noble metal (NM) catalysts critically enable many existing and emerging technologies, such as catalytic converters (*1*), reforming (*2*), and fuel cells (*3*). However, their scarcity and high cost necessitate the development of catalytic systems with reduced NM loadings, increased activity, and improved durability. In this respect, various nanostructured architectures have been investigated, including atomically-dispersed NM catalysts (*4*), hollow nanocages (*5, 6*), alloyed nanoparticles (NPs) (*7*), and core-shell structures (*8, 9*). In particular, core-shell NPs composed of an earth-abundant core coated with an atomically-thin NM shell are a promising platform that offers both design flexibility and reduced precious metal loadings. However, achieving independent control over the particle size, core composition, shell composition, and shell thickness poses a substantial challenge (*8, 9*). State-of-the-art synthetic methods are predominantly limited to a few earth-abundant metallic cores (e.g., Fe, Co, Ni, and Cu) that allow for more precise synthetic control; however, these metal cores form intrinsically metastable core-shell particles that restructure during heating (*10-12*) or electrochemical cycling (*13, 14*).

Early transition metal carbides (TMCs) are earth-abundant ceramics with ideal topochemical properties for supporting precious metal shells (*15*-*17*). First, TMCs exhibit metallic electrical conductivity, corrosion resistance, and high melting points (*18*). Second, precious metals tend to bind strongly to metal-terminated early TMC surfaces (Fig. S1), but cannot readily form stable carbides (*19*). Thus, NMs should coat TMC surfaces, but should not alloy with the underlying core. In particular, tungsten carbide (WC) is inexpensive (Fig. S2), exhibits a "platinum-like" density of electronic states (*20*, *21*), and its metal-terminated surface forms interfacial Pt-WC bonds that are ca. 90 kJ mol^{-1} stronger than interfacial Pt-Pt bonds (Fig. S1). Although experimental studies on model thin film systems have corroborated these attractive properties (*15*, *22*, *23*), synthetic efforts to date have not achieved TMC NPs coated with NM monolayers. Until recently, TMC NPs alone were difficult to engineer with controlled properties because their synthesis requires high temperatures (above ca. 700˚C) followed by passivation with dilute oxygen (*24*). Without proper synthetic control, these conditions result in sintered TMC particles covered in both graphitic coke and an oxide surface layer. Such surface impurities preclude core-shell formation because of the unfavorable binding energies between precious metals and contaminated TMC surfaces (Fig. S1).

We present here a high temperature self-assembly method to synthesize size-tunable TMC NPs (<10 nm) coated with monometallic or heterometallic NM surface shells of controlled thicknesses ranging from submonolayer to multilayer coverages. These core-shell materials achieve superior catalytic activity, improved stability, and reduced NM loadings compared to state-of-the-art commercial catalysts for electrochemical applications. They are also sinter-resistant, and the core-shell structure remains stable at high temperatures under various atmospheres.

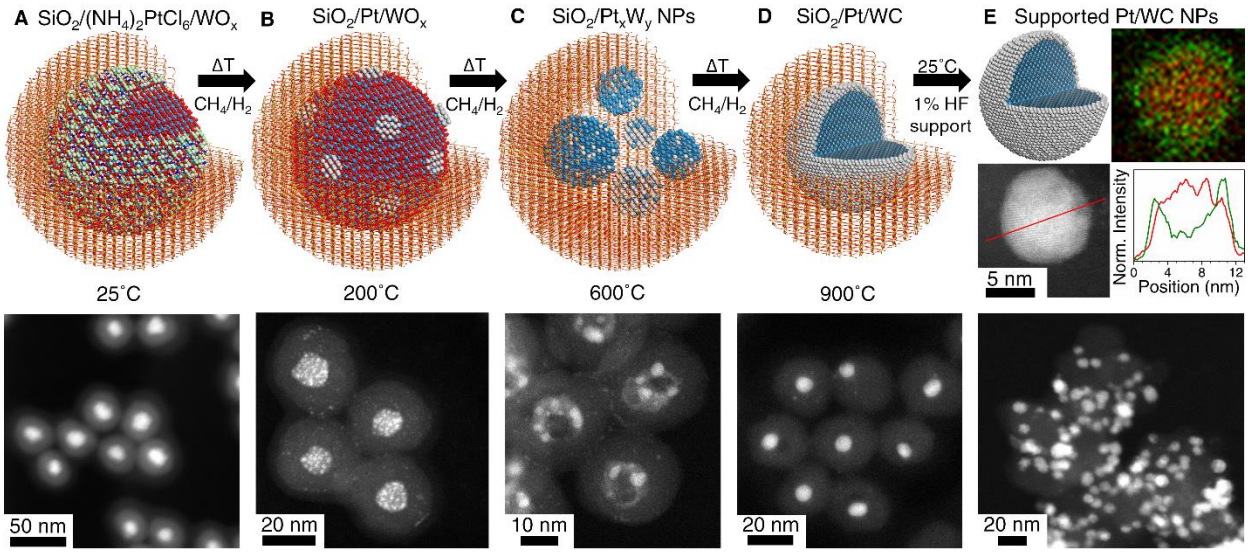

Fig. 1. High temperature self-assembly of NM monolayers on TMC cores. (**A** to **D**) Schematic representations and corresponding STEM images of (A) silica-encapsulated $(NH_4)_2PtCl_6/WO_x$ NPs synthesized in a one-pot reactor at room temperature and subsequently heated to (B) 200˚C, (C) 600˚C, and (D) 900˚C in a CH_4/H_2 atmosphere. (**E**) STEM image, EDX map, and linescan (Pt signal in green, W signal in red) of a resulting core-shell Pt/WC NP and a STEM image of Pt/WC formulated on a carbon black support after silica removal.

Aberration-corrected scanning transmission electron microscopy (STEM) images (Fig. 1) depict the stages of the NM/TMC (shell/core) self-assembly process as a function of temperature, with Pt/WC NP formation as the representative example. In the first step, WO_x NPs were impregnated uniformly with a $(NH_4)_2PtCl_6$ salt and encapsulated in silica NPs via a room-temperature reverse microemulsion (RME) (Fig. 1A). This method generated $SiO_2/(NH_4)_2PtCl_6/WO_x$ composites with controlled NP size and Pt loading [see Supporting Information for comprehensive synthetic details (*25*)].

The $SiO_2/(NH_4)_2PtCl_6/WO_x$ composites were then subjected to a temperature ramp under a 15% CH_4/85% H_2 flow (Fig. 1, B to D). At temperatures lower than 200˚C, H_2 permeated through the silica nanospheres (*24*), reducing the encapsulated Pt salt into Pt nanoclusters over the WO_x domains (Fig. 1B and Fig. S3). By 600˚C, the central WO_x NPs underwent reduction, forming metallic mixtures of Pt and W that are trapped within the silica NPs (Fig. 1C and Figs. S3 and S4). Near 900˚C, these small metallic clusters sintered to form single central NPs while carbon from methane decomposition intercalated into the W-rich domains, forming WC (Fig. 1D). Because NMs are insoluble in TMC lattices, Pt phase-segregates from the WC domains and wets the central carbide core as an atomically-thin shell, resulting in the self-assembly of uniform core-shell NPs (Fig. 1E) as determined by an energy-dispersive x-ray spectroscopy (EDX) map and linescan. The silica template was dissolved, and the resulting NPs could then be dispersed in solution with or without a capping agent (Fig. S5) or onto a high-surface-area matrix (Fig. 1E). The final Pt/WC particle size and Pt shell thickness were controlled by engineering the WO_x NP size and $(NH_4)_2PtCl_6$ loading in the RME prior to silica encapsulation and carburization.

Silica encapsulation is critical for controlling core-shell NP formation. In Fig. 2, A to C, we compare two carbon-supported NM/TMC materials, one with silica encapsulation (denoted as $Pt_{C\text{-}S}$, 28%Pt/72%$Ti_{0.1}W_{0.9}C$ supported at 28 wt%), and the other without silica encapsulation (denoted as Pt_{direct}, 20%Pt/80% $Ti_{0.1}W_{0.9}C$ supported at 20 wt%). Because TiC is the most electrochemically stable carbide (*26*), a bimetallic TiWC core was used to enhance stability without affecting the WC lattice parameter by more than 1%. The powder x-ray diffraction (PXRD) pattern for $Pt_{C\text{-}S}$ shows reflections consistent with phase-pure face-centered cubic (fcc) WC (PDF #00-020-1316) without additional fcc Pt reflections (PDF #00-004-0802), whereas the pattern for Pt_{direct} exhibits distinct, sintered fcc Pt crystallites (Fig. 2A). These data are consistent with core-shell formation for $Pt_{C\text{-}S}$ but Pt phase-segregation for Pt_{direct}. In addition, $Pt_{C\text{-}S}$ showed a difference between the bulk and surface Pt:TiW ratios (28% vs. 49% as determined by inductively coupled plasma mass spectrometry [ICP] and x-ray photoelectron spectroscopy [XPS], respectively). This surface ratio enhancement is indicative of Pt monolayers screening a TiW-rich core. In contrast, such surface screening was not observed for Pt_{direct} where the bulk and surface Pt:TiW ratios were 20% and 18%, respectively.

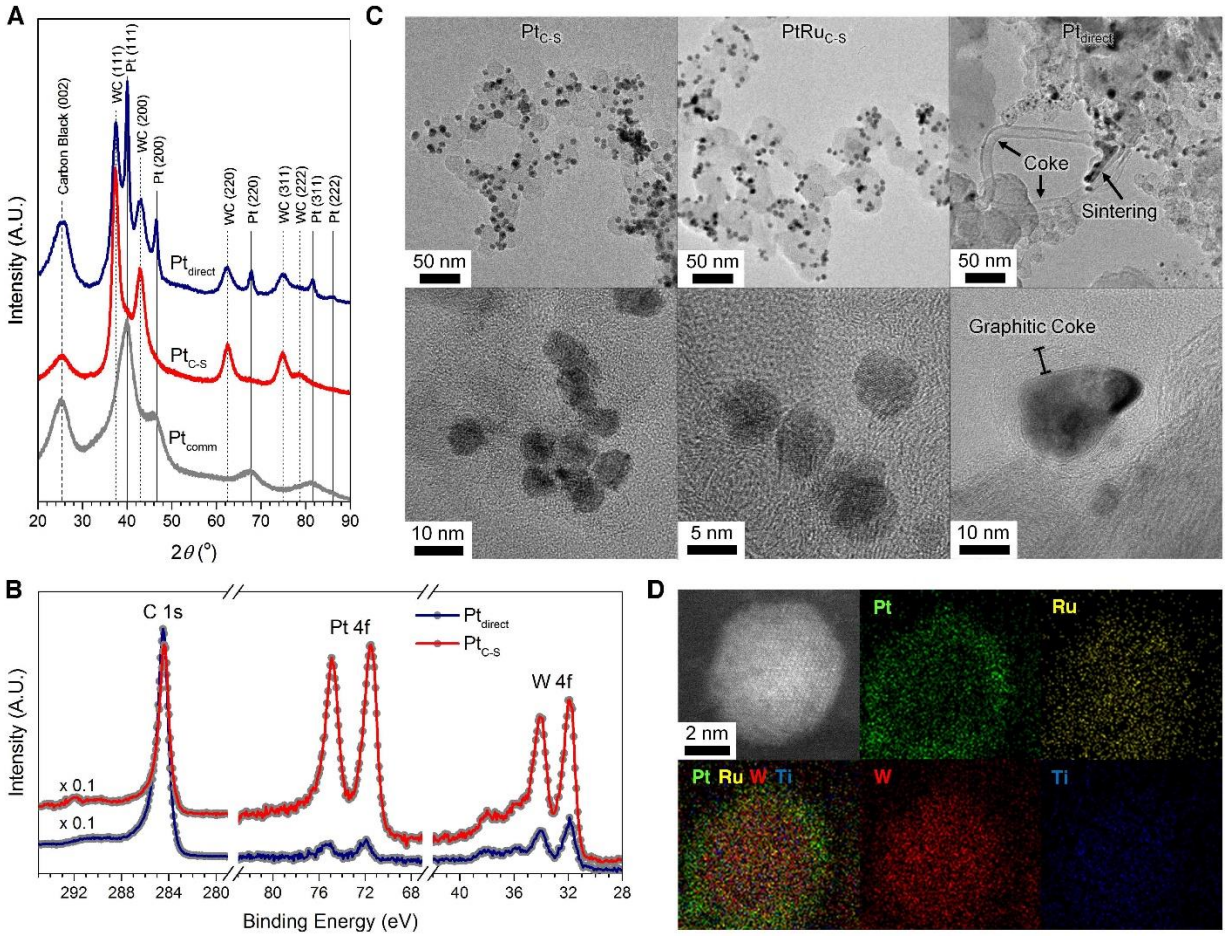

Fig. 2. Experimental corroboration of core-shell structure. (**A**) PXRDs of $Pt_{C\text{-}S}$ and Pt_{direct} compared to Pt_{comm}. (**B**) XPS comparison of the C 1s, Pt 4f, and W 4f signals of $Pt_{C\text{-}S}$ and Pt_{direct}. (**C**) TEM images of $Pt_{C\text{-}S}$, $PtRu_{C\text{-}S}$, and Pt_{direct}. (**D**) STEM and EDX maps of $PtRu_{C\text{-}S}$.

Silica encapsulation prevented undesirable coking during carburization, as verified by a 6-fold lower carbon-to-metal surface ratio for $Pt_{C\text{-}S}$ compared to Pt_{direct} (Fig. 2B). Characteristic graphitic coke fibrils and sintered particles encapsulated in 4 to 5 nm of graphitic coke are visible in the transmission electron microscopy (TEM) images of Pt_{direct} (Fig. 2C). In contrast, $Pt_{C\text{-}S}$ shows well-dispersed crystalline NPs with a uniform particle size distribution (PSD) of 6 to 8 nm and the absence of detectable coke layers. A heterometallic $27\%Pt_{0.67}Ru_{0.33}/73\%Ti_{0.1}W_{0.9}C$ material (denoted as $PtRu_{C\text{-}S}$) was synthesized analogously to $Pt_{C\text{-}S}$ (Fig. 2C and Figs. S6-8). Although Ru could partition into the carbide core because it is less noble than Pt, STEM-EDX mapping (Fig. 2D) and XPS (Fig. S7) show a core-shell structure with an Ru-enriched surface.

We compared the electrocatalytic properties of $Pt_{C\text{-}S}$ and $PtRu_{C\text{-}S}$ (8 wt% NM) to 20 wt% carbon-supported commercial (Premetek) electrocatalysts, denoted as Pt_{comm} and $PtRu_{comm}$, using gas diffusion electrodes (GDEs) (Fig. 3A) and rotating disk electrodes (RDEs) (Fig. 3, B to E). Carbon monoxide stripping voltammetry was used to determine the electrochemically active surface area (CO-ECSA) and roughness factors of all materials (Table S1, Fig. S9). Both Pt_{comm} and $PtRu_{comm}$ consist of 1 to 3 nm NPs (Fig. S10) and have high CO-ECSAs of $68\pm6\ m^2\ g^{-1}_{NM}$

and 99±7 $m^2\ g^{-1}_{NM}$, respectively. Despite having larger PSDs (6 to 8 nm) than the commercial samples, both $Pt_{C\text{-}S}$ and $PtRu_{C\text{-}S}$ achieve comparable CO-ECSAs of 50±2 $m^2\ g^{-1}_{NM}$ and 73±2 $m^2\ g^{-1}_{NM}$, respectively. Pt_{direct} did not exhibit a measureable CO-ECSA (Fig. S9) and behaved analogously to carbon during cycling from 0.025 V to 1 V (Fig. S11).

The reactivity and stability of $Pt_{C\text{-}S}$ and $PtRu_{C\text{-}S}$ were characterized by using density functional theory (DFT) and various probe reactions including hydrogen evolution (HER), hydrogen oxidation (HOR), HOR under CO contamination, and methanol electrooxidation (MOR). Both $Pt_{C\text{-}S}$ and $PtRu_{C\text{-}S}$ exhibited improved specific activity for HER and HOR, indicating that TiWC cores are excellent supports for NM monolayers and can favorably alter catalytic activity. Despite a 60% reduction in NM loading, $Pt_{C\text{-}S}$ and $PtRu_{C\text{-}S}$ exhibited a symmetric activity profile during HER and HOR linear sweep voltammetry (LSV), similar to that for the commercial catalysts (Fig. 3A). Both core-shell materials exhibited HER and HOR Tafel slopes of ca. 30 mV dec^{-1} even after 10,000 cycles between -50 and 600 mV (Table S2 and Figs. S12 and S13). At an HER overpotential of 50 mV, both core-shell materials show a 4-fold improvement in specific activity and a 3-fold improvement in mass activity over the commercial catalysts (Table S3) and maintain this enhancement after cycling.

Enhanced catalytic activity was corroborated by DFT calculations for thermally equilibrated Pt/TiWC slabs. Specifically, our calculations show Fermi level matching with Pt, which translates to minimal alterations to the work function of surface Pt by subsurface TiWC (*27*) (Figs. S14 and S15), but show that the d-band center for a two-monolayer Pt shell downshifts from -2.7 to -2.8 eV (Fig. S16). This downshift provides access to potentially favorable surface properties, such as a substantial weakening of the CO binding energy by ca. 40 kJ mol^{-1} (*28*). In turn, this effect can increase the tolerance of $Pt_{C\text{-}S}$ and $PtRu_{C\text{-}S}$ toward CO poisoning, thereby overcoming a major challenge afflicting the performance of industrial Pt-based catalysts in many electrochemical applications (*11, 28*).

Indeed, HOR experiments performed in the presence of high CO concentrations confirm that the TiWC cores mitigate poisoning on Pt and PtRu monolayers. Specifically, while 1000 ppm of CO contamination markedly increased the HOR onset potential by ca. 400 mV for $PtRu_{comm}$ (Fig. 3B) and by ca. 200 mV for a state-of-the-art Pt/PtSn catalyst (*29*), both $Pt_{C\text{-}S}$ and $PtRu_{C\text{-}S}$ catalyze HOR with an overpotential as low as 50 mV. Under pure CO, both $Pt_{C\text{-}S}$ and $PtRu_{C\text{-}S}$ achieved a ca. 200 mV lower onset potential and a 30-fold enhancement in specific activity for CO electrooxidation at 400 mV when compared to the commercial catalysts (Fig. S17).

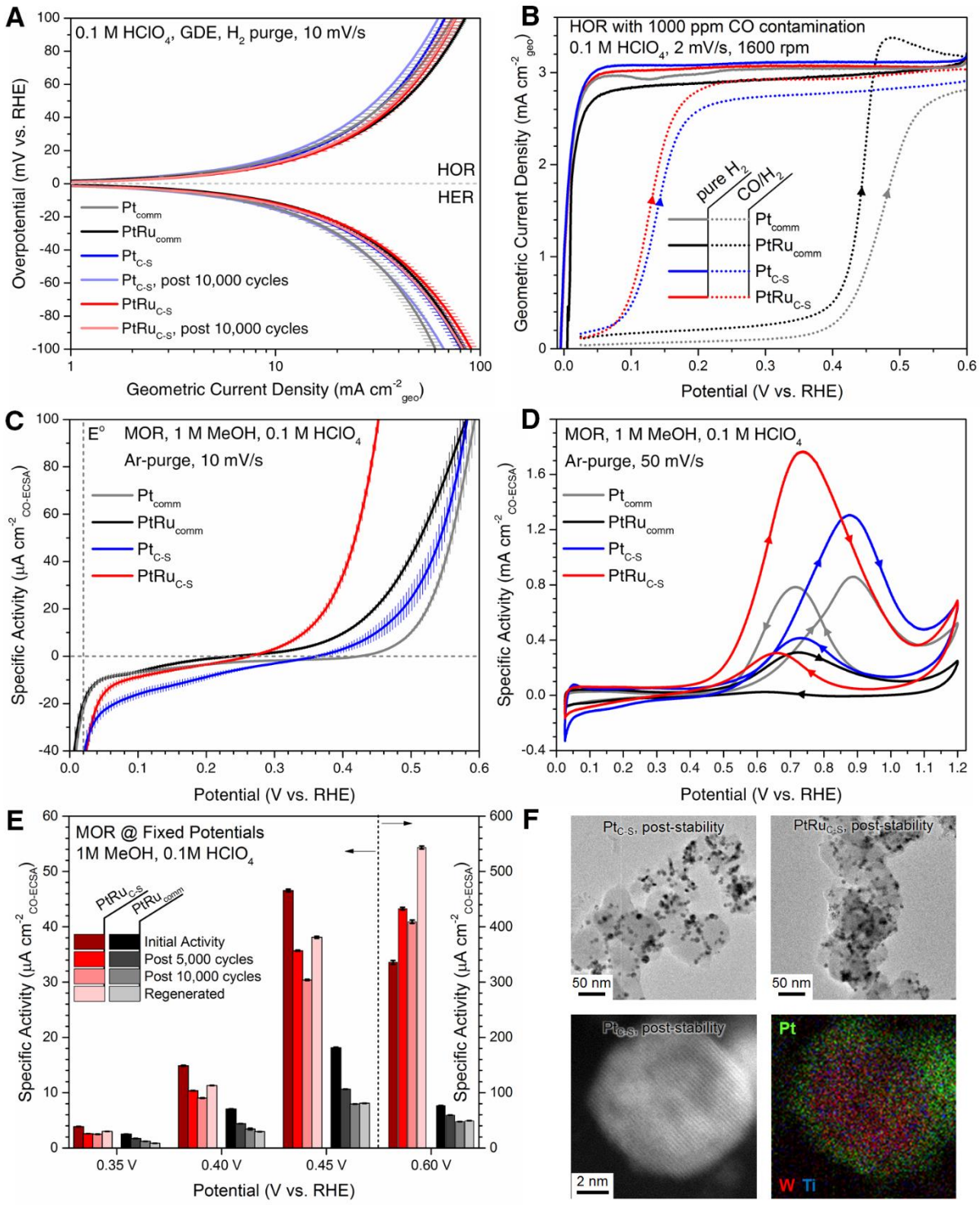

Fig. 3. Electrochemical activity and stability of $Pt_{C\text{-}S}$ and $PtRu_{C\text{-}S}$ compared to commercial catalysts. (**A**) HOR/HER Tafel plots (**B**) HOR LSVs with and without CO contamination. (**C**) LSVs and (**D**) CVs for MOR normalized by CO-ECSA roughness factors. (**E**) Steady-state specific activity at fixed potentials after stability cycling and regeneration in alkaline media. (**F**) TEM images of $Pt_{C\text{-}S}$ and $PtRu_{C\text{-}S}$ and a STEM image with EDX map of a $Pt_{C\text{-}S}$ NP after stability cycling.

By decreasing the CO binding strength, the TiWC core is responsible for enhancing the MOR kinetics observed for $Pt_{C\text{-}S}$ compared to Pt_{comm}. The former features a higher specific activity over a wide potential window and a ca. 100 mV lower onset potential than Pt_{comm} (Fig. 3C, D and Fig. S18). Ru is known to improve the MOR performance of Pt at low overpotentials via a bifunctional mechanism (*30*). Despite extensive efforts in the literature, little improvement in the activity and durability of MOR catalysts has been achieved over commercial PtRu/C in acidic media (*31*). Whereas both $PtRu_{C\text{-}S}$ and $PtRu_{comm}$ achieve a low onset potential of ca. 250 mV, $PtRu_{C\text{-}S}$ displays a higher steady-state turnover frequency (TOF) of 15.9 min^{-1} at 0.6 V compared to 3.6 min^{-1} using $PtRu_{comm}$ (Table S4), further evidencing the favorable activity modulation achievable using a TiWC core.

$PtRu_{C\text{-}S}$ also demonstrates enhanced stability compared to $PtRu_{comm}$ (Fig. 3E and Figs. S19 and S20). After 10,000 cycles, $PtRu_{comm}$ lost more than 50% of its steady-state activity at 0.35, 0.40, and 0.45 V, whereas the $PtRu_{C\text{-}S}$ activity decreased by only 35% at these potentials and actually improved at 0.6 V. Notably, a simple 2 min alkaline dip partially regenerated the activity of $PtRu_{C\text{-}S}$ at all potentials, but had no appreciable benefit for $PtRu_{comm}$. Specifically, after regeneration, the overall loss in activity at 0.45 V was 18% and 55% for $PtRu_{C\text{-}S}$ and $PtRu_{comm}$, respectively. The final TOF at 0.6 V after 10,000 cycles and regeneration was 25.7 min^{-1} for $PtRu_{C\text{-}S}$, 2.4 min^{-1} for $PtRu_{comm}$, 1.8 min^{-1} for $Pt_{C\text{-}S}$, and 1.1 min^{-1} for Pt_{comm} (Table S4), which represents an order of magnitude improvement of our core-shell material over the commercial catalysts.

No appreciable deactivation via particle sintering was observed for the core-shell materials after 10,000 cycles (Fig. 3F). HR-STEM and EDX mapping of $Pt_{C\text{-}S}$ after stability cycling show a highly crystalline composite NP with an intact Pt shell and a well-alloyed TiWC core (Fig. 3F and Fig. S21). We attribute the improved stability of the core-shell materials to the strong NM-TMC interfacial bonds and to the lower surface free energies of large NPs relative to the surface free energies of ultra-small NPs. These results demonstrate the ability of our method to reformulate a classic bimetallic NM catalyst, such as PtRu, into an architecture that preserves the complexity of the original bimetallic surface chemistry while favorably modulating catalytic performance through subsurface strain and ligand effects. As a class of materials that breaks the traditional metal-adsorbate scaling relations for transition metals (*32*), TMCs not only serve as promising core candidates to reduce NM loadings, but could favorably impact catalytic activity for industrially-relevant reactions, such as HOR, MOR, water-gas shift, or methanol synthesis wherein CO coverage effects deeply influence catalyst performance.

Remarkably, the high temperature self-assembly process used here permits comprehensive control of the entire core-shell architecture for a variety of early and late transition metals (Fig. 4). Using TiWC cores, we synthesized NPs of controlled sizes (3 to 10 nm) with mono- and bimetallic shell compositions using mixtures of Ru, Rh, Ir, Pt, and Au (Fig. 4A and Figs. S22-S24). All materials crystallized into fcc WC lattices and displayed enhanced surface NM:TiW ratios, consistent with core-shell structures (Figs. S25-S27 and Table S5). In addition, NM shells lattice-matched and self-assembled onto bimetallic semicarbide cores (PDF #00-020-1315) such as $(Cu_{0.2}W_{0.8})_2C$, $(Co_{0.2}W_{0.8})_2C$, and $(Ni_{0.3}W_{0.7})_2C$ (Fig. 4B, C, Figs. S28 and S29). While NM interfacial bond formation and stability is not explored on all possible TMC

core formulations, our data suggest broader applicability of the method for synthesizing a variety of NM/TMC combinations.

For Au, Pt, and PtAu monolayers self-assembled on TiWC cores, the RME method also allowed control of the NM shell thickness from sub-monolayer (ca. 0.5 ML) to multilayer (ca. 3 ML) coverages (Fig. 4D). For each material, the extent of the XPS-determined surface NM:TiW ratio enhancement over the ICP-determined bulk NM:TiW ratio correlated with the monolayer coverage, ranging from 1 to 3% at submonolayer coverages to 10 to 20% screening at multilayer coverages (Table S5). Unlike Au surfaces, the surface of Pt passivates under ambient conditions with a PtO layer, which is detectable as Pt^{2+} with XPS. As the monolayer coverage decreased for the Pt/TiWC system (Fig. 4D, spectra f to d), the Pt 4f signals shifted to higher binding energies, reaching 72.3 and 75.7 eV for the submonolayer sample (denoted as $Pt_{sub\text{-}ML}$). The presence of only PtO is consistent with submonolayer coverage, and such materials could have important applications in thermal catalysis where both WC and Pt surface functionalities are accessible for catalytic transformations. Notably, when $Pt_{sub\text{-}ML}$ was supported on carbon and heated to 400˚ and 600˚C in different atmospheres (H_2, dry N_2, or H_2O-saturated N_2), neither sintering nor discrete fcc Pt crystallites were detectable using TEM and PXRD, and an enriched Pt:W ratio showing only Pt^{2+} surface species was observed with XPS (Figs. S30-S33). Collectively, TMC NPs coated with NM monolayers offer new, highly tunable pathways for decreasing NM loading requirements while increasing activity and stability in thermo- and electrocatalysis.

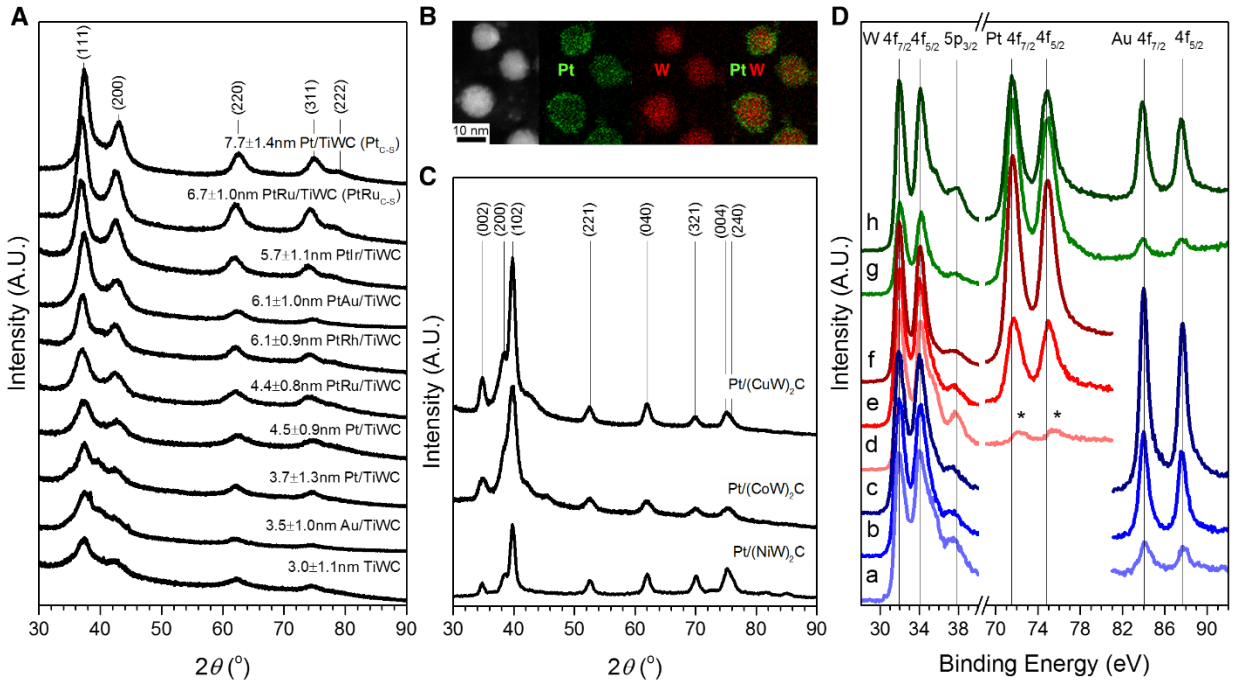

Fig. 4. Experimental exploration of various core-shell NM/TMC architectures. (**A**) PXRD diffractograms of NM/TiWC NPs of various sizes, compositions, and NM coverages. (**B**) STEM image and EDX maps of carbon-supported Pt/$(CuW)_2C$ NPs. (**C**) PXRD diffractograms of Pt monolayers on various bimetallic semicarbide core NPs. (**D**) XPS spectra of (a-c) Au/TiWC NPs, (d-f) Pt/TiWC NPs, and (g,h) PtAu/TiWC NPs with submonolayer, monolayer, and multilayer NM shell thicknesses. The * in panel D marks the Pt^{2+} signal

Supplementary Materials

Materials and Methods
Fig. S1 to S33
Table S1 to S5
References (33-61)

References and Notes:

1. A. T. Bell, The impact of nanoscience on heterogeneous catalysis. *Science* **299**, 1688-1691 (2003).
2. G. A. Deluga, J. R. Salge, L. D. Schmidt, X. E. Verykios, Renewable hydrogen from ethanol by autothermal reforming. *Science* **303**, 993-997 (2004).
3. J. Zhang, K. Sasaki, E. Sutter, R. R. Adzic, Stabilization of platinum oxygen-reduction electrocatalysts using gold clusters. *Science* **315**, 220-222 (2007).
4. Y. Zhai *et al.*, Alkali-stabilized Pt-OHx species catalyze low-temperature water-gas shift reactions. *Science* **329**, 1633-1636 (2010).
5. L. Zhang *et al.*, Platinum-based nanocages with subnanometer-thick walls and well-defined, controllable facets. *Science* **349**, 412-416 (2015).
6. C. Chen *et al.*, Highly crystalline multimetallic nanoframes with three-dimensional electrocatalytic surfaces. *Science* **343**, 1339-1343 (2014).
7. J. Greeley *et al.*, Alloys of platinum and early transition metals as oxygen reduction electrocatalysts. *Nature Chem.* **1**, 552-556 (2009).
8. P. Strasser *et al.*, Lattice-strain control of the activity in dealloyed core-shell fuel cell catalysts. *Nat Chem* **2**, 454-460 (2010).
9. H. Yang, Platinum-based electrocatalysts with core–shell nanostructures. *Angew. Chem. Int. Ed.* **50**, 2674-2676 (2011).
10. F. Tao *et al.*, Reaction-driven restructuring of Rh-Pd and Pt-Pd core-shell nanoparticles. *Science* **322**, 932-934 (2008).
11. S. Alayoglu, A. U. Nilekar, M. Mavrikakis, B. Eichhorn, Ru-Pt core-shell nanoparticles for preferential oxidation of carbon monoxide in hydrogen. *Nat. Mater.* **7**, 333-338 (2008).
12. C. S. Bonifacio *et al.*, Thermal stability of core–shell nanoparticles: a combined in situ study by XPS and TEM. *Chem. Mater.* **27**, 6960-6968 (2015).
13. C. Cui, L. Gan, M. Heggen, S. Rudi, P. Strasser, Compositional segregation in shaped Pt alloy nanoparticles and their structural behaviour during electrocatalysis. *Nat. Mater.* **12**, 765-771 (2013).
14. C. Wang *et al.*, Correlation between surface chemistry and electrocatalytic properties of monodisperse PtxNi1-x nanoparticles. *Adv. Funct. Mater.* **21**, 147-152 (2011).
15. D. V. Esposito, J. G. Chen, Monolayer platinum supported on tungsten carbides as low-cost electrocatalysts: opportunities and limitations. *Energy Environ. Sci.* **4**, 3900-3912 (2011).
16. I. E. Stephens, A. S. Bondarenko, U. Grønbjerg, J. Rossmeisl, I. Chorkendorff, Understanding the electrocatalysis of oxygen reduction on platinum and its alloys. *Energy Environ. Sci.* **5**, 6744-6762 (2012).
17. J. A. Schaidle, N. M. Schweitzer, O. T. Ajenifujah, L. T. Thompson, On the preparation of molybdenum carbide-supported metal catalysts. *J. Catal.*, (2012).

18. S. T. Oyama, *The Chemistry of Transition Metal Carbides and Nitrides*. (Blackie, Glasgow, 1996).
19. S. Ono, T. Kikegawa, Y. Ohishi, A high-pressure and high-temperature synthesis of platinum carbide. *Solid State Commun.* **133**, 55-59 (2005).
20. R. B. Levy, M. Boudart, Platinum-like behavior of tungsten carbide in surface catalysis. *Science* **181**, 547-549 (1973).
21. L. H. Bennett, J. R. Cuthill, A. J. McAlister, N. E. Erickson, R. E. Watson, Electronic structure and catalytic behavior of tungsten carbide. *Science* **184**, 563-565 (1974).
22. D. V. Esposito, S. T. Hunt, Y. C. Kimmel, J. G. Chen, A new class of electrocatalysts for hydrogen production from water electrolysis: metal monolayers supported on low-cost transition metal carbides. *J. Am. Chem. Soc.* **134**, 3025-3033 (2012).
23. T. G. Kelly, A. L. Stottlemyer, H. Ren, J. G. Chen, Comparison of O−H, C−H, and C−O bond scission sequence of methanol on tungsten carbide surfaces modified by Ni, Rh, and Au. *J. Phys. Chem. C* **115**, 6644-6650 (2011).
24. S. T. Hunt, T. Nimmanwudipong, Y. Roman-Leshkov, Engineering non-sintered, metal-terminated tungsten carbide nanoparticles for catalysis. *Angew. Chem. Int. Ed.* **53**, 5131-5136 (2014).
25. See supporting material on *Science* Online.
26. Y. C. Kimmel, X. Xu, W. Yu, X. Yang, J. G. Chen, Trends in electrochemical stability of transition metal carbides and their potential use as supports for low-cost electrocatalysts. *ACS Catal.* **4**, 1558-1562 (2014).
27. W. Schottky, Über spontane stromschwankungen in verschiedenen elektrizitätsleitern. *Annalen der Physik* **362**, 541-567 (1918).
28. B. Hammer, Y. Morikawa, J. Norskov, CO chemisorption at metal surfaces and overlayers. *Phys. Rev. Lett.* **76**, 2141-2144 (1996).
29. Z. Liu, G. S. Jackson, B. W. Eichhorn, PtSn intermetallic, core-shell, and alloy nanoparticles as CO-tolerant electrocatalysts for H2 oxidation. *Angew. Chem. Int. Ed. Engl.* **49**, 3173-3176 (2010).
30. T. J. Schmidt, H. A. Gasteiger, R. J. Behm, Methanol electrooxidation on a colloidal PtRu-alloy fuel-cell catalyst. *Electrochem. Commun.* **1**, 1-4 (1999).
31. A. K. Singh, Q. Xu, Synergistic catalysis over bimetallic alloy nanoparticles. *ChemCatChem* **5**, 652-676 (2013).
32. R. Michalsky, Y. J. Zhang, A. J. Medford, A. A. Peterson, Departures from the adsorption energy scaling relations for metal carbide catalysts. *J. Phys. Chem. C* **118**, 13026-13034 (2014).
33. S. T. Hunt, T. M. Kokumai, D. Zanchet, Y. Roman-Leshkov, Alloying tungsten carbide nanoparticles with tantalum: impact on electrochemical oxidation resistance and hydrogen evolution activity. *J. Phys. Chem. C* **119**, 13691-13699 (2015).
34. S. T. Hunt, Y. Roman-Leshkov, Reverse microemulsion-mediated synthesis of monometallic and bimetallic early transition metal carbide and nitride nanoparticles. *J. Vis. Exp.* **e53147**, (2015).
35. M. Koenig, J. Grant, Signal-to-noise measurement in X-ray photoelectron spectroscopy. *Surf. Interface Anal.* **7**, 217-222 (1985).
36. T. Schmidt *et al.*, Characterization of High-Surface-Area Electrocatalysts Using a Rotating Disk Electrode Configuration. *J. Electrochem. Soc.* **145**, 2354-2358 (1998).

37. K. Shinozaki, J. W. Zack, R. M. Richards, B. S. Pivovar, S. S. Kocha, Oxygen Reduction Reaction Measurements on Platinum Electrocatalysts Utilizing Rotating Disk Electrode Technique I. Impact of Impurities, Measurement Protocols and Applied Corrections. *J. Electrochem. Soc.* **162**, F1144-F1158 (2015).
38. K. Shinozaki, J. W. Zack, S. Pylypenko, B. S. Pivovar, S. S. Kocha, Oxygen Reduction Reaction Measurements on Platinum Electrocatalysts Utilizing Rotating Disk Electrode Technique II. Influence of Ink Formulation, Catalyst Layer Uniformity and Thickness. *J. Electrochem. Soc.* **162**, F1384-F1396 (2015).
39. T. Binninger, E. Fabbri, R. Kötz, T. Schmidt, Determination of the electrochemically active surface area of metal-oxide supported platinum catalyst. *J. Electrochem. Soc.* **161**, H121-H128 (2014).
40. K. Elbert *et al.*, Elucidating Hydrogen Oxidation/Evolution Kinetics in Base and Acid by Enhanced Activities at the Optimized Pt Shell Thickness on the Ru Core. *ACS Catal.* **5**, 6764-6772 (2015).
41. J. X. Wang, Y. Zhang, C. B. Capuano, K. E. Ayers, Ultralow charge-transfer resistance with ultralow Pt loading for hydrogen evolution and oxidation using Ru@ Pt core-shell nanocatalysts. *Sci. Rep.* **5**, 1-8 (2015).
42. G. Kresse, J. Furthmüller, Efficient iterative schemes for ab initio total-energy calculations using a plane-wave basis set. *Physical Review B* **54**, 11169-11186 (1996).
43. J. P. Perdew, K. Burke, M. Ernzerhof, Generalized Gradient Approximation Made Simple. *Phys. Rev. Lett.* **77**, 3865-3868 (1996).
44. F. Finocchi, A. Barbier, J. Jupille, C. Noguera, Stability of Rocksalt (111) Polar Surfaces: Beyond the Octopole. *Phys. Rev. Lett.* **92**, 136101 (2004).
45. D. O. Scanlon *et al.*, Surface Sensitivity in Lithium-Doping of MgO: A Density Functional Theory Study with Correction for on-Site Coulomb Interactions. *J. Phys. Chem. C* **111**, 7971-7979 (2007).
46. J. K. Nørskov *et al.*, Trends in the exchange current for hydrogen evolution. *J. Electrochem. Soc.* **152**, J23-J26 (2005).
47. K. T. Butler, C. H. Hendon, A. Walsh, Electronic Chemical Potentials of Porous Metal–Organic Frameworks. *J. Am. Chem. Soc.* **136**, 2703-2706 (2014).
48. B. Hammer, J. K. Nørskov, Electronic factors determining the reactivity of metal surfaces. *Surface Science* **343**, 211-220 (1995).
49. X. Liang, C. Jiang, Atomic layer deposited highly dispersed platinum nanoparticles supported on non-functionalized multiwalled carbon nanotubes for the hydrogenation of xylose to xylitol. *J. Nanopart. Res.* **15**, 1890 (2013).
50. Z. Yan, M. Cai, P. K. Shen, Nanosized tungsten carbide synthesized by a novel route at low temperature for high performance electrocatalysis. *Sci. Rep.* **3**, 1646 (2013).
51. I. J. Hsu, Y. C. Kimmel, X. Jiang, B. G. Willis, J. G. Chen, Atomic layer deposition synthesis of platinum-tungsten carbide core-shell catalysts for the hydrogen evolution reaction. *Chemical Comunications* **48**, 1063-1065 (2012).
52. S. Zhang *et al.*, Monodisperse Core/Shell Ni/FePt Nanoparticles and Their Conversion to Ni/Pt to Catalyze Oxygen Reduction. *J. Am. Chem. Soc.* **136**, 15921-15924 (2014).
53. "Free market commodity prices, monthly, January 1960-June 2015," United Nations Conference on Trade and Development, (2015) http://unctadstat.unctad.org/wds/TableViewer/tableView.aspx?ReportId=28768

54. "Gold Price in a Range of Currencies since December 1978," The World Gold Council, (2015) https://www.gold.org/research/download-the-gold-price-since-1978
55. "Platinum, Palladium, Rhodium, Iridium, Ruthenium Monthly Average Prices between 01 Jun 1992 and 31 Jul 2015," Johnson Matthey, (2015) http://www.platinum.matthey.com/prices/price-charts
56. S. Rudi, C. Cui, L. Gan, P. Strasser, Comparative Study of the Electrocatalytically Active Surface Areas (ECSAs) of Pt Alloy Nanoparticles Evaluated by Hupd and CO-stripping voltammetry. *Electrocatalysis* **5**, 408-418 (2014).
57. J. K. Nørskov, F. Studt, F. Abild-Pedersen, T. Bligaard, *Fundamental concepts in heterogeneous catalysis*. (John Wiley & Sons, 2014).
58. Z. Jusys, J. Kaiser, R. Behm, Composition and activity of high surface area PtRu catalysts towards adsorbed CO and methanol electrooxidation: A DEMS study. *Electrochim. Acta* **47**, 3693-3706 (2002).
59. J. Durst, C. Simon, F. Hasche, H. A. Gasteiger, Hydrogen Oxidation and Evolution Reaction Kinetics on Carbon Supported Pt, Ir, Rh, and Pd Electrocatalysts in Acidic Media. *J. Electrochem. Soc.* **162**, F190-F203 (2014).
60. C. C. McCrory *et al.*, Benchmarking Hydrogen Evolving Reaction and Oxygen Evolving Reaction Electrocatalysts for Solar Water Splitting Devices. *J. Am. Chem. Soc.* **137**, 4347-4357 (2015).
61. D. V. Esposito *et al.*, Low-cost hydrogen-evolution catalysts based on monolayer platinum on tungsten monocarbide substrates. *Angew. Chem. Int. Ed.* **49**, 9859-9862 (2010).

Acknowledgments: Work at MIT was supported by the Department of Energy, Office of Basic Energy Sciences (DE-FG02-12ER16352). This work used the Extreme Science and Engineering Discovery Environment (XSEDE), which is supported by National Science Foundation (ACI-1053575). The authors acknowledge use of facilities and instrumentation supported by the University of Wisconsin Materials Research Science and Engineering Center (DMR-1121288). S.T.H. thanks the National Science Foundation for financial support through the National Science Foundation Graduate Research Fellowship under Grant No. 1122374. M.M. thanks the Swiss National Science Foundation (Project number P2EZP2_159124) for financial support. J.A.D. acknowledges funding by the U.S. Department of Energy, Office of Basic Energy Sciences (DE-SC0014058).

Supplementary Materials for

Self-assembly of noble metal monolayers on transition metal carbide nanoparticle catalysts

Sean T. Hunt, Maria Milina, Ana C. Alba-Rubio, Christopher H. Hendon, James A. Dumesic, Yuriy Román-Leshkov*

*correspondence to: yroman@mit.edu

This PDF file includes:

Materials and Methods

Materials

Reverse microemulsions were prepared from anhydrous *n*-heptane (Sigma-Aldrich, 99%, stored under ambient conditions), polyoxyethylene (4) lauryl ether (Sigma-Aldrich, Brij® L4, average M_n ~ 362), ammonium hydroxide solution (Sigma-Aldrich, 28-30%), and deionized (DI) water (18.2 MΩ·cm). For syntheses involving the precipitation of Ir and Rh chloride salts, ammonium chloride (Sigma-Aldrich, 99.5%) was also added. Monometallic and heterometallic transition metal oxide (TMO) nanoparticles (NPs) were obtained by co-hydrolysis of commercially available metal alkoxides and metal alkoxides prepared from commercially available metal chloride salts. These consisted of tungsten (IV) chloride (Strem Chemicals, 97%) prepared with anhydrous isopropanol (IPA, Sigma-Aldrich, 99.5%), titanium (IV) isopropoxide (Sigma-Aldrich, 97%), cobalt (II) isopropoxide (Alfa Aesar), nickel (II) methoxyethoxide (Alfa Aesar, 5% w/v), and copper (II) isopropoxide (Alfa Aesar, 98%). The metal oxide NPs were coated with noble metals (NM) using as-received commercially available hydrated noble metal chloride ($NMCl_x$) salts. These consisted of ruthenium (III) chloride hydrate (Strem Chemicals, 99.9% Ru), rhodium (III) chloride hydrate (Strem Chemicals, 38-41% Rh), iridium (III) chloride hydrate (Strem Chemicals, 99.9% Ir), chloroplatinic acid (Strem Chemicals, 99.9%), and chloroauric acid (Strem Chemicals, 99.8%). The $NMCl_x$/TMO NPs were coated with silica nanospheres upon hydrolysis of tetraethyl orthosilicate (Sigma-Aldrich, 99%).

The materials were carburized in a methane/hydrogen atmosphere (Airgas, uhp grade 5). The silica shells were removed using 1% HF diluted in ethanol (200 proof) prepared from 48 wt% HF in H_2O solution (Sigma-Aldrich, 99.99% trace metals basis). The NM/TMC NPs were supported on carbon black (Cabot, Vulcan® XC-72r) or dispersed using oleylamine (Sigma-Aldrich, 70%).

Stock electrolyte solutions were prepared from DI water (18.2 MΩ·cm), perchloric acid (GFS chemicals veritas® double distilled, 70%), and methanol (Sigma-Aldrich traceSELECT®, 99.9%). The electrolyte solutions were degassed with argon (Airgas, uhp grade 5), hydrogen (Airgas, uhp grade 5), and carbon monoxide (Airgas, uhp grade 3). 0.1 M NaOH solution was prepared from DI water and NaOH pellets (Sigma-Aldrich, 99.99% trace metals basis). Commercial 20 wt% Pt (denoted as Pt_{comm}) and 20 wt% (1:1) PtRu (denoted as $PtRu_{comm}$) catalysts supported on Vulcan® were supplied by Premetek (Wilmington, DE).

Synthesis

Preparation of the tungsten alkoxide precursor: The tungsten precursor stock solution was prepared from commercial WCl_4 by addition of anhydrous isopropanol (IPA). Under constant stirring, 10 mL of anhydrous IPA was injected into a round bottom flask containing 5.0 g of WCl_4 under a continuous N_2 purge at 60˚C in a well-ventilated fume hood. Within the first minute, the grey-green WCl_4 transitioned to a purple intermediate and then to a black-brown liquid. The residual liquid was allowed to slowly evaporate at 60 ˚C under a constant N_2 purge, leaving a black-brown solid. This procedure was repeated two additional times with 20 mL of anhydrous IPA to remove any residual HCl. The final

product was diluted by addition of 100 mL of anhydrous IPA and stored under inert conditions.

Preparation of titanium, copper, and cobalt alkoxide precursors: Stock solutions of titanium (IV) isopropoxide (TiIPO), copper (II) isopropoxide (CuIPO), and cobalt (II) isopropoxide (CoIPO), were prepared by diluting the commercially available isopropoxides with anhydrous isopropanol to a final concentration of 5% w/v for TiIPO and 1% w/v for CuIPO and CoIPO. This step resulted in a slurry for CuIPO and CoIPO solutions.

Synthesis of $SiO_2/NMCl_x$/TMO NPs: A reverse microemulsion (RME) was prepared under constant stirring in ambient conditions by mixing 240 mL of *n*-heptane, 54 mL of Brij-L4® surfactant, 7.8 mL of ultrapure deionized water, and 1.4 mL of NH_4OH solution, resulting in an optically transparent and colorless RME. In the synthesis involving Ir or Rh, NH_4Cl was dissolved in ultrapure deionized water before addition into the emulsion (molar ratio of NH_4Cl to Rh or Ir = 6:1).

A metal alkoxide mixture was prepared by mixing aliquots of the metal alkoxide stock solutions in the desired ratio. Typically, 1.1 mmoles of metal alkoxides were added at this scale. Under ambient conditions without the need for a Schlenk line, the metal alkoxide mixture was diluted with 120 mL of *n*-heptane. The diluted metal alkoxide mixture was then added to the RME under constant mixing over the span of a few minutes. The RME was allowed to mix under ambient conditions for 4 h to form bimetallic transition metal oxide (TMO) NPs. During this time, the RME remained optically transparent for all syntheses, but the color varied depending on the metals used and the metal ratios. This solution will be referred to as the TMO RME. Further details on controlling the TMO NP particle size and composition is provided elsewhere (*24*, *33*, *34*).

While the TMO RME was reacting, a separate RME containing noble metal salts, further referred to as the NM RME, was prepared. Commercially available hydrated noble metal chloride salts were weighed in the desired ratios and then fully dissolved in 1 mL of ultrapure deionized water. The noble metal chloride solution was then rapidly injected to a mixture of 46 mL of *n*-heptane with 7.2 mL of Brij-L4® surfactant to obtain an optically transparent RME of various colors depending on the noble metals employed.

The NM RME was gravity-fed dropwise over ~ 30 min into the TMO RME under constant mixing to form the NM/TMO RME. After 4 h of mixing the NM/TMO RME remained optically transparent. Next, 1.5 mL of tetraethyl orthosilicate (TEOS) was added rapidly to the NM/TMO RME and allowed to react for 16.5 h. During this time, the NM/TMO RME gradually became translucent.

After 16.5 h, 300 mL of methanol was added rapidly to the RME under constant mixing to precipitate the $SiO_2/NMCl_x$/TMO NPs. After 15 min, the mixing was stopped and the $SiO_2/NMCl_x$/TMO NPs were allowed to flocculate and sediment over 1 h to form a three-phase mixture: a heptane-rich upper phase, a methanol-rich middle phase, and the SiO_2/NM/TMO NP precipitant on the bottom. The NPs were obtained by decanting off the top two layers and centrifuging the remaining slurry at 2,000 rpm. The wet cake was then redispersed in acetone to remove residual surfactant and centrifuged at 6,000 rpm. The acetone was then removed and the $SiO_2/NMCl_x$/TMO wet cake was dried under a stream of N_2. The product cake was then stored under ambient conditions. The above standard

synthesis produces ca. 600 mg of recovered SiO_2/$NMCl_x$/TMO product. For most syntheses explored in this work, all of the quantities reported above were doubled to obtain > 1 g of product.

Carburization of SiO_2/NM/TMO NPs: Approximately 500 mg of as-synthesized SiO_2/$NMCl_x$/TMO powder was spread into an alumina crucible and purged with N_2 for 30 min in a tubular furnace. The inlet gas was then switched to 130 cm^3(STP) min^{-1} of H_2 and 23 cm^3(STP) min^{-1} of CH_4. Using a 2˚C min^{-1} ramp rate, the furnace was then heated to 900˚C and held for 5 h. During the final 30 min, the flowrate of CH_4 was turned off. This final high temperature hydrogen treatment constitutes a standard scavenging step that has been shown to generate predominantly metal-terminated TMC surfaces (*22, 24*). The furnace was then allowed to cool naturally with the lid closed under 130 cm^3(STP) min^{-1} of H_2 to room temperature. Once at room temperature, the furnace was purged with N_2 bubbled through an H_2O saturator for 2 h at 95 cm^3(STP) min^{-1} and then passivated using a 1%O_2/99%N_2 mixture for 2 h. After passivation, the samples were stored in a dry N_2 glovebox.

For samples containing Ru, Rh, or Ir, the tubular furnace was heated to 1000˚C under 130 cm^3(STP) min^{-1} of H_2 and 23 cm^3(STP) min^{-1} of CH_4. Once 1000˚C was reached, the methane flow was stopped and the samples were held at 1000˚C for 30 min under 130 cm^3(STP) min^{-1} of H_2 before cooling to room temperature and passivating normally.

Removing SiO_2 to obtain NM/TMC nanodispersions or supported NM/TMC: To remove the encapsulating SiO_2 shells, ~ 60 mg of SiO_2/NM/TMC powder was added to a well-mixed solution of 10 mL of degassed ethanol and 200 µL of reagent-grade 48 wt% aqueous HF solution prepared such that the molar ratio of HF:SiO_2 was approximately 6:1. Next, 600 µL of 70% technical grade oleylamine or a high surface area support, such as carbon black, were added to obtain a nanodispersion or a supported catalyst, respectively. After 18 h at room temperature and constant mixing, the NM/TMC was recovered by centrifuging at 6,000 rpm and rinsed thoroughly with degassed ethanol and degassed water. The powder was dried under vacuum and stored in a dry N_2 glovebox.

Characterization

Transmission Electron Microscopy (TEM) and Scanning Transmission Electron Microscopy (STEM) was performed on a JEOL 2010F equipped with a field emission gun (FEG) operating at 200 kV. Magnifications of obtained images ranged from 25,000x to 600,000x. STEM was performed using high-angle annular dark field (HAADF) mode.

Aberration-Corrected STEM with EDX Mapping/Linescans was performed on an FEI equipped with a CEOS probe-side aberration corrector operated at 200 kV, with a probe convergence angle of 24.5 mrad. HAADF mode was used for imaging, with a probe current of ~ 25 pA, and spatial resolution < 0.1 nm. EDS spectrum images were taken (EDAX EDS detector, 128 eV resol.) with a probe current ~ 200-780 pA, and spatial resolution ~ 0.16-0.29 nm. Sample preparation for STEM included dispersion in ethanol or acetone, ultra-sonication for 30 min, and then deposition onto carbon copper TEM grids. STEM samples were plasma cleaned for 15 min before loading into the microscope.

X-ray Photoelectron Spectroscopy (XPS) was performed on a PHI Versaprobe II equipped with a multichannel hemispherical analyzer and a monochromatic aluminum anode X-ray source operating at 100 W with a 100 μm beam scanned over a 1.4 mm line across the sample surface. A dual-beam charge neutralization system was used with an electron neutralized bias of 1.2 eV and an argon ion beam energy of 10 eV. All spectra were charge corrected by referencing the adventitious C 1s signal to 284.7 eV. Samples were prepared by mounting powders onto electrically conductive copper tape. For unsupported nanodispersions, the nanodispersions were dispersed in DI water without the use of any ligands or capping agents. The nanodispersion was then dripped onto the copper tape and the water was evaporated under vacuum to obtain a nanoparticle thin film.

Signal-to-noise (S/N) ranged from over 300 for W 4f spectra to 70 for Ti 2p spectra. During peak deconvolution, the $\Sigma(X^2)$ was kept below 1. Peaks with S/N values below 70 could not meet this criteria, and the results from peak deconvolutions are listed as N.R. (not reported) on Table S5. We note that an S/N value greater than 3 is commonly considered a detectable peak (*35*). As such, all XPS spectra obtained were well above the detection limits of the PHI Versaprobe II.

Inductively Coupled Plasma Mass Spectrometry (ICP-MS) was performed on an Agilent 7900 ICP-MS.

Caution: Sample digestion in acidic media is extremely dangerous and should only be performed in small quantities in a well-ventilated fume hood approved for HF use. Proper PPE includes all of the following: safety glasses, full face shield, butyl rubber gloves with secondary gloves, a lab coat, and a full-body HF-resistant apron. Calcium gluconate must be readily available within an arm's reach. Aqua regia mixtures generate toxic fumes and if sealed will become pressurized.

Sample masses were averaged from triplicate measurements, with errors in the measurements of ca. ±0.02 mg. 2-3 mg samples were dissolved in a sealed polypropylene tube by adding 6 drops of reagent-grade HCl and 2 drops of reagent-grade HNO_3. After a few minutes, 6 drops of reagent-grade aqueous HF was added and the tube contents were well-mixed for 40 hours. The tubes were vented after the first 15 minutes, after 1 hour, and after 2 hours. For nanoparticles supported on carbon black, the dissolved sample was diluted with 2% HNO_3 and filtered. 1 mL of fresh aqua regia was used to rinse the filter followed by several more mL rinses with 2% HNO_3. In all cases, the final solution was diluted with 2% HNO_3 to 100-500 ppb. The detection limits for each element studied was below 100 ppt, and the R^2 value for each calibration curve always exceeded 0.999. The method for carbon-supported materials was benchmarked against total wt% loading determination using TGA. ICP and TGA agreed to less than 1% error. Mass loading errors during run-to-run replicates never exceeded 3% error.

Powder X-ray Diffraction (PXRD) was performed on a Bruker D8 diffractometer using Cu Kα radiation. Data were recorded in the range of 15-90˚ 2θ with an angular step size of 0.01˚ and a counting time of 0.1 s per step.

Thermogravimetric Analysis (TGA) was performed on a Q500 thermal analysis system (TA Instruments) between 25 and 800˚C (with 15 min isothermal hold at 150˚C) using a heating ramp of 5˚C min^{-1} under 25 sccm of air and 5 sccm of N_2 flow.

Electrochemical Study

Electrochemical measurements were performed on a CH Instruments 627e potentiostat/galvanostat using a BASi RDE-2 rotating disk electrode equipped with a jacketed glass cell and PTFE cap (*36-38*). The cell was maintained at a constant temperature of 30.0˚C unless otherwise noted. Viton® o-rings were used to seal the electrodes and bubbler into the ports of the PTFE cap. In all experiments, a platinized platinum coil was used as the counter electrode. An eDAQ Hydroflex™ Hydrogen Reference Electrode was used as the reference electrode, except for experiments involving the presence of CO in the electrolyte, in which a leak-proof 3 M NaCl Ag/AgCl reference electrode calibrated to the eDAQ hydrogen reference electrode was employed. All potentials are reported versus RHE. iR compensation was used where reported, while the uncompensated solution resistance was typically ~ 30 Ω.

Gases were delivered to the electrochemical cell using a high surface area fritted glass bubbler and controlled using a calibrated Sierra SmartTrak® mass flow controller. For measurements involving CO/H_2 mixtures, the CO was delivered using a calibrated Sierra MicroTrak® ultra low flow controller.

3 mm glassy carbon (GC) disk electrodes were used as the substrate for the catalyst inks. The GC working electrodes were freshly polished using a 0.05 μm alumina suspension on a Texmet pad for 2 min in a figure eight pattern, rotating 90˚ every 30 sec. The electrodes were then rinsed with methanol, sonicated for 5 sec in acetone, rinsed thoroughly with DI water and dried in N_2 flow.

Catalyst inks were prepared from a common stock solution consisting of 50 mL of DI water, 4 mL of isopropanol, and 1 mL of 5% Nafion® 117 solution. For all experiments, the inks consisted of 3 mg of catalyst by total mass per 1 gram of solution. These inks were sonicated for 1 h in an ice bath. Immediately after sonicating, 6 μL droplets were loaded onto the surface of the freshly cleaned GC working electrodes. The electrodes were then dried by pulling a slow vacuum to -380 Torr, holding for 5 min, and then pulling a slow vacuum to -710 Torr and holding for 15 min to obtain an optically uniform black thin film. For the control catalysts, the NM loading was ~ 51 μg cm^{-2}_{geo} while for the core-shell catalysts, the NM loading was ~ 20 μg cm^{-2}_{geo}. Exact loadings were determined using ICP-MS.

The working electrodes were then pre-treated by rinsing with DI water, swirling in 0.1 M NaOH solution for 2 min, and then rinsing again with copious amounts of DI water. The working electrode was always lowered into fresh electrolyte solutions under potential control at 0.1 V. The final pretreatment step consisted of 100 conditioning cyclic voltammetry (CV) scans performed from -0.05 V to 0.6 V at 200 mV s^{-1} and a rotation rate of 2500 rpm in Ar-purged 0.1 M $HClO_4$. Pt/C was conditioned by cycling from -0.05 V to 1.2 V.

The electrolyte was then switched to fresh H_2-purged 0.1 M $HClO_4$ for HER/HOR studies at 0, 400, 900, 1000, 1600, and 2500 rpm. These measurements were performed at

10 mV s^{-1} followed by chronoamperometry and chronopotentiometry HER studies at 2500 rpm.

Afterwards, a fresh H_2-purged 0.1 M $HClO_4$ electrolyte was used for CO/HOR studies. After an initial HOR scan at 2 mV s^{-1} and 1600rpm, the working electrode was held at 0.025 V and 1600 rpm for an arbitrarily long time (e.g. 180 min) while the gas flow was switched to 99.9 ± 0.1 mL min^{-1} H_2 and 100 ± 1 µL min^{-1} of CO. Once the geometric current dropped below 0.1 mA cm^{-2} (typically requiring approximately 2 h), an iR-compensated LSV was performed from 0.025 V to 0.6 V at 2 mV s^{-1}. A low potential of 0.025 V was used because the NM/TMC core shell materials would not saturate with CO at 0.05 V or above due to their high CO tolerance.

Next, the electrolyte was changed to Ar-satured 0.1 M $HClO_4$ and the working electrode was conditioned from -0.05 V to 1.0 V at 1600 rpm and 50 mV s^{-1} for 20 cycles. 3 cycles from 0.025 V to 1 V at 0 rpm and 20 mV s^{-1} were performed to obtain an estimate for the H_{upd}-ECSA. The working electrode was then held at 0.025 V and 1600 rpm for 10 min under a pure CO purge and then for another 10 min under a pure Ar purge to remove excess CO. Immediately, 3 iR-compensated cyclic voltammograms (CVs) were performed from 0.025 V to 1.0 V at 50 mV s^{-1}. Prior to CO-stripping, a "simulation" scan was performed under identical conditions as the CO-stripping experiment but under an Ar-purge. This new method developed for ceramic-supported Pt catalysts was done to identify and correct for any potentially confounding signals from the TMC cores (such as surface oxidation) on the actual CO-stripping experiment (*39*).

Methanol electrooxidation (MOR) was performed in Ar-purged 1 M MeOH and 0.1 M $HClO_4$ solution at 30˚C and a rotation rate of 1000 rpm. Under these conditions, the limiting current is approximately 4.5 A cm^{-2}_{geo}. However, the measured currents in this study were at least 1.8 orders of magnitude below this limiting current. To remove excess bubbles, a rotation rate of 2500 rpm was used during high potential CV measurements and CA measurements when holding at a fixed potential of 0.6 V. After a working electrode was lowered into the MOR electrolyte, 100 conditioning scans were performed between -0.05 V and 0.6 V at 200 mV s^{-1}. Afterwards, iR-compensated CA measurements were conducted by holding the electrode at fixed potentials for 15 min intervals at 0.35 V, 0.4 V, 0.45 V, and 0.6 V. The activity was computed by averaging the current over the last minute. Then, iR-compensated CV measurements were performed by cycling between 0.025 V and 1.2 V at 50 mV s^{-1}.

Stability studies were conducted in Ar-saturated 1 M MeOH and 0.1 M HClO4 solution at 30˚C and 1000 rpm from -0.05 V to 0.6 V at 100 mV s^{-1}. During this time, the working electrode oscillated rapidly between performing HER, HOR, and MOR. After 10,000 cycles, a regeneration was attempted by thoroughly rinsing each working electrode with DI water, swirling in 0.1 M NaOH solution for 2 min at room temperature, and then rinsing again with copious amounts of DI water.

Gas Diffusion Electrode (GDE) HOR/HER activity and stability studies were performed to supplement the RDE studies and obtain more accurate kinetic estimates using a recently developed method (*40*, *41*). Catalyst inks were prepared at 3 mg per gram of solution by adding water followed by a solution of IPA:EtOH:5% Nafion® 117 solution. The final ratios used were 25:50:25 H_2O:IPA:EtOH as the solvent with 18 µL of 5% Nafion® 117 solution per 3 mg of catalyst. Sigracet GDL 25 BC from fuelcellstore.com were used to prepare the GDEs, which were cut into 1 cm×2 cm strips. 17 µL of ink was

applied to a 0.2 cm×1 cm line at one end of the GDE and dried vertically in ambient conditions for 2 minutes before being dried further using our standard vacuum protocol described above. For the control catalysts, the NM loading was ~ 51 μg cm^{-2}_{geo} while for the core-shell catalysts, the NM loading was ~ 20 μg cm^{-2}_{geo}. Exact loadings were determined using ICP-MS. In this way, the geometric activities can be compared between the RDE and GDE methods.

The GDE was then suspended vertically in the electrolyte solution from a freshly-polished Ti wire. The solution level was maintained such that the bottom 0.3 cm of the GDE was submerged in solution. In this configuration, the uncompensated solution resistance was ~ 8-10 Ω. The bubbler was not positioned in the electrolyte solution but rather directly above the solution and maintained with 300 cm^3(STP) min^{-1} of either UHP Ar or UHP H_2. Once submerged, the GDE was cycled from 0 V to 0.6 V at 200 mV s^{-1} in Ar-purged 0.1 M $HClO_4$ at 30.0 ˚C. The electrolyte was refreshed, and the flow was then switched to H_2 and two uncompensated LSV scans were obtained at 10 mV s^{-1}. The first was from 150 mV to -150 mV, and the second from -150 mV to 150 mV. The average of these two scans was taken (*41*) for each electrode mounting. The LSV scans were then repeated with standard iR correction applied. Triplicate electrode mountings were performed for each catalyst and averaged. A 10,000 cycle stability study was then conducted for each of the two studied core-shell catalysts as described above. Representative electrodes were then studied in 1.0 M $HClO_4$ at 30.0 ˚C. In this electrolyte, the uncompensated solution resistance was ~ 4 Ω.

It is common for different normalization conventions (e.g. geometric, mass, and specific activity) to be used in the comparison of catalysts for each of the reactions studied. For convenience, the information above and the information in table S1 are provided so that the presented data can be interpreted in the context of either of these three normalization schemes.

Thermal Study

4%Pt/96%$Ti_{0.1}W_{0.9}C$ supported on carbon black at 20wt% (denoted as Pt_{subML}) and Pt_{comm} were loaded into alumina crucibles and subjected to various heat treatments to examine the propensity towards sintering and the stability of sub-monolayer Pt loadings on the surface of TiWC NPs. Heating was always performed at 2 ˚C min^{-1} in a 5% H_2 / 95% N_2 atmosphere using a quartz tubular furnace under 100 cm^3(STP) min^{-1} of total gas flow. Once the final temperature was reached, the atmosphere was changed to either 100% H_2, 100% N_2, or H_2O-saturated N_2 (saturated using a room-temperature saturator). The final temperature was maintained for 4 h, except for one heat study at 600˚C in 100% N_2 where the final temperature was held for 20 h. After the specified time had elapsed, the furnace was allowed to cool naturally with the lid closed under 100 cm^3(STP) min^{-1} of whichever atmosphere was under study. Once at room temperature, the furnace was purged with N_2 bubbled through an H_2O saturator for 2 h at 95 cm^3(STP) min^{-1} and then passivated using a 1%O_2/99%N_2 mixture for 2 h. After passivation, the samples were stored in a dry N_2 glovebox.

Theoretical Study

All calculations were performed within the DFT construct as implemented in the Vienna *ab initio* Simulation Package (VASP) (*42*). Starting with the experimentally determined crystallographic structure of fcc-WC, the lattice parameters and atomic positions were optimized using the PBEsol functional (*43*), with a Gamma point-centered 10×10×10 k-mesh and a 500 eV planewave cutoff. These criteria resulted in energies converged to at least 0.01 eV per atom. The [111] surface was then cut from this optimized structure. The most suitable material was determined by successive iterations to be a stoichiometric polar construction, in contrast to non-stoichiometric surface reconstructions known for other fcc materials (*44*) and non-polar terminations for semiconductors (*45*). Although this termination results in a dipole across the cell, the effect is only non-trivial in semiconductors; the metallic nature of TiWC permits the use of such topology (fig. S13).

The slab was then expanded to a 2×2×1 supercell with a 15 Å vacuum layer. Ti substitutions were then made to the crystalline slab at 10 wt% loading in W lattice sites. The slab, shown in Figure S13, was then relaxed with respect to atomic positions using a 2×2×1 Gamma point-centered k-mesh and the same energetic cutoffs as the bulk material. The Pt layer was then built by the addition of a layer of [111] Pt on the W-terminated surface. The initial Pt positions occupied the next layer C sites. This lattice spacing was a reasonable starting point as it resulted in similar Pt-Pt distances to bulk Pt [111]. To achieve sub-monolayer loading, random Pt atoms were removed from the perfect [111] surface coating. Multilayers were constructed in a similar fashion, through the addition of a second depleted Pt [111] layer.

To provide a description of the surface topology of the Pt at synthetically relevant temperatures, *ab initio* molecular dynamics was used to introduce heat (nuclear kinetic energy) to the slab. Heating was performed from 0 to 700˚C in 0.1˚C per 5 fs time steps. The structure was then held at the terminal temperature to reach a steady-state structure. 700˚C was determined a sufficient final temperature from studies up to 1700˚C, which did not alter the 700˚C steady-state structure.

The standard state for Pt was obtained by full optimization of the experimental crystal structure, using 500 eV cutoff and an 8×8×8 k-mesh. Slabs of Pt were constructed in the same fashion as WC and TiWC. Surface binding energies were computed using a previously presented method (*46*).

Workfunctions were aligned using a code freely available online (*47*). Electronic d-band centers were aligned through the integral of the partial density of states for relevant atoms (*48*).

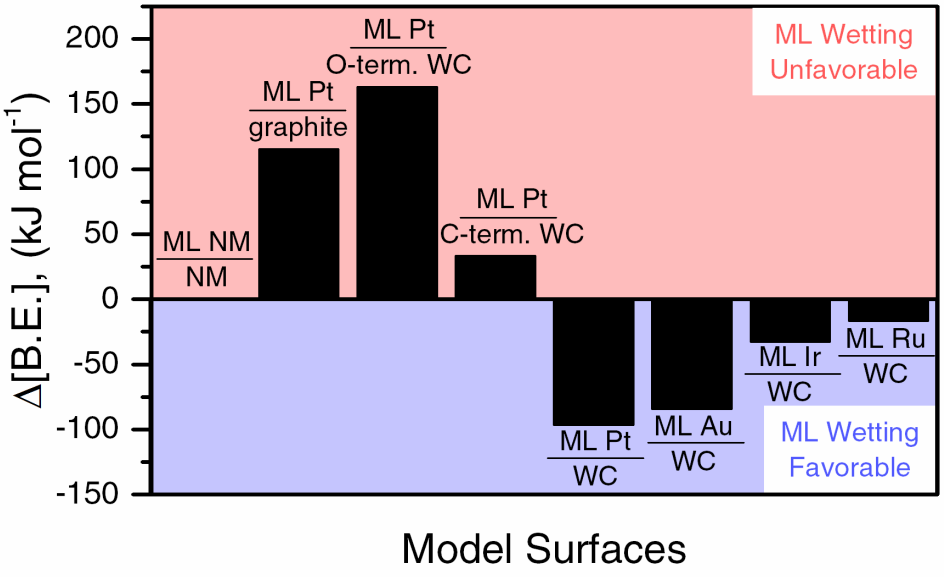

Fig. S1. Theoretical study of the NM probability to wet various surfaces.

DFT study of the binding energies of noble metal monolayers (NM MLs) on various planar surfaces compared to the binding energies of NM MLs on native NM planar surfaces. $\Delta[B.E._{ML\ NM/NM} - B.E._{ML\ NM/NM}]$ (denoted as Δ[B.E.]) is greater than zero for a ML of Pt adsorbed on graphite, oxygen-terminated WC, and carbidic carbon-terminated WC. This predicts that it is less favorable for Pt to wet these surfaces in a ML fashion than to bind to itself. This is consistent with i) atomic layer deposition (ALD) studies of Pt on high surface area graphitic carbon supports where Pt does not grow layer by layer but instead forms nanoparticles (*49*) and ii) the observations that Pt does not wet WC surfaces which are passivated or coated in graphitic carbon but instead form separate fcc Pt crystallites (*50*, *51*). Beyond WC, the inability to wet passivated materials with Pt is well-known, such as the observation that Pt does not wet oxide-terminated Ni nanoparticles (*52*). Δ[B.E.] is less than zero for a ML of Pt, Au, Ir, and Ru adsorbed on the surface of metal-terminated WC, suggesting that it is favorable for these NMs to "wet" metal-terminated WC surfaces in a ML fashion as demonstrated experimentally in the current study.

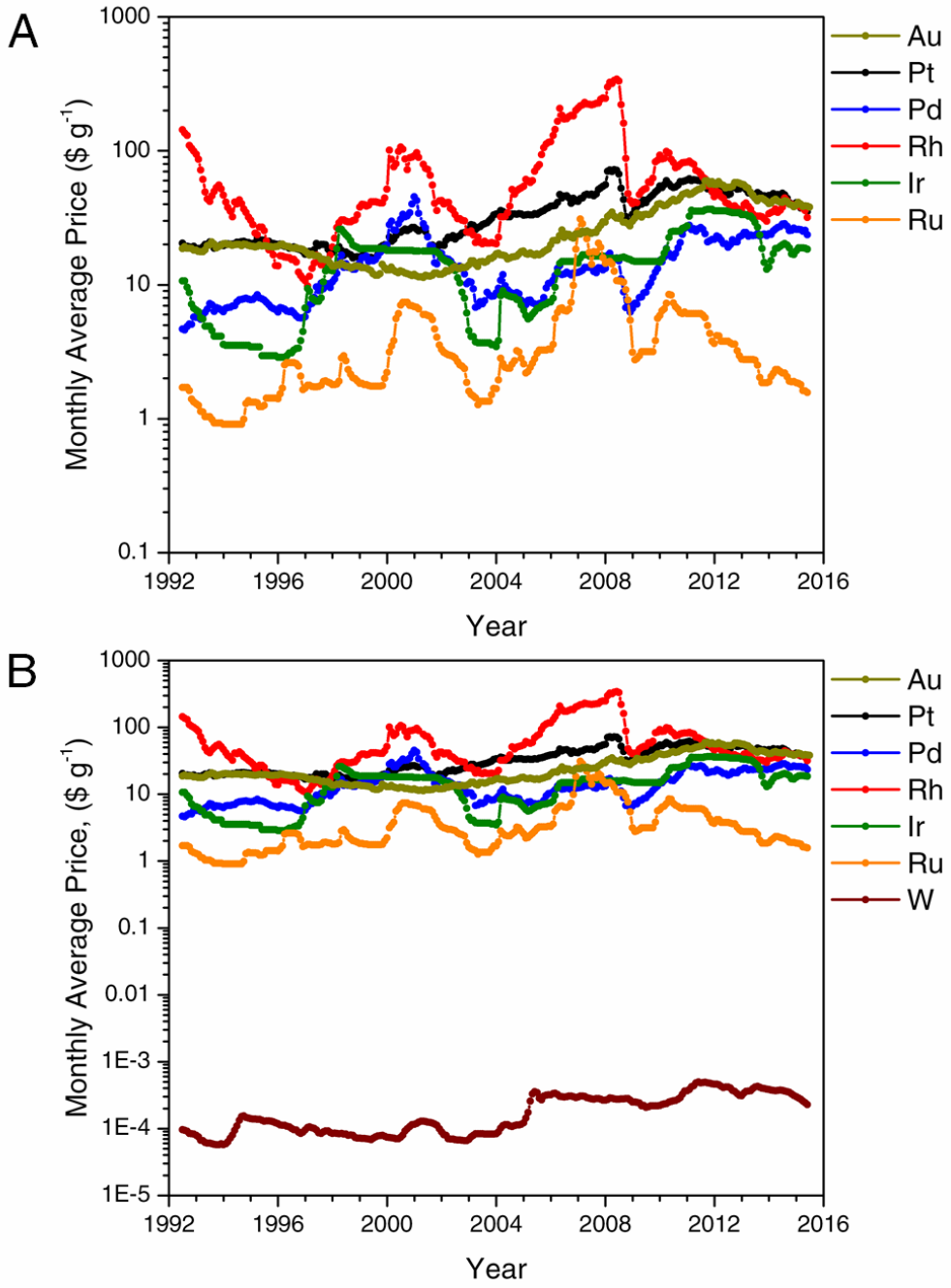

Fig. S2. Cost comparison between noble metals and ammonium paratungstate.
Inflation-adjusted (to Q2 2015) monthly average prices (in USD) for **(A)** noble metals and **(B)** noble metals in comparison to reagent-grade ammonium paratungstate. Historical prices were obtained from publicly available information (*53-55*).

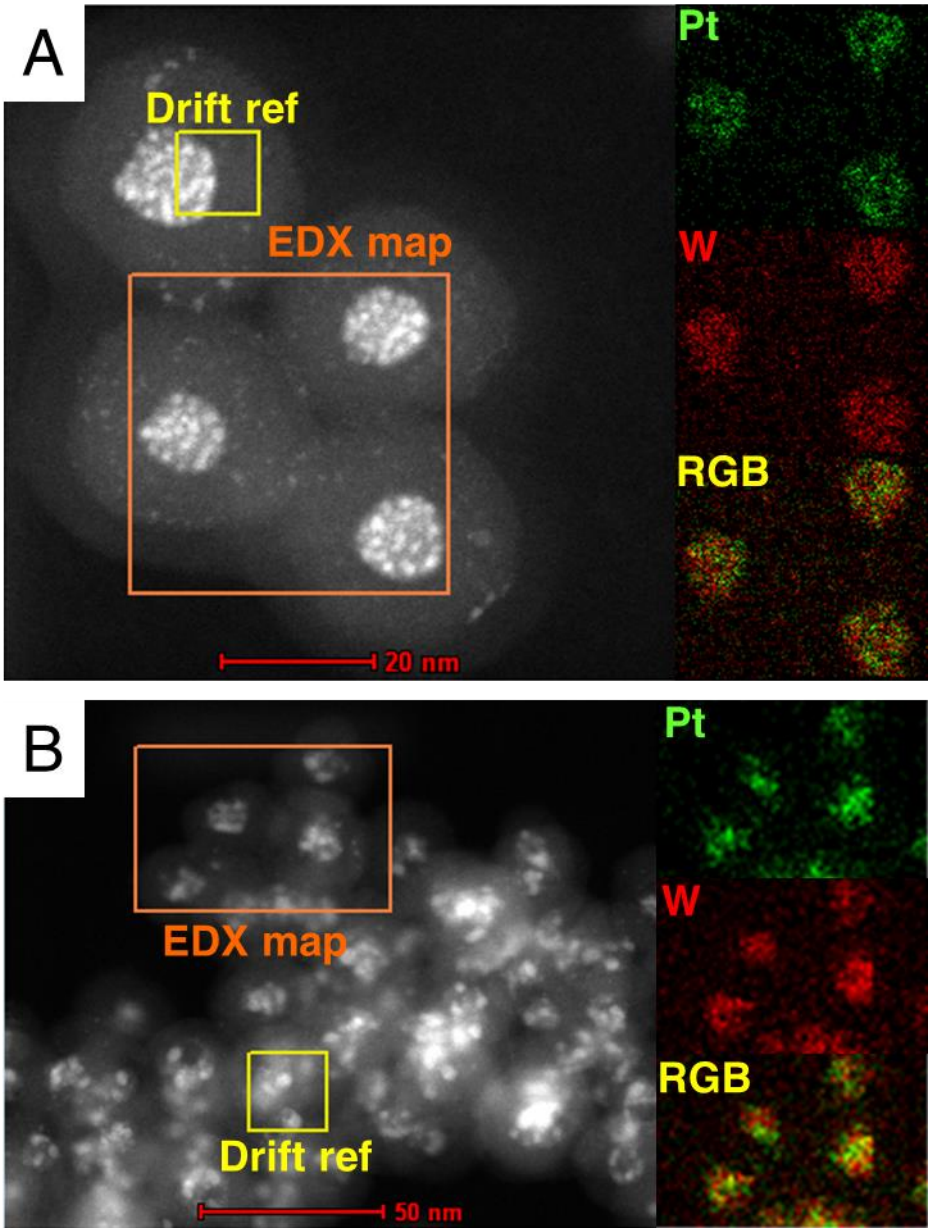

Fig. S3. Structural changes in $SiO_2/(NH_4)_2PtCl_6/WO_x$ system during carburization. **(A)** STEM image and EDX map of $SiO_2/Pt/WO_x$ after heating to 200˚C in a 15% CH_4/85% H_2 atmosphere corresponding to Fig. 1B. **(B)** STEM and EDX map of SiO_2/Pt_xW_y after heating to 600˚C in a 15% CH_4/85% H_2 atmosphere corresponding to Fig. 1C.

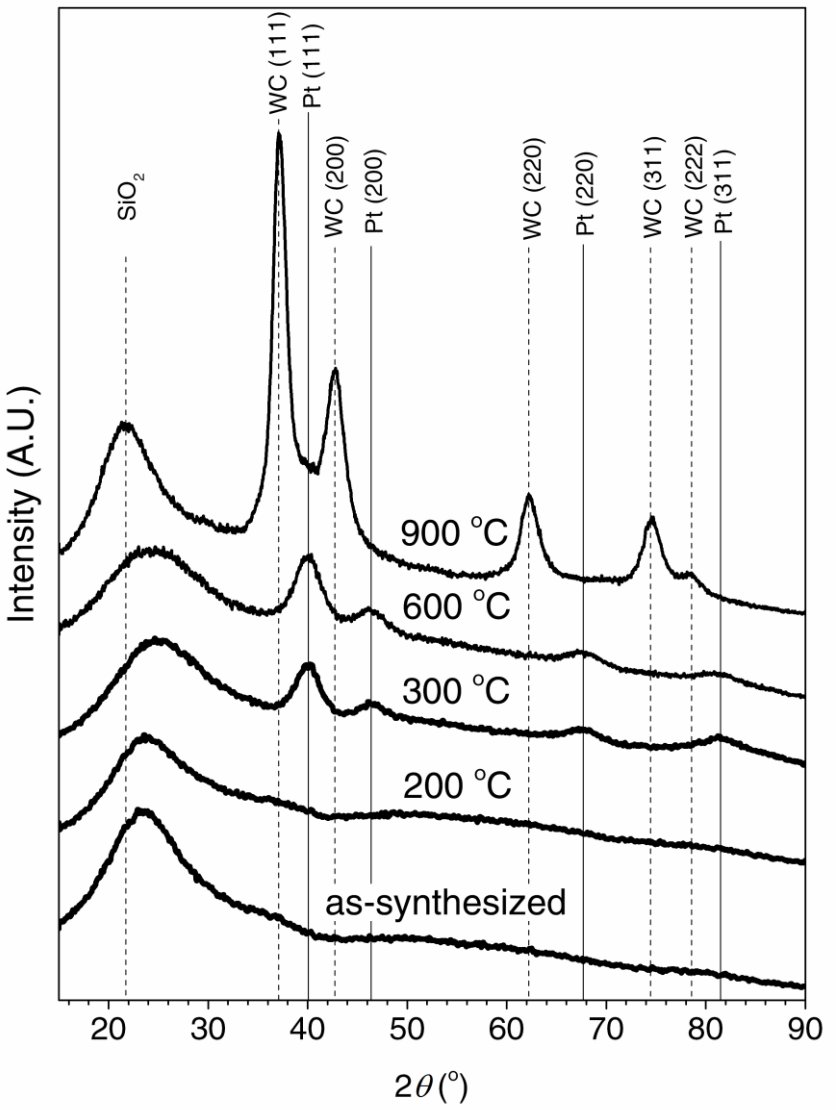

Fig. S4. PXRD study of the core-shell NP self-assembly process during carburization. PXRD diffractograms of as-synthesized $SiO_2/(NH_4)_2PtCl_6/WO_x$ after heating to 200˚C, 300˚C, 600˚C, and 900˚C in a 15% CH_4/85% H_2 atmosphere with a heating ramp of 2˚C min^{-1}. The sample heated to 900˚C was kept at this temperature for 5 h. The PXRD diffractograms for the materials as-synthesized (i.e. 25˚C), 200˚C, 600˚C, and 900˚C correspond to the materials presented in Fig. 1A-D.

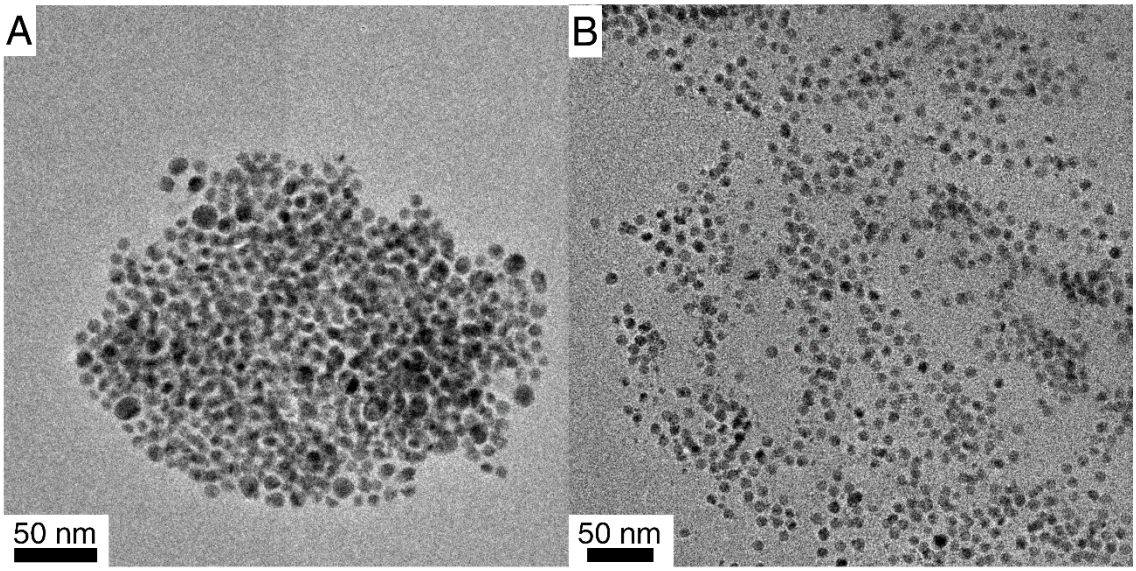

Fig. S5. Microscopic analysis of the core-shell NM/TMC nanodispersions.

(A) A representative TEM image of an NM/TMC nanoaggregate dispersed in ethanol obtained by dissolving the silica shells without adding either a catalyst support or a surfactant capping agent. The material is Pt/$Ti_{0.1}W_{0.9}C$ core-shell NPs corresponding to $Pt_{C\text{-}S}$ and is typical of the material formulation used for XPS analysis of NM/TMC NPs. **(B)** A representative TEM image of NM/TMC NPs dispersed in ethanol using oleylamine as a capping agent after removal of the silica template. The above material consists of PtRu(1:1)/$Ti_{0.1}W_{0.9}C$ core-shell NPs.

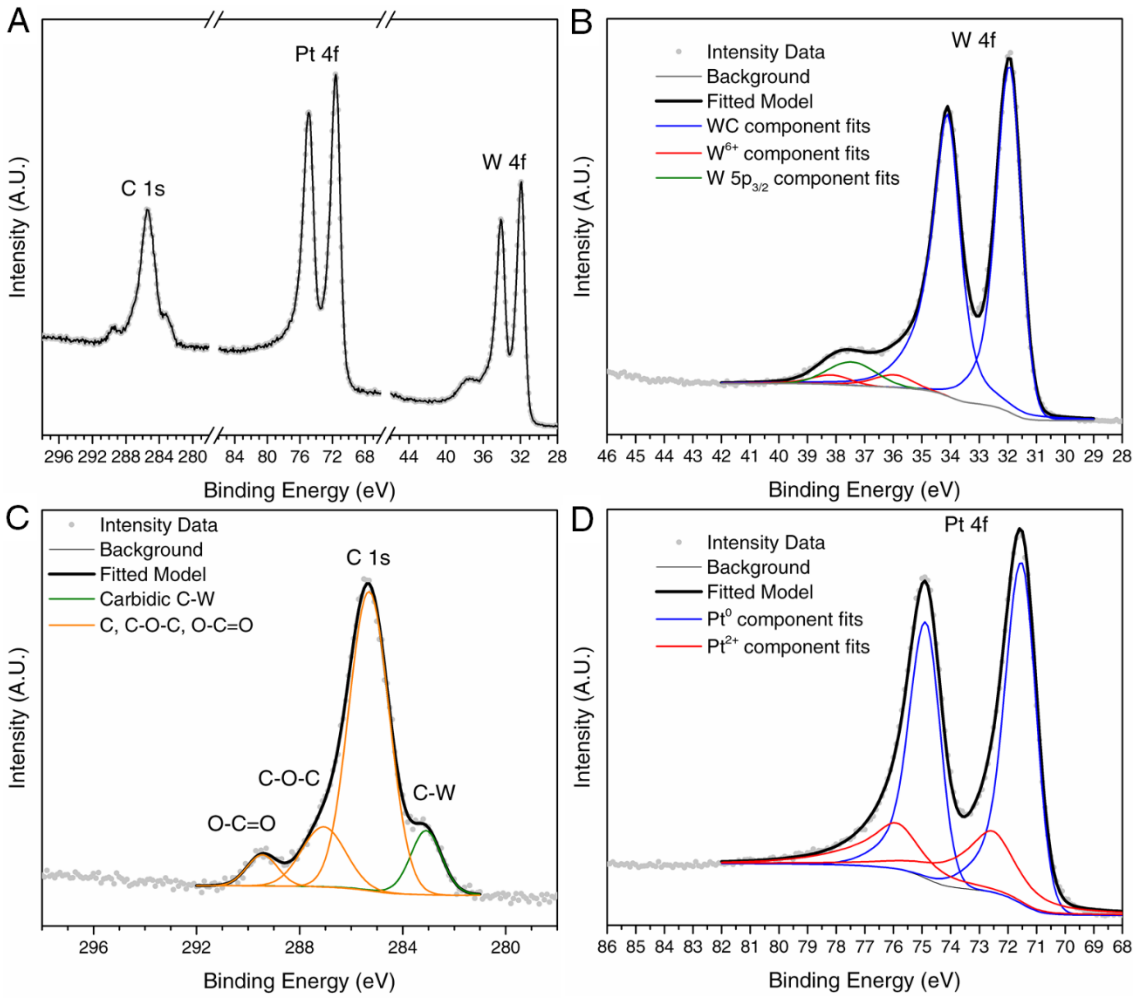

Fig. S6. XPS analysis of $Pt_{C\text{-}S}$.

(A) Raw XPS intensity data obtained for 28%Pt/72%$Ti_{0.1}W_{0.9}C$ core-shell NP nanoaggregates ($Pt_{C\text{-}S}$ formulated as a nanoaggregate in ethanol without carbon black support added during silica removal to obtain a clearer C 1s spectrum).

(B) XPS peak deconvolution of the W 4f spectrum.

(C) XPS peak deconvolution of the C 1s spectrum. The C:TiW ratio was 0.73

(D) XPS peak deconvolution of the Pt 4f spectrum.

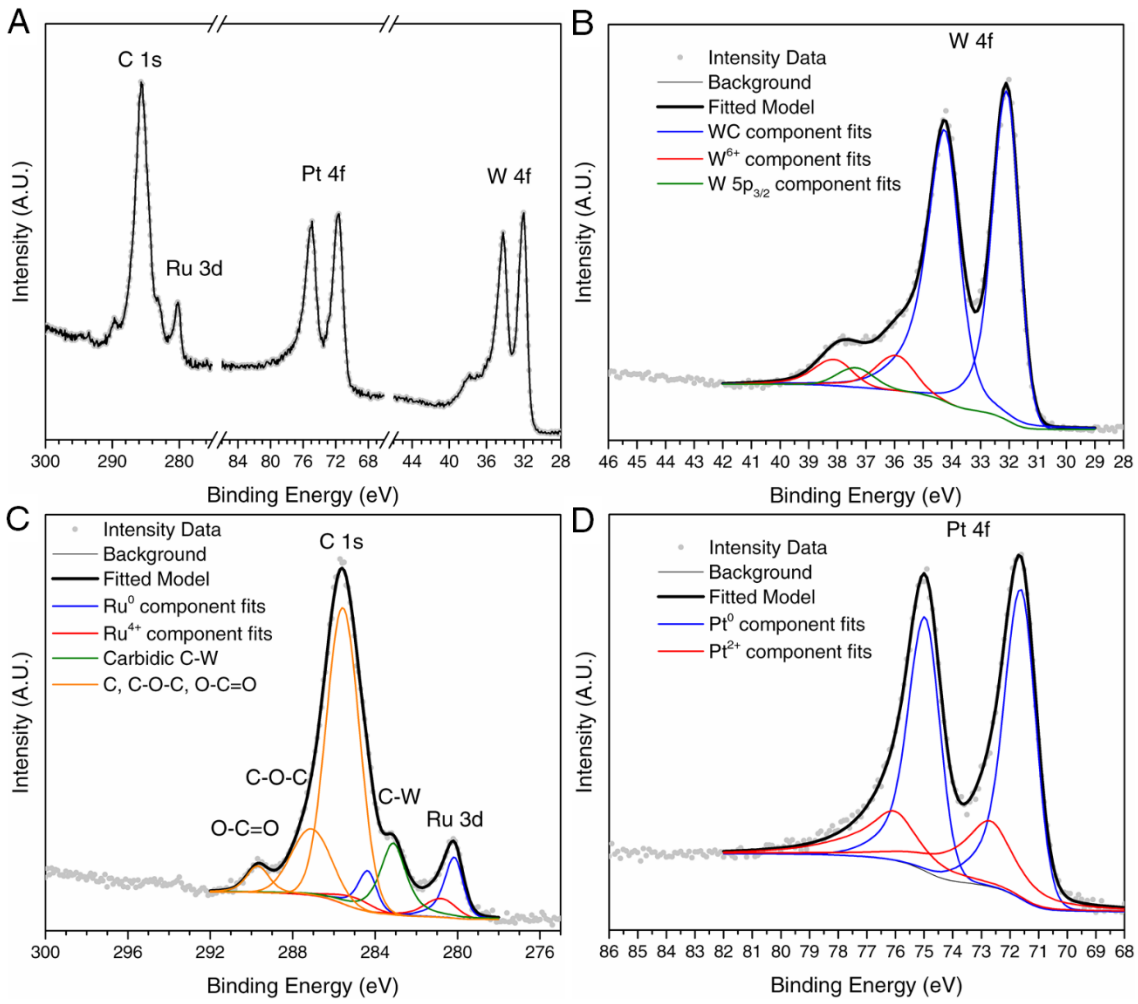

Fig. S7. XPS analysis of PtRu$_{C\text{-}S}$.

(A) Raw XPS intensity data obtained for 27% $Pt_{0.67}Ru_{0.33}$ / 73% $Ti_{0.1}W_{0.9}C$ core-shell NP nanoaggregates ($PtRu_{C\text{-}S}$ formulated as a nanoaggregate in ethanol without carbon black support added during silica removal to obtain clear C 1s spectrum).

(B) XPS peak deconvolution of the W 4f spectrum.

(C) XPS peak deconvolution of the C 1s and Ru 3d spectra. The carbidic C:TiW ratio was 0.78

(D) XPS peak deconvolution of the Pt 4f spectrum.

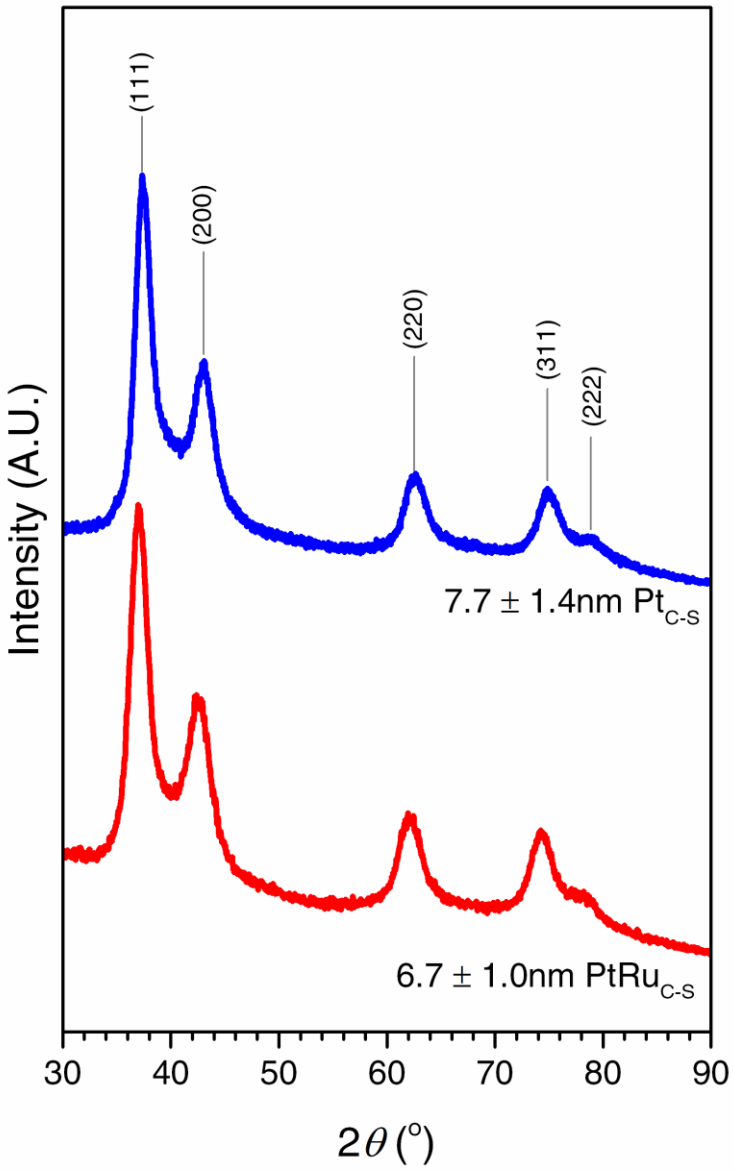

Fig S8. PXRD comparison between Pt$_{C-S}$ and PtRu$_{C-S}$.

PXRD patterns of Pt$_{C-S}$ and PtRu$_{C-S}$ showing phase-pure fcc WC lattices without additional reflections associated with metallic Pt or Ru.

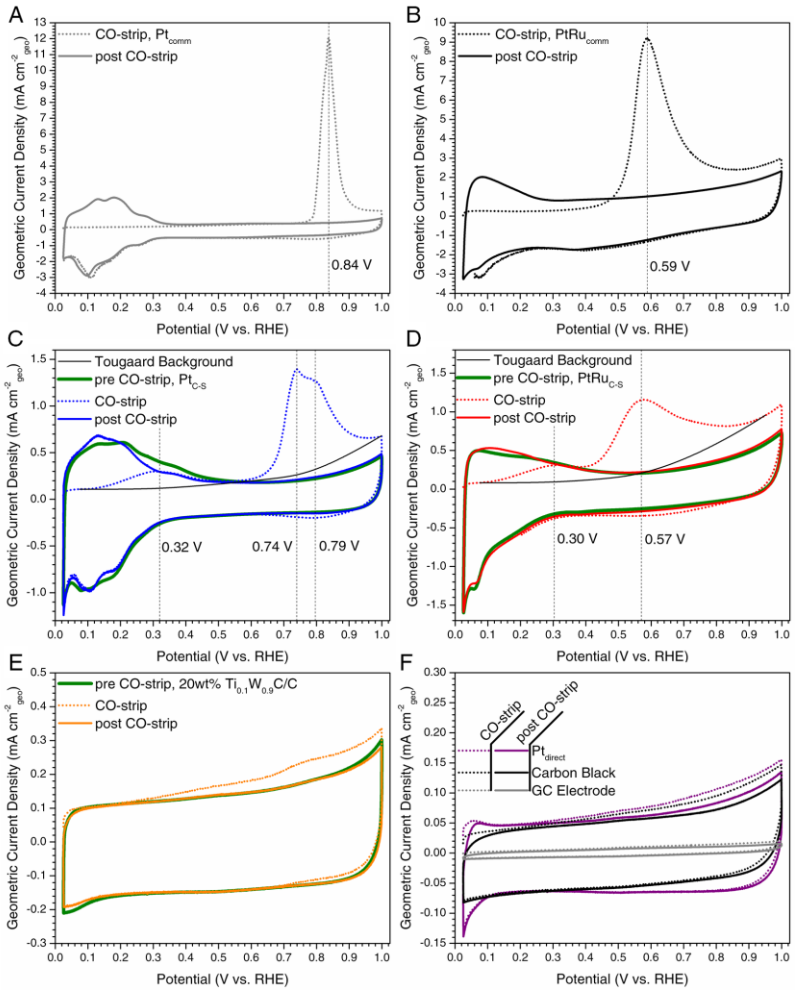

Fig. S9. CO-stripping voltammograms for various catalysts and controls.

CO-stripping voltammograms of **(A)** Pt_{comm}, **(B)** $PtRu_{comm}$, **(C)** $Pt_{C\text{-}S}$, **(D)** $PtRu_{C\text{-}S}$, **(E)** 20 wt% $Ti_{0.1}W_{0.9}C$, and (**F**) $Pt_{direct,}$ carbon black, and empty GC electrode, collected by holding the working electrode potentiostatically at +0.025 V vs. RHE in CO-saturated 0.1 M $HClO_4$ at 30˚C under a rotation rate of 1600 rpm followed by an Ar-purge and scanning at 50 mV s^{-1} with iR compensation. The reported "post CO-strip" CVs are the second scan obtained immediately after the first CO-stripping scan. In some cases, a "pre CO-strip" CV was obtained immediately prior to the actual CO stripping measurement in accordance with a recently developed method to obtain a more accurate background (*39*). However, due to the complex pre-peak of the core-shell samples, an optimized Tougaard background was used when integrating the charge under the CO-stripping voltammograms instead of standard linear backgrounds, which were found to bisect the data. The Tougaard background was found to be more suitable and more conservative than using either the pre or post CO-stripping scans as backgrounds. *If* the carbide cores were *not* subsurface, fig. S9E shows that the contribution from the carbide core to the CO-stripping voltammograms in figs. S9C and S9D would be less than 10%. CO-stripping was performed as the last step in all experimental sequences, after conditioning scans, HER, HOR, CO/HOR, and MOR studies (*56*).

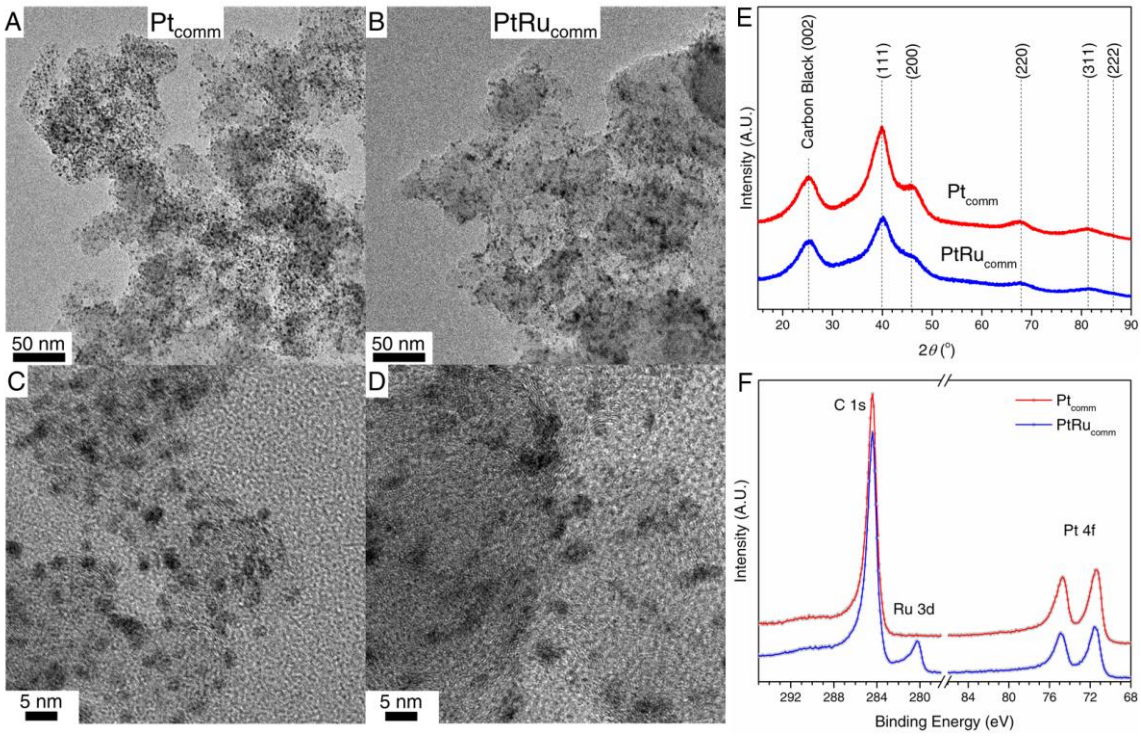

Fig. S10. Characterization of commercial Pt_{comm} and $PtRu_{comm}$ catalysts.
Wide-view TEM and HR-TEM images of **(A,C)** Pt_{comm} and **(B,D)** $PtRu_{comm}$. **(E)** PXRD patterns of Pt_{comm} and $PtRu_{comm}$. (**F**) XPS spectra of Pt_{comm} and $PtRu_{comm}$.

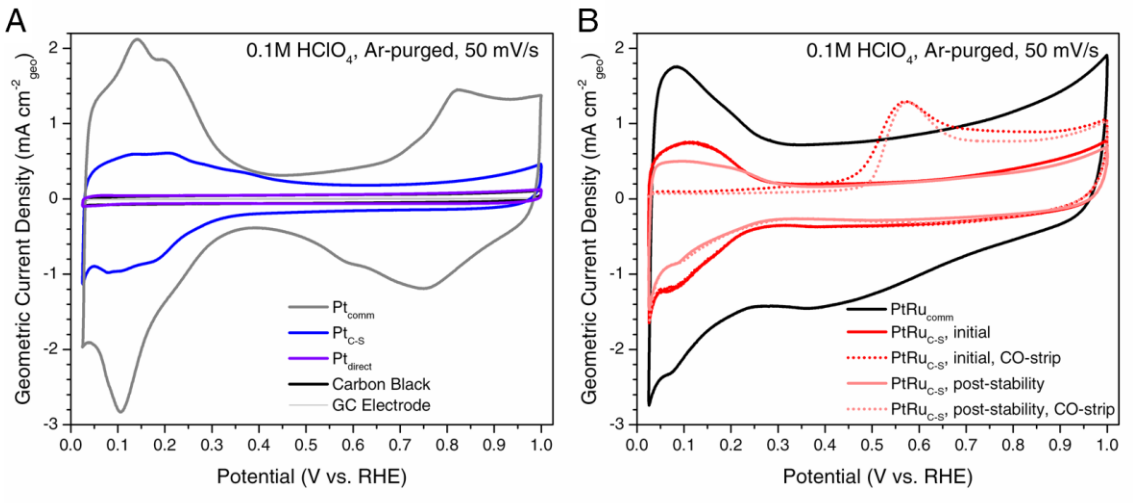

Fig. S11. CVs of various catalysts and controls.

(**A**) and (**B**) Post-conditioning CVs collected from +0.025 V to 1.0 V at 50 mV s^{-1} in Ar-saturated 0.1 M $HClO_4$ at 30˚C under a rotation rate of 1000 rpm. Pt_{direct} exhibits similar electrochemical behavior as the Vulcan® XC-72r carbon black control, in agreement with the TEM and XPS analysis (Fig. 2) illustrating particle sintering and blockage of active sites by graphitic coke. In contrast, the cyclic voltammograms (CVs) for $Pt_{C\text{-}S}$ and $PtRu_{C\text{-}S}$ exhibit high capacitance and characteristic peaks for hydrogen adsorption/desorption (H_{upd}) below 0.4 V, but with notable differences from Pt_{comm} and $PtRu_{comm}$, such as suppressed OH adsorption/desorption (OH_{ad}) features above 0.6 V. These differences suggest that the TiWC cores modulate the electrochemical behavior of the Pt and PtRu shells.

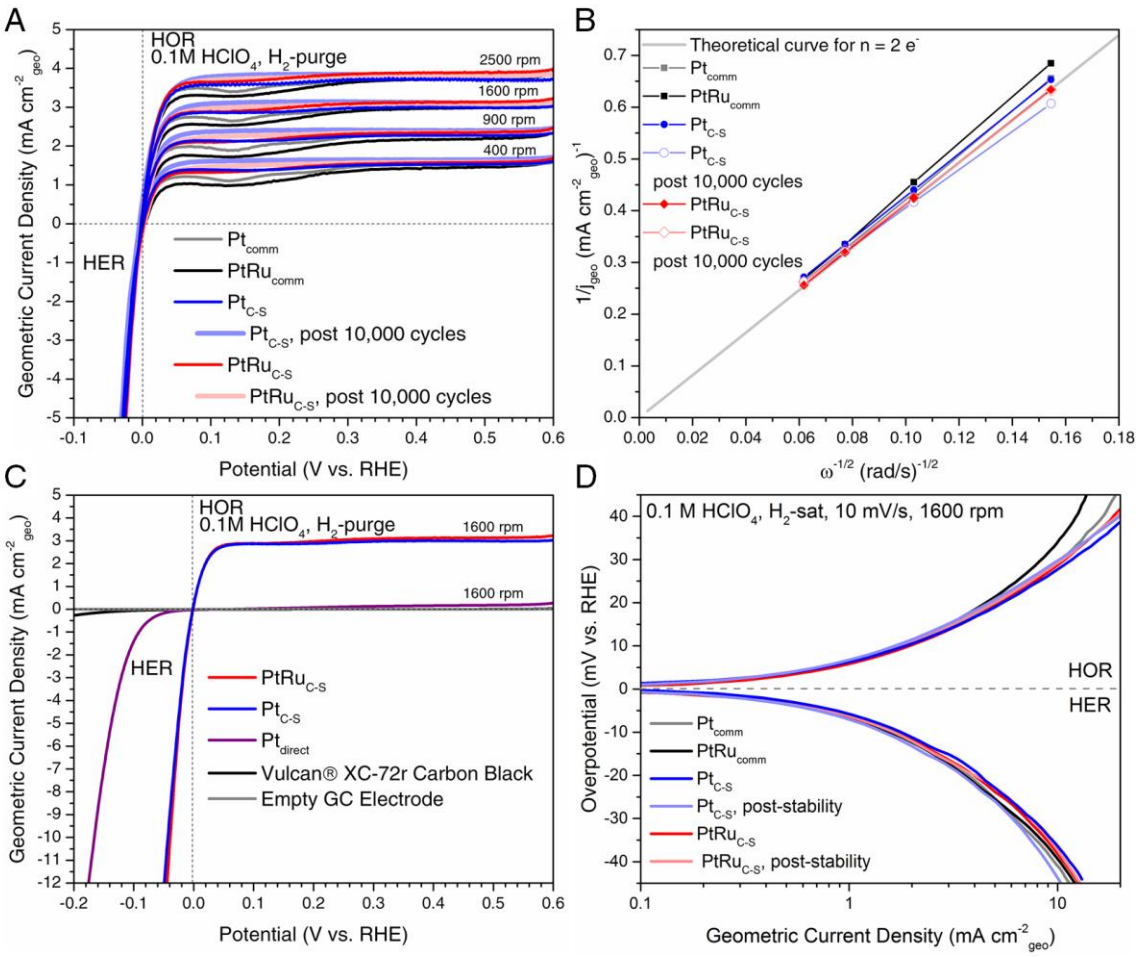

Fig. S12. HOR and HER activity analysis using an RDE.

All measurements were performed in H_2-saturated 0.1 M $HClO_4$ at 30˚C and 10 mV s^{-1} using various rotation rates listed on each panel.

(A) Raw LSV data collected for various catalysts before and after 10,000 potential cycles. These data were used to obtain the Tafel plots in panel D

(B) A Koutecky-Levich plot obtained from the LSVs shown in (A) using the current densities at 0.5 V and various rotation rates. The theoretical line was constructed for a 2-electron transfer process using a diffusion coefficient of $4.5 \cdot 10^{-5}$ cm^2 s^{-1}, a solution viscosity of 0.008 cm^2 s^{-1} at 30˚C, and a concentration of $7.2 \cdot 10^{-7}$ mol H_2 cm^{-3} electrolyte.

(C) Raw LSV data obtained at 1600 rpm for $Pt_{C\text{-}S}$ and $PtRu_{C\text{-}S}$ compared to empty Vulcan® XC-72r carbon black, an empty GC electrode, and Pt_{direct}. The extensive coking and sintering suppresses both the HER and HOR activity of Pt_{direct} in comparison with the core-shell materials prepared using silica encapsulation/removal.

(D) Tafel plot constructed from the 1600 rpm RDE data in panel A. This plot was used to extract the RDE kinetic parameters in Table S2.

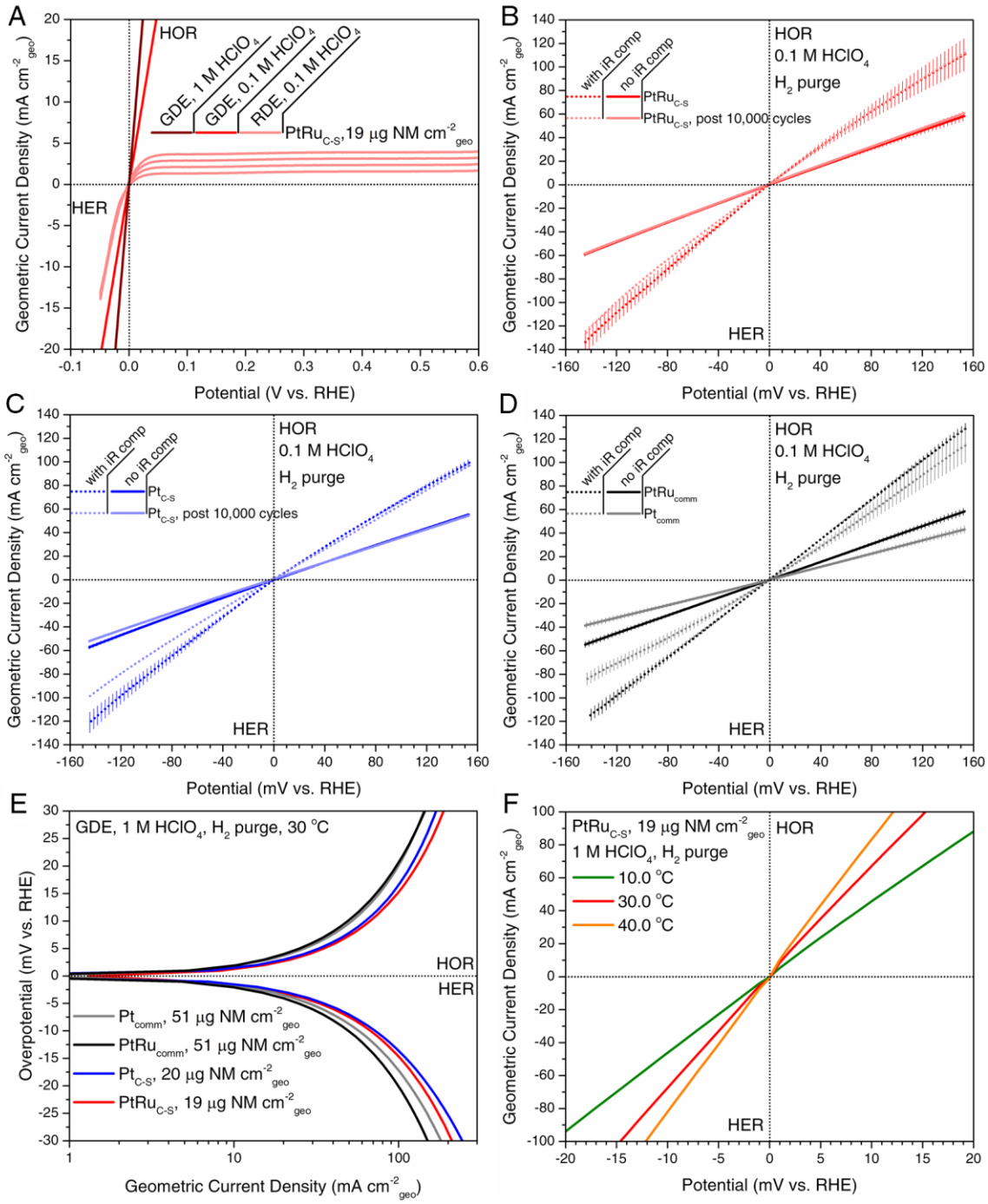

Fig. S13. HOR and HER activity analysis using a GDE.

All measurements were performed under an H_2 purge at 10 mV s^{-1}.

(A) $PtRu_{C\text{-}S}$ HOR/HER LSVs using a GDE in 1 M $HClO_4$, a GDE in 0.1 M $HClO_4$, and an RDE in 0.1 M $HClO_4$ at various rotation rates. No iR compensation was applied.

(B) $PtRu_{C\text{-}S}$ LSVs obtained with and without instrument-applied iR compensation before and after 10,000 cycles. Error bars are shown for the initial activity measurements and were

obtained from triplicate electrode mountings. The iR-compensated data was used to construct Fig. 3A.
(C) Pt_{C-S} LSVs obtained with and without instrument-applied iR compensation before and after 10,000 cycles. Error bars are shown for the initial activity measurements and were obtained from triplicate electrode mountings. The iR-compensated data was used to construct Fig. 3A.
(D) Pt_{comm} and $PtRu_{comm}$ LSVs obtained with and without instrument-applied iR compensation. Error bars are shown for the initial activity measurements and were obtained from triplicate electrode mountings. The iR-compensated data was used to construct Fig. 3A.
(**E**) Tafel plot of iR-compensated LSVs obtained in 1 M $HClO_4$ for Pt_{comm}, $PtRu_{comm}$, Pt_{C-S}, and $PtRu_{C-S}$.
(**F**) $PtRu_{C-S}$ iR-compensated LSVs obtain in 1 M $HClO_4$ at different temperatures.

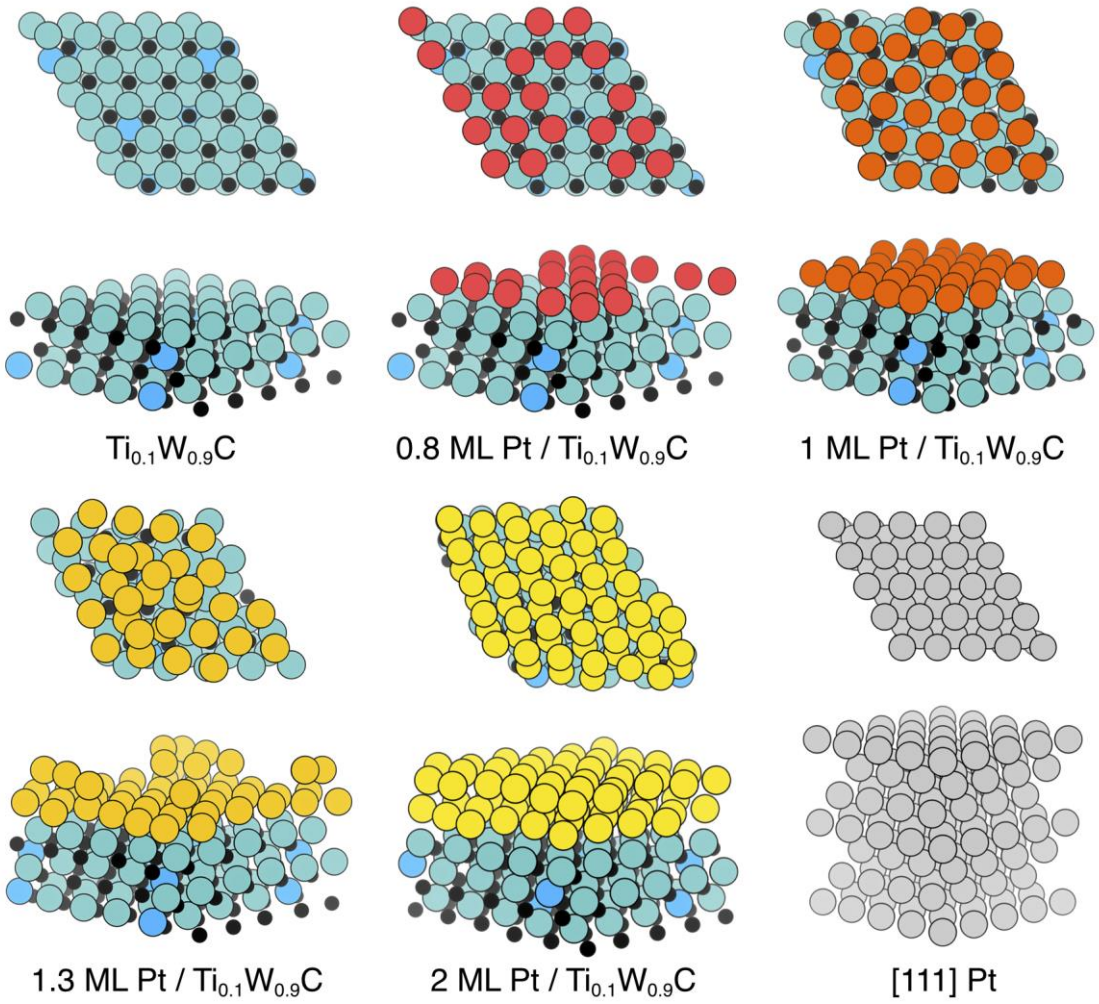

Fig. S14. Model surfaces obtained from high temperature DFT equilibration.

The [111] terminated TiWC slab model with various surface concentrations of Pt. The structures shown are the result of the high temperature equilibrated *ab initio* molecular dynamics simulations on the slabs.

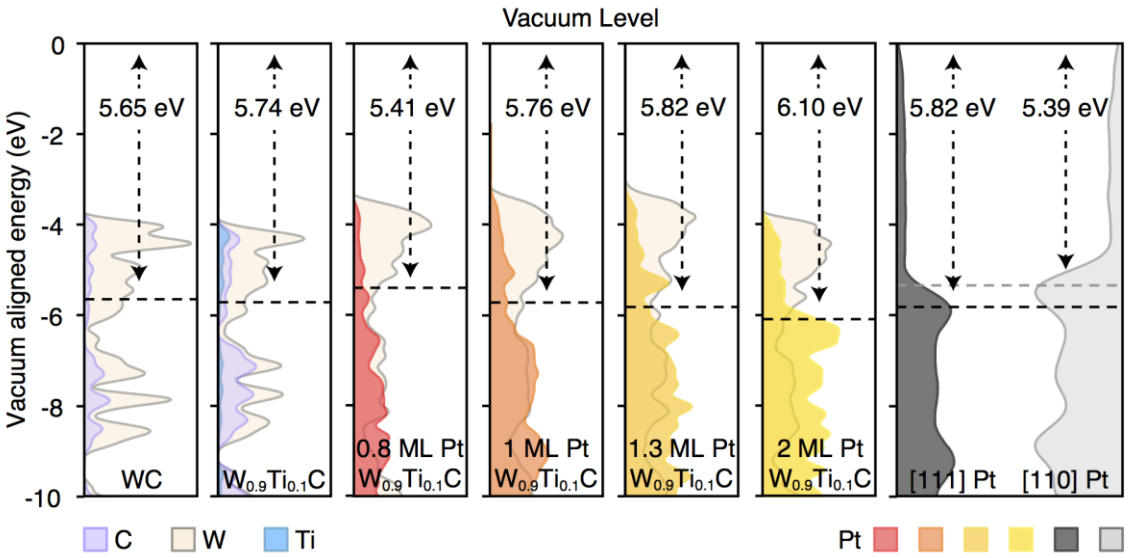

Fig. S15. Elemental projected density of states aligned to the vacuum level.

The elemental projected density of states (Fermi level depicted in dotted lines) for the materials examined herein. The rightmost DOS arise from the pure [111] and [110] surface terminated bulk Pt. The low loading of Pt results in low density, similar to the [110] Pt surface, whereas increased loading provokes the surface Pt to obtain a workfunction nearer to bulk [111] Pt. The decrease in workfunction beyond bulk [111] observed in the 2 ML loading is attributed to the increase in Pt-Pt packing density (91% more dense), which is favored in both the high temperature kinetic modeling and from DFT.

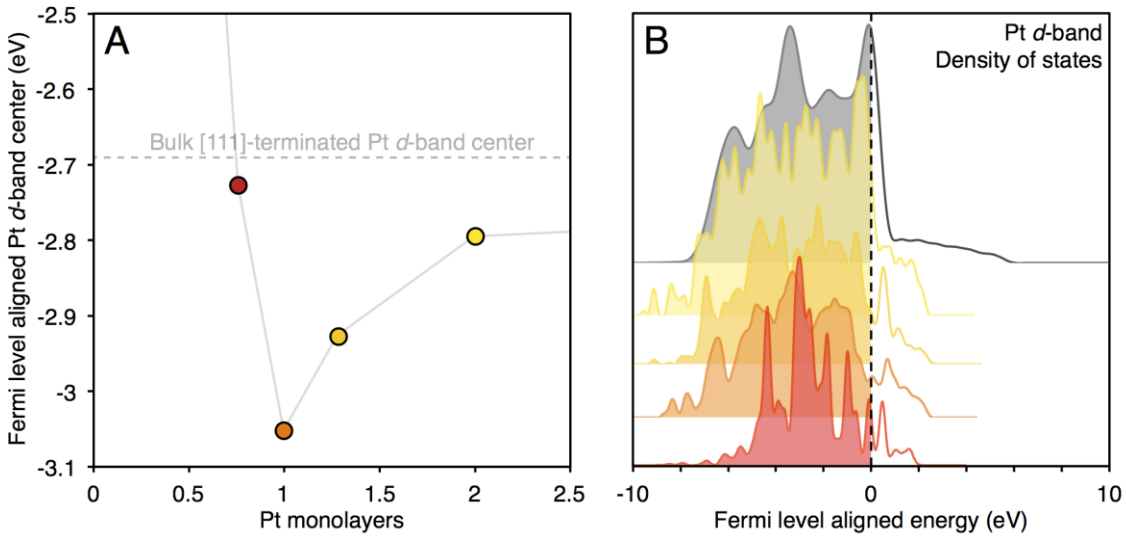

Fig. S16. Comparison of Pt d-band centers from projected density of states.

The Pt d-band can be directly correlated to the CO binding (*57*). The d-band center, as obtained by the mean of the integral of the pDOS, is Morse-like: at low loading levels, the Pt acts highly localized and the d-band descriptor breaks down. At monolayer and greater loading the d-band center progresses to that of bulk [111] Pt.

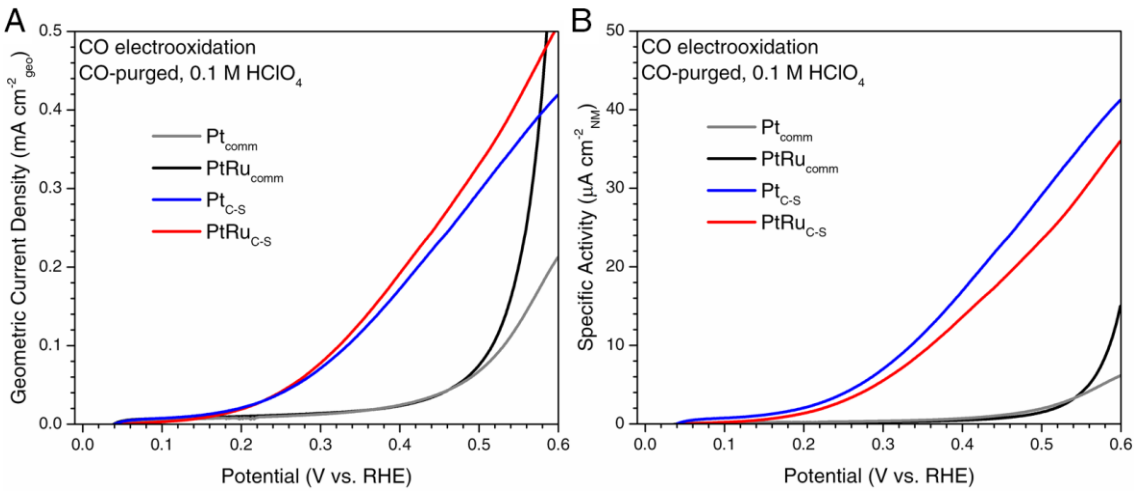

Fig. S17. CO electrooxidation activity.

LSVs with iR compensation showing **(A)** geometric current densities and **(B)** specific activities for various catalysts performing CO electrooxidation in CO-saturated 0.1 M $HClO_4$ at 30˚C and 2 mV s^{-1} under a rotation rate of 1600 rpm. For comparison, the current density at +0.4 V is improved by a factor of 8 for the NM/TMC core-shell materials relative to $PtRu_{comm}$ on a geometric basis and by a factor of 30 on a specific activity basis.

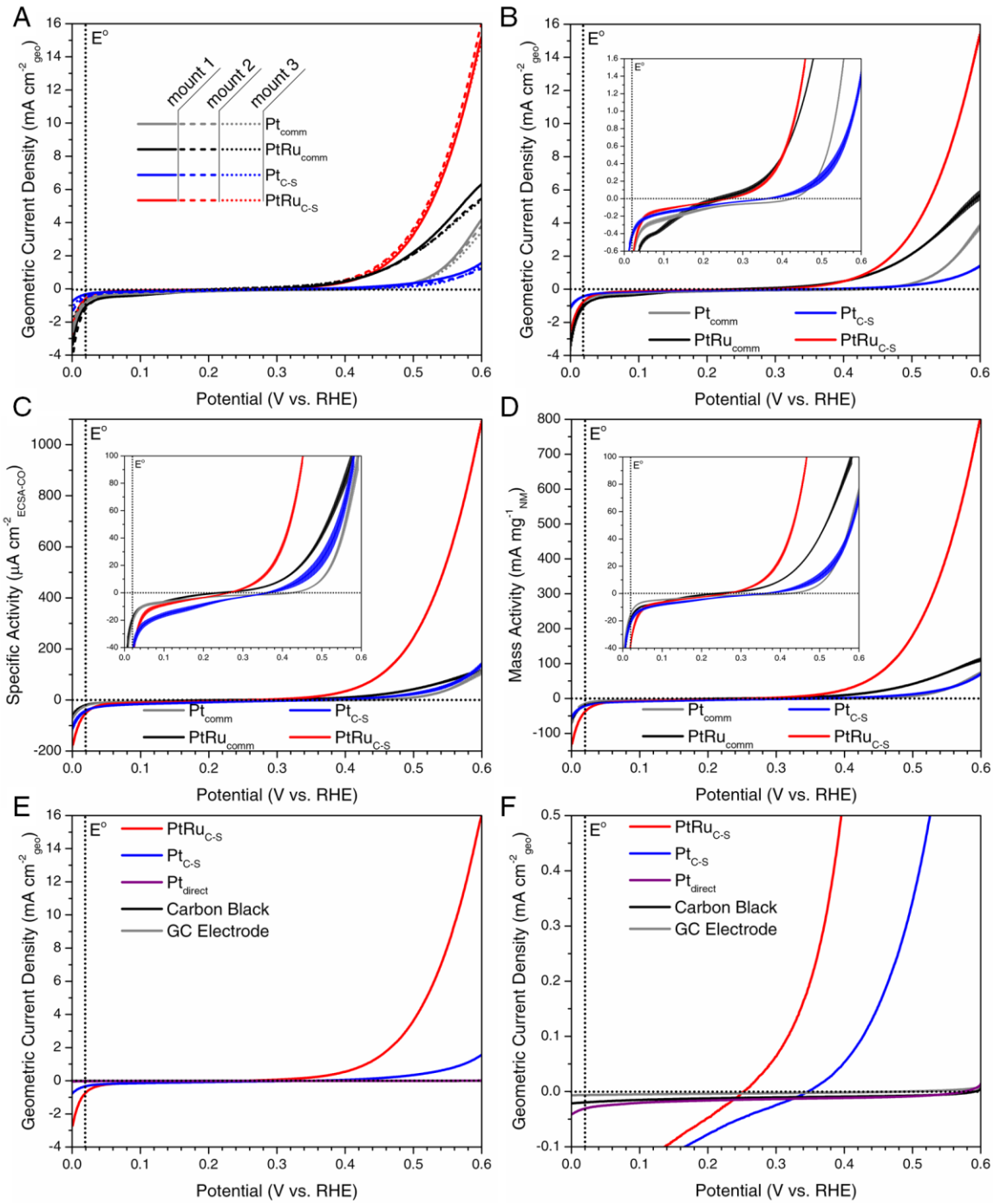

Fig. S18. MOR initial activity comparison and reproducibility study.

(A) LSVs with iR compensation normalized by geometric current density for the NM/TMC core-shell catalysts and commercial controls at 10 mV s^{-1} in 1 M MeOH and 0.1 M $HClO_4$ at 30˚C and 1000 rpm. Each catalyst ink was mounted on three separate electrodes to examine measurement reproducibility. The vertical line represents E^o, the thermodynamic reversible potential for MOR, which is 0.02 V vs. RHE.

(B) The LSVs from (A) with the triplicate runs averaged at each 1 mV interval. The line thickness includes standard deviation error bars. The inset panel is magnified to show differences in the onset potential for MOR.
(C) The LSVs from (B) normalized by specific surface area determined from CO stripping. The errors in the specific surface area measurements are propagated with the errors from the triplicate runs. The inset panel is magnified to show differences in the onset potential for MOR.
(**D**) The LSVs from (B) normalized by loaded NM mass with errors propagated. The inset panel is magnified to show differences in the onset potential for MOR.
(**E**) and (**F**) $PtRu_{C\text{-}S}$ and $Pt_{C\text{-}S}$ LSVs compared to Pt_{direct} and the bare controls under identical conditions where (F) is a magnified view of (E).

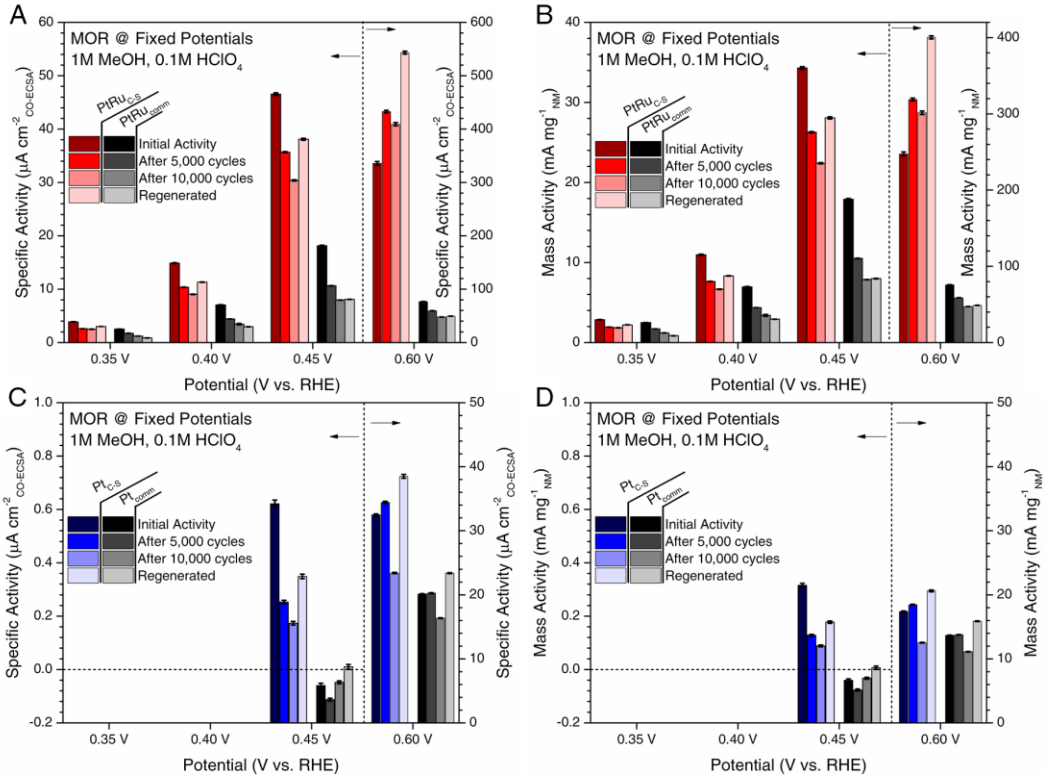

Fig. S19. MOR Stability Study.

Chronoamperometry studies held at fixed potentials for 15 min intervals in 1 M MeOH and 0.1 M $HClO_4$ at 30˚C and 1000 rpm (0.35, 0.4, and 0.45 V) or 2500 rpm (0.6 V). The final current density was averaged over the last 1 min of the measurement. Initial activity measurements were performed after conditioning cycles. The chronoamperometry measurements were repeated after performing 5,000 cycles from -50 to 600 mV at 100 mV s^{-1}, after 10,000 cycles from -50 to 600 mV at 100 mV s^{-1}, and after regeneration (dipping the electrode for 2 min in 0.1 M NaOH solution).
(A) $PtRu_{C\text{-}S}$ compared to $PtRu_{comm}$ on a specific activity basis (Fig. 3E).
(**B**) $PtRu_{C\text{-}S}$ compared to $PtRu_{comm}$ on a mass activity basis.
(**C**) $Pt_{C\text{-}S}$ compared to Pt_{comm} on a specific activity basis.
(**D**) $Pt_{C\text{-}S}$ compared to Pt_{comm} on a mass activity basis.

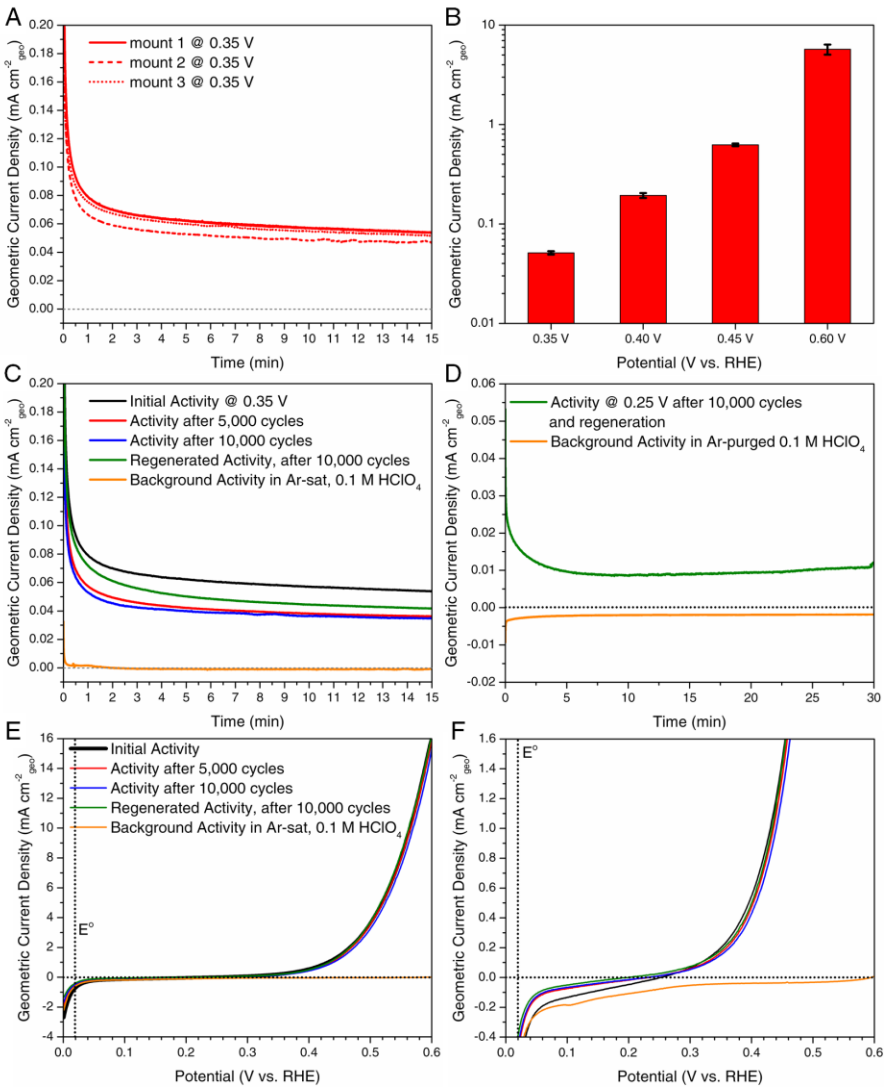

Fig. S20. Detailed analysis of PtRu$_{C\text{-}S}$ performance for MOR.

All measurements were performed in 1 M MeOH and 0.1 M $HClO_4$ at 30˚C under a rotation rate of 1000 rpm (2500 rpm for CA measurements at 0.6 V) with iR compensation applied.
(A) Initial activity CA curves at 0.35 V for triplicate mountings.
(B) Initial activity reproducibility study obtained from averaging the current response over the last minute of CA data collected for 15 min for triplicate electrode mountings. Representative raw CA data is shown in (A).
(C) Representative CA data collected at 0.35 V over 15 min before, during, and after stability cycling as well as regeneration. The background current is obtained in the absence of MeOH. Data averaged over the last minute at various potentials are presented in Fig. 3E-F.
(D) After 10,000 cycles and regeneration in alkaline media, PtRu$_{C\text{-}S}$ maintains a positive current density even at the low potential of 0.25 V over 30 min.
(E) LSVs at 10 mV s^{-1} before, during, and after stability cycling as well as regeneration.
(F) A magnified version of panel (E) showing the onset potential for MOR.

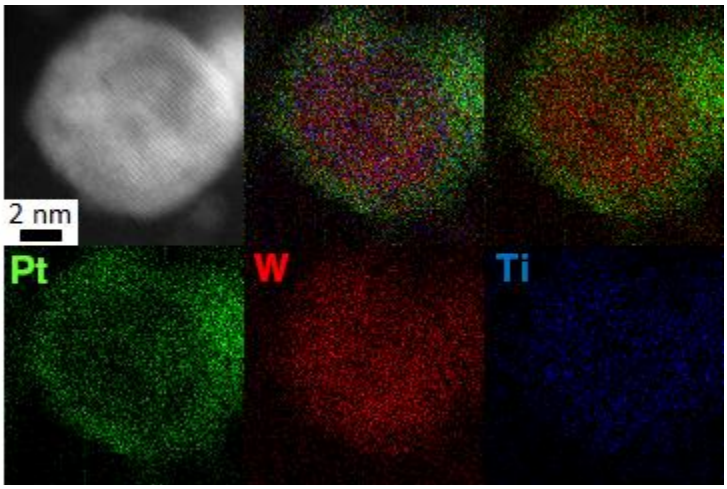

Fig. S21. Microscopic evidence of $Pt_{C\text{-}S}$ stability after cycling.

HR-STEM and EDX map of $Pt_{C\text{-}S}$ after stability cycling from -50 mV to 600 mV. The individual Pt, W, and Ti maps are shown as well as an overlay of all three elements and an overlay of just Pt and W.

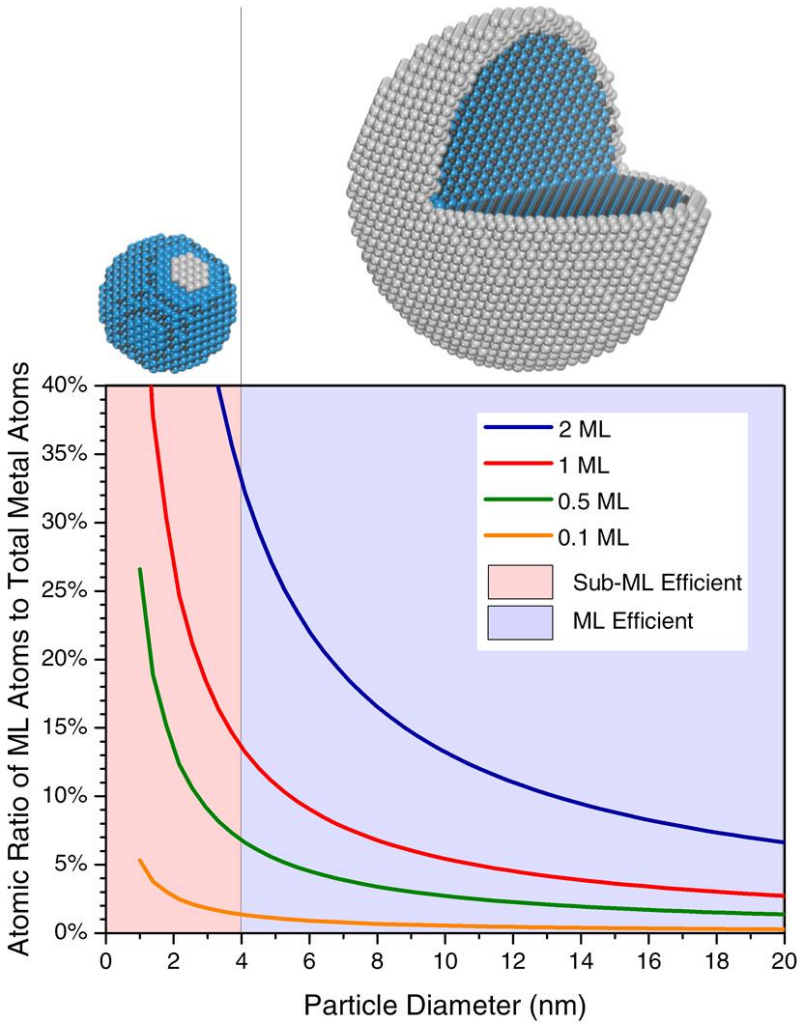

Fig. S22. Core-shell NP design space.

Atomic ratio of surface ML coverage to the total number of metal atoms in the NP versus total NP diameter. Small core-shell NPs with sub-ML NM surface coverages offer complete NM dispersion while also offering bifunctional surfaces with exposed NM sites and TMC sites accessible for catalytic transformations. However, small core-shell NPs with complete ML NM coatings cannot offer substantial NM loading reductions. As such, this regime is designated as "Sub-ML Efficient." For large NPs, complete ML and multilayer NM surface coverages can still result in substantial reductions in NM loadings and are more appropriate for applications in electrocatalysis where durability is a significant challenge. As such, this regime is designated as "ML Efficient."

This figure can also be used to estimate the regime of ML coverage for various NM/TMC core-shell NPs synthesized using the new method reported here. For instance, a 4 nm core-shell NP consisting of 7% NM and 93% TMC (metals basis) has ~0.5 ML NM surface coverage. A 4 nm NP consisting of 13% NM and 87% TMC has ~ 1 ML NM surface coverage, while a 6 nm NP consisting of 22% NM and 82% TMC has ~ 2 ML NM surface coverage. An 8 nm NP consisting of 30% NM and 70% TMC has ~ 3 ML NM surface coverage. These are the typical synthetic regimes targeted in the current study.

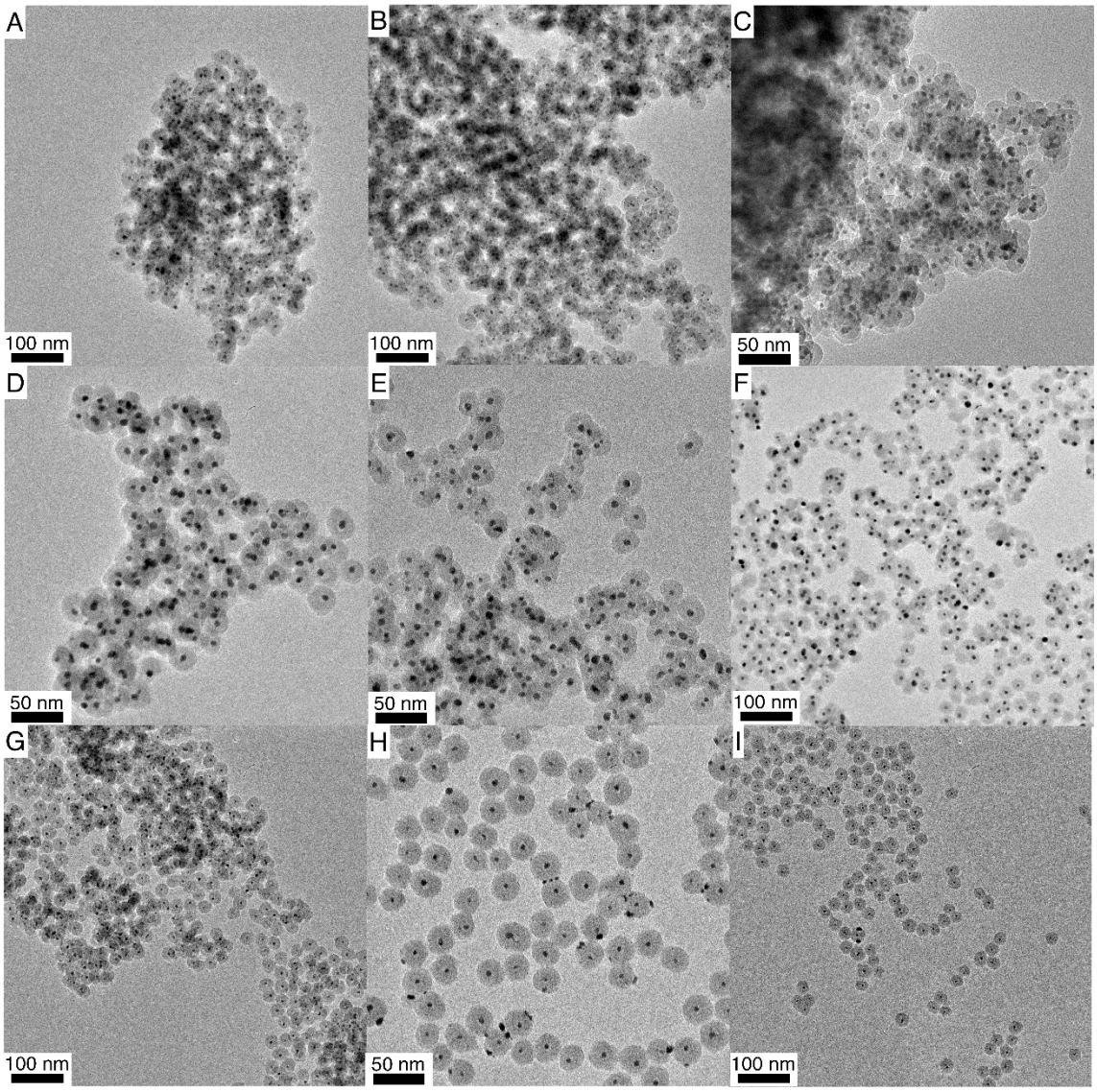

Fig. S23. TEM analysis of NPs with varying shell composition encapsulated in silica.

TEM images for a representative selection of different NM/TMC core-shell NPs encapsulated in silica after carburization at 900˚C-1000˚C in a 15% CH_4/85% H_2 atmosphere. All percentages are based on total metals basis as determined by ICP.

(A) 6.1 ± 0.9nm 26% $Pt_{0.6}Rh_{0.4}$ / 74% $Ti_{0.1}W_{0.9}C$
(B) 6.4 ± 1.0nm 27% $Pt_{0.5}Ru_{0.5}$ / 73% $Ti_{0.1}W_{0.9}C$
(C) 5.7 ± 1.1nm 25% $Pt_{0.8}Ir_{0.2}$ / 75% $Ti_{0.2}W_{0.8}C$
(D) 6.1 ± 1.0nm 17% $Pt_{0.93}Au_{0.07}$ / 83% $Ti_{0.1}W_{0.9}C$
(E) 9.7 ± 2.0nm 27% $Pt_{0.7}Au_{0.3}$ / 73% $Ti_{0.2}W_{0.8}C$
(F) 7.7 ± 1.4nm 28% Pt / 72% $Ti_{0.1}W_{0.9}C$ ($Pt_{C\text{-}S}$)
(G) 2.9 ± 0.6nm 13% Au / 87% $Ti_{0.3}W_{0.7}C$
(H) 3.5 ± 1.0nm 6% Au / 94% $Ti_{0.2}W_{0.8}C$
(I) 3.7 ± 1.3nm 4% Pt / 96% $Ti_{0.1}W_{0.9}C$

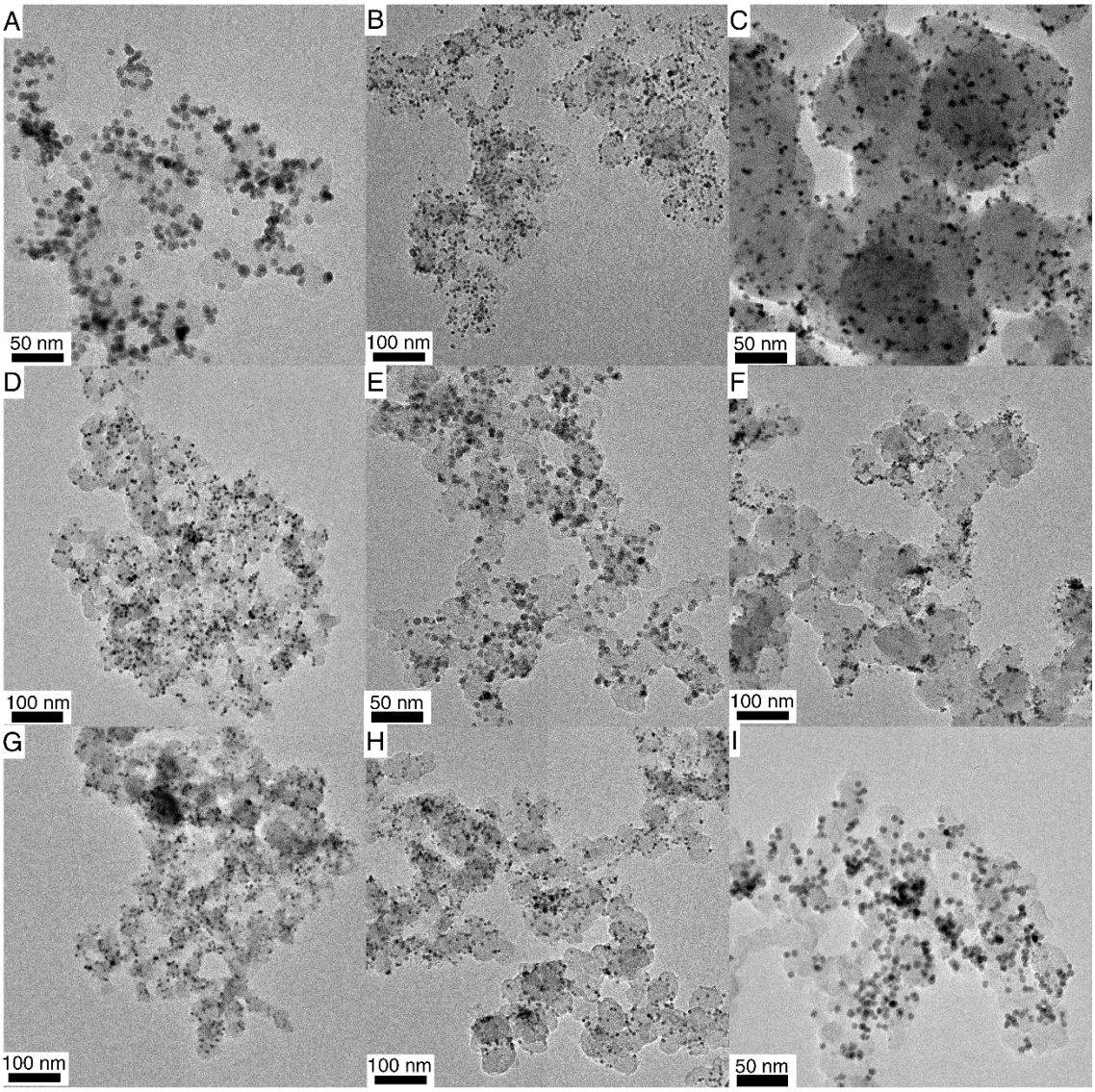

Fig. S24. TEM analysis of NPs with varying shell composition supported on carbon.

TEM images for a representative selection of different NM/TMC core-shell NPs supported on Vulcan® XC-72r carbon black after removal of the silica template.

(A) 7.7 ± 1.4nm 28% Pt / 72% $Ti_{0.1}W_{0.9}C$ NPs supported on carbon ($Pt_{C\text{-}S}$)
(B) 7.1 ± 1.4nm 21% Pt / 79% $Ti_{0.1}W_{0.9}C$ NPs supported on carbon
(C) 2.9 ± 0.6nm 13% Au / 87% $Ti_{0.1}W_{0.9}C$ NPs supported on carbon
(D) 6.1 ± 0.9nm 26% $Pt_{0.6}Rh_{0.4}$ / 74% $Ti_{0.1}W_{0.9}C$ NPs supported on carbon
(E) 5.7 ± 1.1nm 25% $Pt_{0.8}Ir_{0.2}$ / 75% $Ti_{0.2}W_{0.8}C$ NPs supported on carbon
(F) 6.1 ± 1.0nm 17% $Pt_{0.93}Au_{0.07}$ / 83% $Ti_{0.1}W_{0.9}C$ NPs supported on carbon
(G) 4.4 ± 0.8nm 14% $Pt_{0.6}Ru_{0.4}$ / 86% $Ti_{0.2}W_{0.8}C$ NPs supported on carbon
(H) 6.4 ± 1.0nm 27% $Pt_{0.5}Ru_{0.5}$ / 73% $Ti_{0.1}W_{0.9}C$ NPs supported on carbon
(I) 6.7 ± 1.0nm 27% $Pt_{0.67}Ru_{0.33}$ / 83% $Ti_{0.1}W_{0.9}C$ NPs supported on carbon ($PtRu_{C\text{-}S}$)

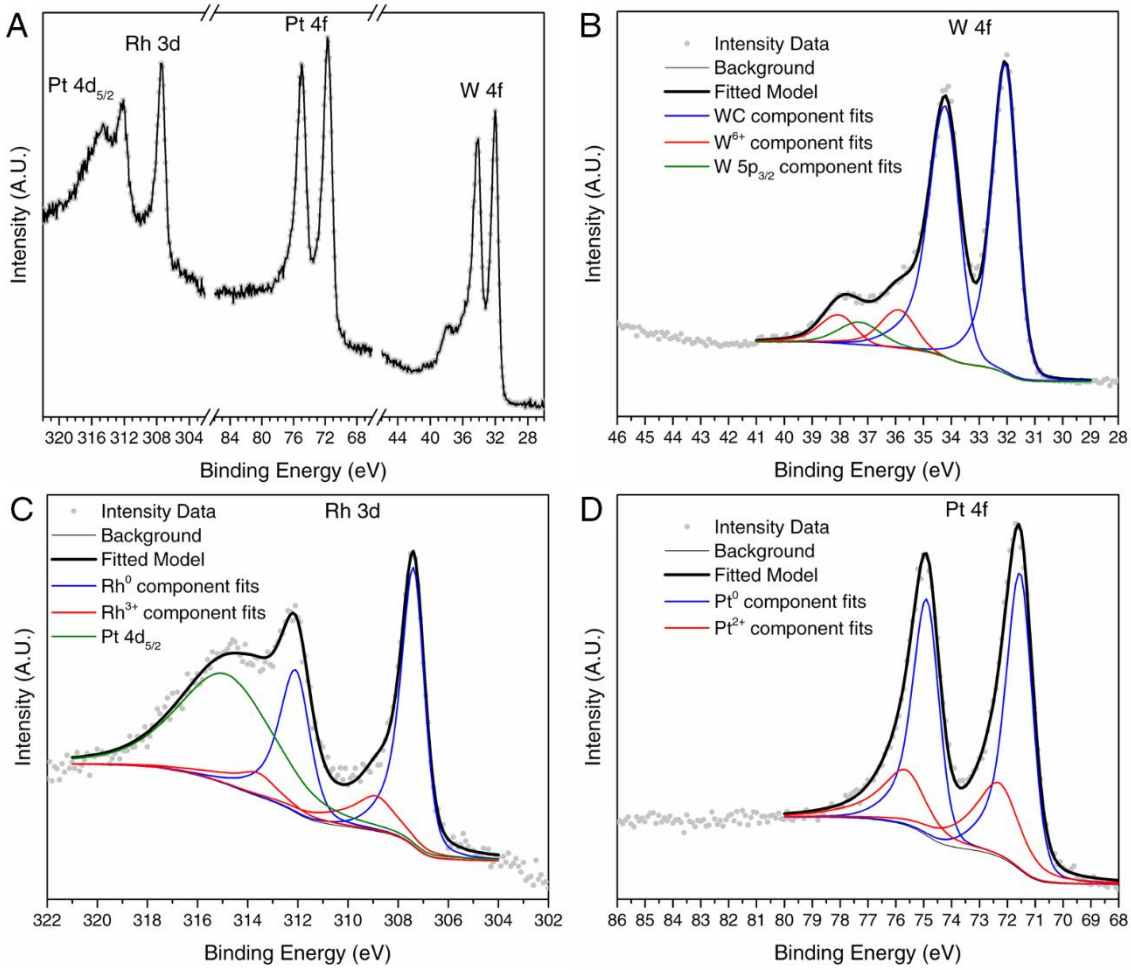

Fig. S25. XPS analysis of PtRh/TiWC NPs.

(A) Raw XPS intensity data obtained for 26%$Pt_{0.6}Rh_{0.4}$/74% $Ti_{0.1}W_{0.9}C$ core-shell NP nanoaggregates.

(B) XPS peak deconvolution of the W 4f spectrum.

(C) XPS peak deconvolution of the Rh 3d spectrum.

(D) XPS peak deconvolution of the Pt 4f spectrum.

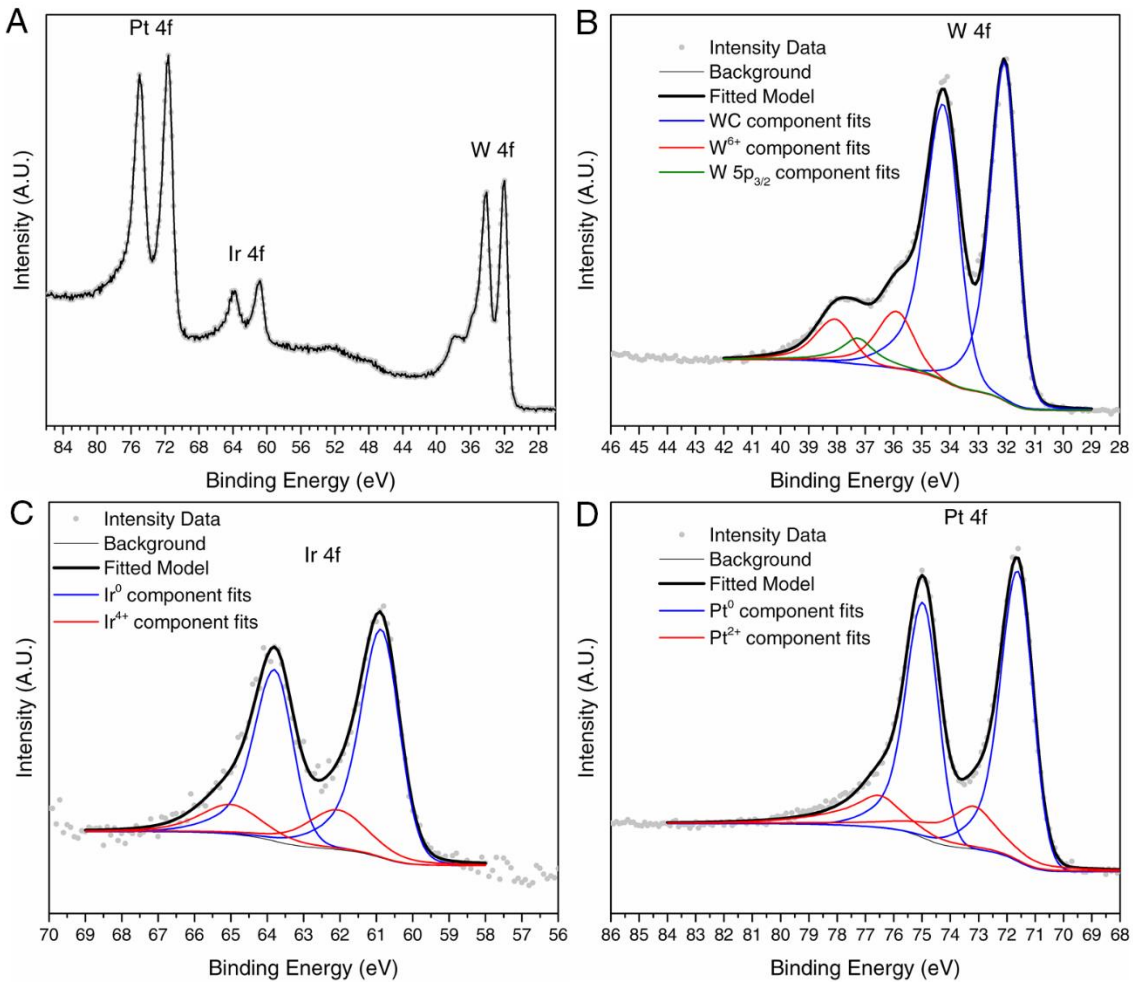

Fig. S26. XPS analysis of PtIr/TiWC NPs.

(A) Raw XPS intensity data obtained for 25%$Pt_{0.8}Ir_{0.2}$/75%$Ti_{0.2}W_{0.8}C$ core-shell NP nanoaggregates.

(B) XPS peak deconvolution of the W 4f spectrum.

(C) XPS peak deconvolution of the Ir 4f spectrum.

(D) XPS peak deconvolution of the Pt 4f spectrum.

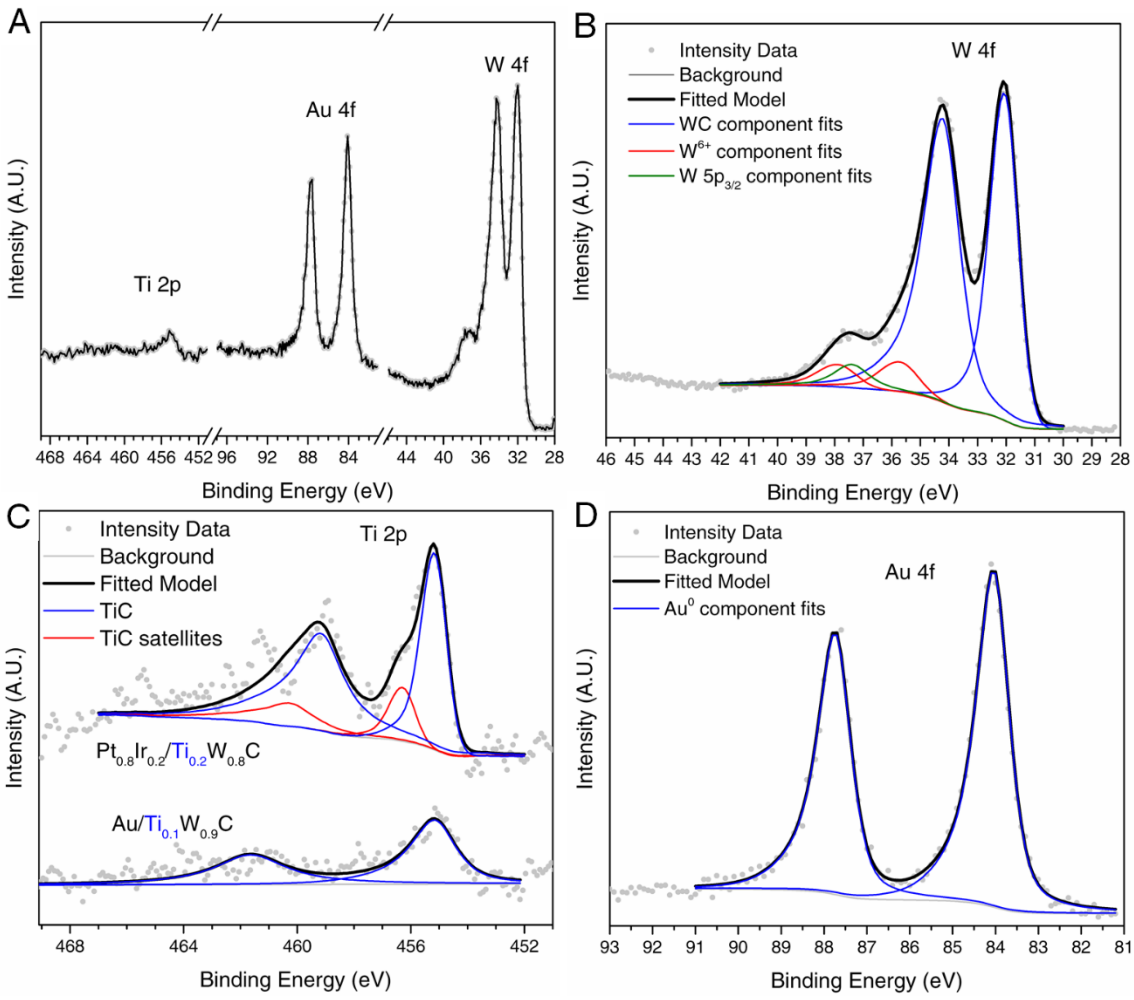

Fig. S27. XPS analysis of Au/TiWC NPs.

(A) Raw XPS intensity data obtained for 13%Au/$Ti_{0.1}W_{0.9}C$ core-shell NP nanoaggregates.

(B) XPS peak deconvolution of the W 4f spectrum.

(C) XPS peak deconvolution of the Ti 2p spectrum. The Ti 2p spectrum is difficult to deconvolute for three reasons: the atomic sensitivity factor is low for ejected Ti 2p photoelectrons, the Ti concentration is low in the carbide cores, and the Ti signal is screened by the overlayer of noble metals. For these reasons, the Ti 2p spectrum for $Pt_{0.8}Ir_{0.2}/Ti_{0.2}W_{0.8}C$ is shown. This is a representative core-shell material with a higher core percentage of Ti. In cases where the core percentage is 10%, a deconvolution is difficult to perform and instead an estimate of the Ti composition is obtained from simple integration as shown for the Ti 2p spectrum for $Au/Ti_{0.1}W_{0.9}C$.

(D) XPS peak deconvolution of the Au 4f spectrum.

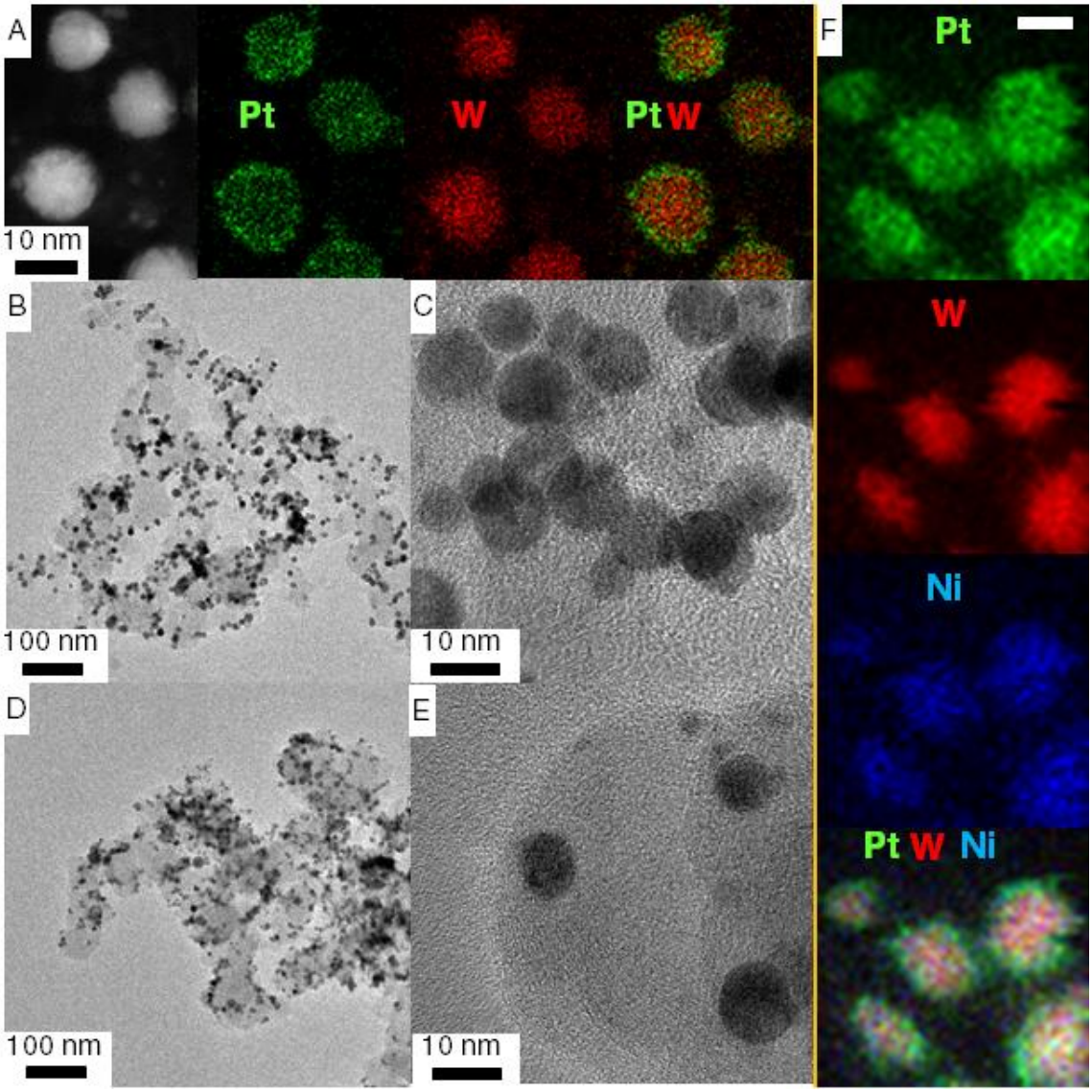

Fig. S28. Microscopic analysis of NPs with varying core compositions.

(A) STEM-EDX maps and **(B,C)** TEM images of 26%Pt/$(Cu_{0.2}W_{0.8})_2C$ supported on carbon black.

(D, E) TEM images of 23%Pt/$(Co_{0.2}W_{0.8})_2C$ supported on carbon black.

(F) STEM-EDX maps of 16%Pt/$(Ni_{0.3}W_{0.7})_2C$ supported on carbon black. The scale bar shown for Pt is 10 nm and applies to all micrographs.

The PXRD patterns of these material are shown in Fig 4C.

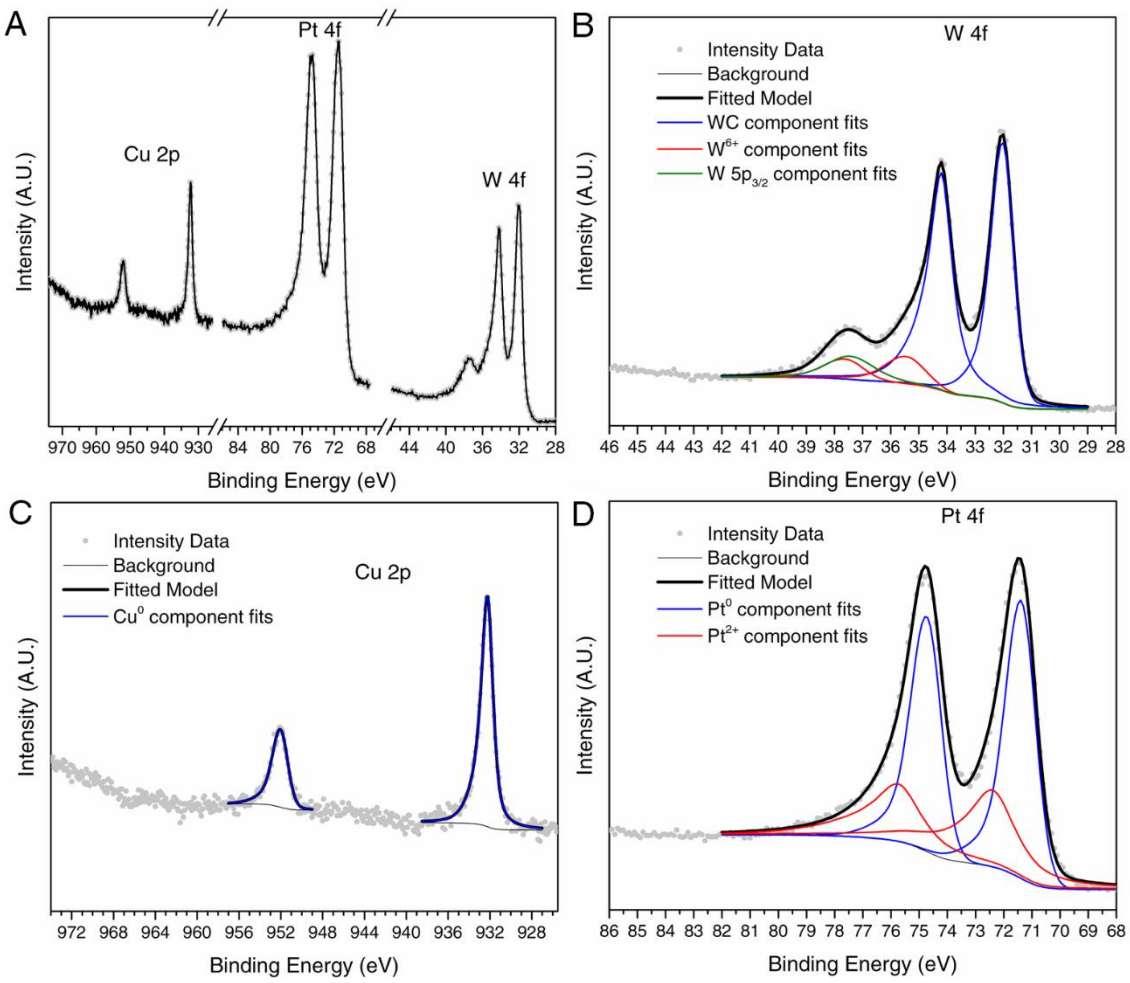

Fig. S29. XPS analysis of Pt/CuWC NPs.

(A) Raw XPS intensity data obtained for 26%Pt/$(Cu_{0.2}W_{0.8})_2C$ core-shell NP nanoaggregates. Quantitative results are shown in Table S5.

(B) XPS peak deconvolution of the W 4f spectrum.

(C) XPS peak deconvolution of the Cu 2p spectrum.

(D) XPS peak deconvolution of the Pt 4f spectrum.

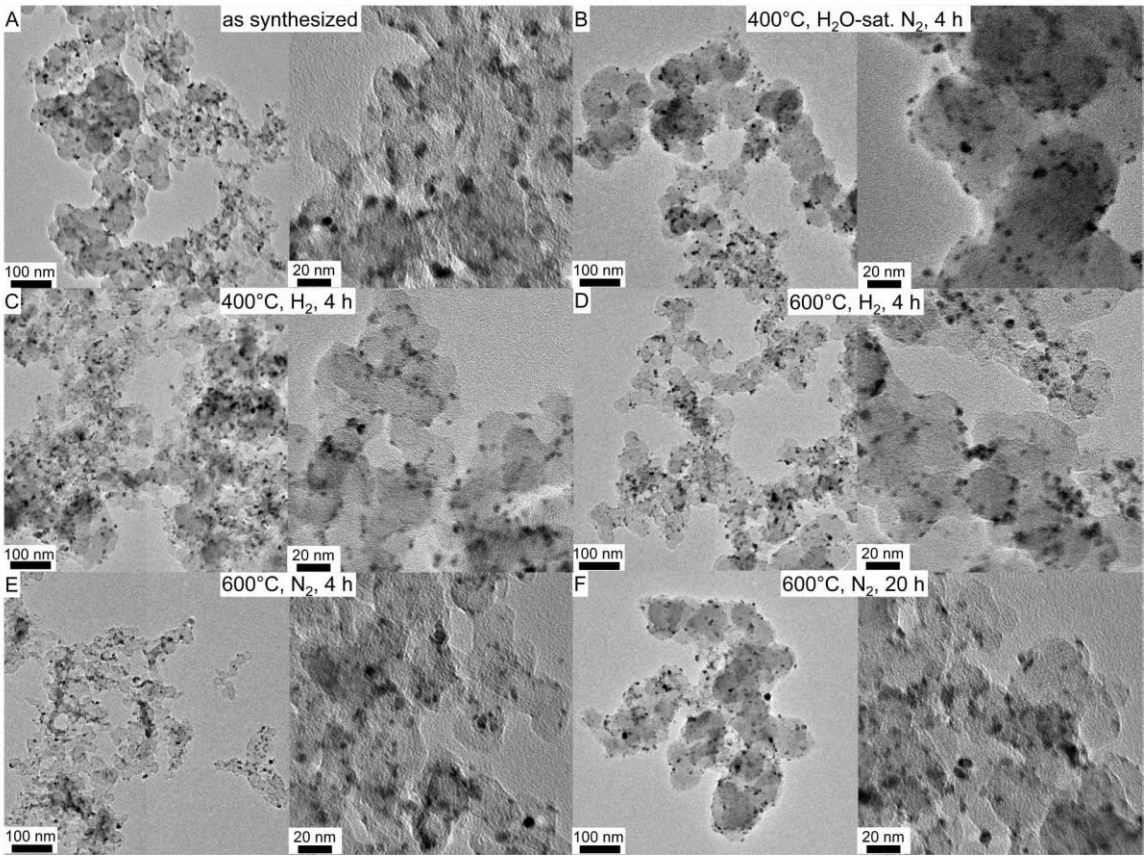

Fig. S30. Microscopic analysis of $Pt_{sub\text{-}ML}$ after various heat treatments.

TEM images of 20 wt% carbon-supported 4%Pt/96% $Ti_{0.1}W_{0.9}C$ NPs (denoted as $Pt_{sub\text{-}ML}$) after various heat treatments in different atmospheres.

(A) As synthesized

(B) After the treatment at 400˚C in wet N_2 for 4 h

(C) After the treatment at 400˚C in H_2 for 4 h

(D) After the treatment at 600˚C in H_2 for 4 h

(E) After the treatment at 600˚C in N_2 for 4 h

(F) After the treatment at 600˚C in N_2 for 20 h

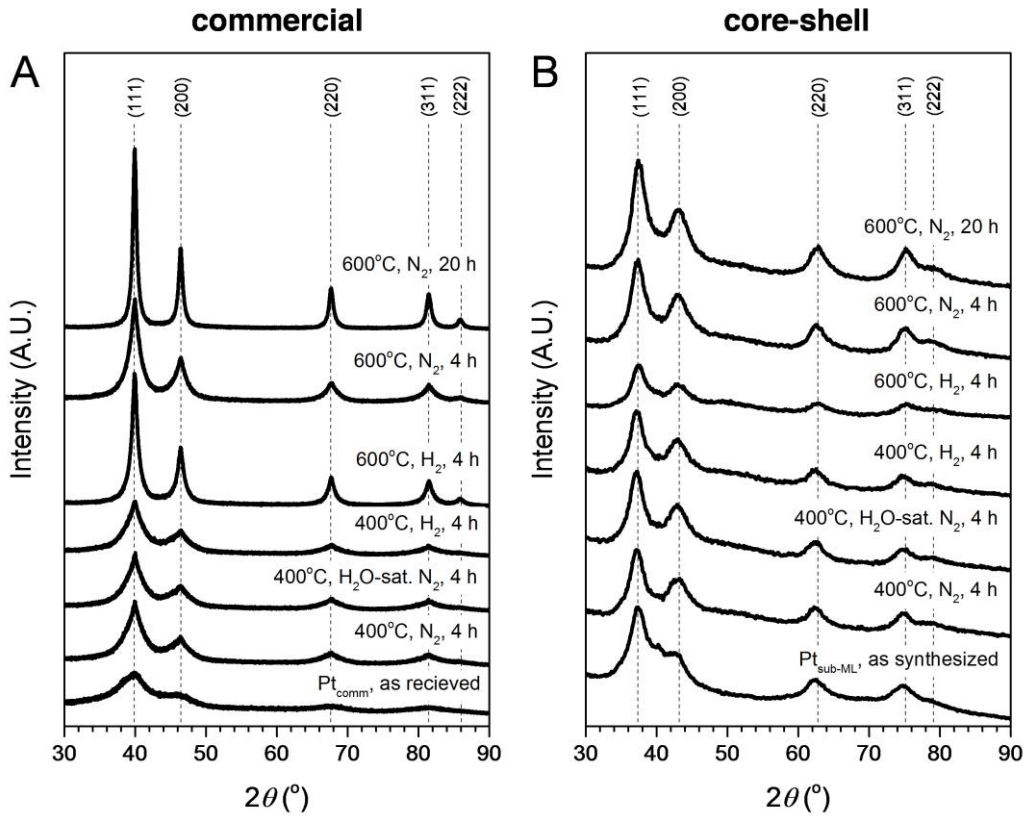

Fig. S31. PXRD analysis of Pt_{comm} and $Pt_{sub\text{-}ML}$ after various heat treatments.

PXRD diffractograms of **(A)** Pt_{comm} and **(B)** $Pt_{sub\text{-}ML}$ heated to 400 or 600˚C in different atmospheres (H_2, dry and wet N_2 flow) for 4 or 20 h.

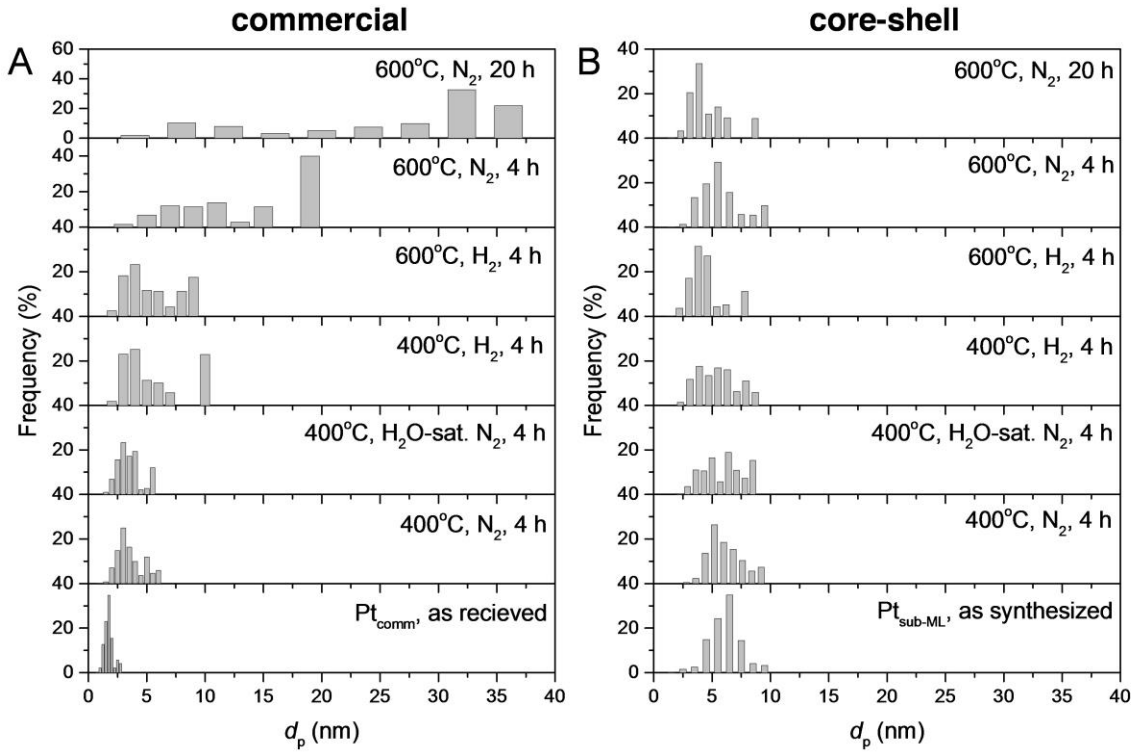

Fig. S32. Impact of various heat treatments on the PSDs of Pt_{comm} and $Pt_{sub\text{-}ML}$.
Volume-weighted particle size distribution (PSD) plots for **(A)** Pt_{comm} and **(B)** $Pt_{sub\text{-}ML}$ after various heat treatments in different atmospheres. The PSDs were determined from at least 200 nanoparticles from several images taken across the TEM grids.

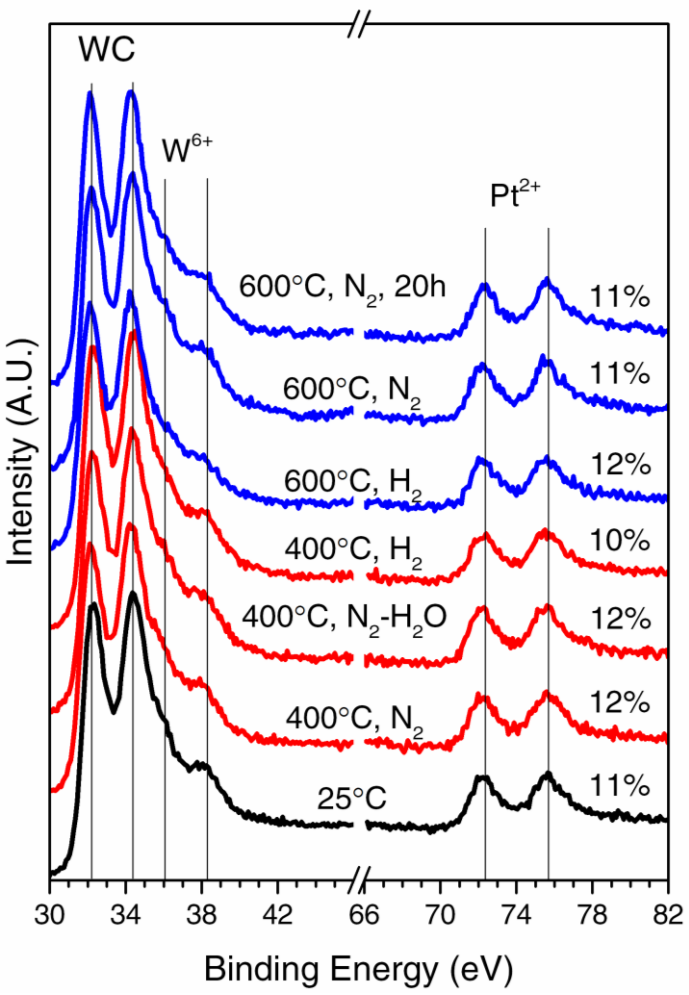

Fig. S33. XPS analysis of $Pt_{sub\text{-}ML}$ after various heat treatments.

XPS study of the thermal stability of $Pt_{sub\text{-}ML}$ held in various atmospheres for 4 or 20 h and then passivated at room temperature. The percentages shown correspond to the XPS-determined Pt:W ratios and range from 10-12%. The ICP-determined bulk Pt:W ratio was 5%.

Table S1. Electrochemical active surface areas of core-shell and commercial catalysts.

Electrochemical active surface areas were determined from triplicate electrode mountings using CO-stripping voltammetry (CO-ECSA) and underpotentially deposited hydrogen (H_{upd}-ECSA). The average roughness factors determined from CO-stripping voltammetry (CO-r_f) are also reported. The CO-ECSA/H_{upd}-ECSA ratio is also provided where appropriate. H_{upd}-ECSA is not reported for $PtRu_{comm}$ as it is poorly defined for this material (*58*). Specific activities were computed for each electrode mounting by dividing its geometric current density by its measured CO-r_f value.

Catalysts	CO-r_f ($cm^2_{NM}\ cm^{-2}_{geo}$)	CO-ECSA ($m^2\ g^{-1}_{NM}$)	H_{upd}-ECSA ($m^2\ g^{-1}_{NM}$)	CO-ECSA / H_{upd}-ECSA
Pt_{comm}	34.6 ± 3.0	67.9 ± 5.8	68.0 ± 7.0	1.00 ± 0.02
$PtRu_{comm}$	50.3 ± 3.6	98.9 ± 7.1	N.R.	N.R.
$Pt_{C\text{-}S}$	10.2 ± 0.4	49.9 ± 2.2	54.9 ± 6.6	0.92 ± 0.07
$PtRu_{C\text{-}S}$	14.1 ± 0.3	72.8 ± 1.5	46.4 ± 2.0	1.53 ± 0.05

N.R. - not reported

Table S2. Tafel analysis of the HOR and HER LSVs from GDE and RDE measurements.

Exchange current densities (j_o) and Tafel slopes (b) as determined from both the HOR and HER LSVs (shown in Fig. 3A and fig. S13) using a GDE in 1 M $HClO_4$ and 0.1 M $HClO_4$. Also shown are j_o and b values determined from both HOR and HER LSVs (fig. S12A) obtained using an RDE in 0.1 M $HClO_4$. Linear fits for all materials were performed at overpotentials from 15 to 30 mV. The reported errors are propagated from the standard errors in the regression. For the RDE measurements, the kinetic HOR current was obtained from the Koutecky-Levich equation. We note that HOR/HER kinetics of platinum group metals are exceptionally fast (*59*), making the kinetic analysis from the RDE underestimated and the GDE data more reliable (*40, 41*). While the RDE data is only included for comparison, it is likely still relevant to the operating activity of an integrated device (*60*).

GDE in 1.0 M $HClO_4$, H_2 purge, 30 ˚C, 10 mV s^{-1}

Catalyst	HOR j_o (mA cm^{-2})	HER j_o (mA cm^{-2})	HOR b (mV dec^{-1})	HER b (mV dec^{-1})
Pt_{comm}	24.4 ± 4.0	25.8 ± 4.5	31.9 ± 1.0	33.3 ± 1.1
$PtRu_{comm}$	26.7 ± 4.7	29.1 ± 4.9	33.3 ± 1.1	32.3 ± 1.0
Pt_{C-S}	32.8 ± 6.3	35.4 ± 6.1	34.1 ± 1.2	30.8 ± 0.9
$PtRu_{C-S}$	34.2 ± 6.0	34.4 ± 6.4	33.1 ± 1.0	32.4 ± 1.0

GDE in 0.1 M $HClO_4$, H_2 purge, 30 ˚C, 10 mV s^{-1}

Catalyst	HOR j_o (mA cm^{-2})	HER j_o (mA cm^{-2})	HOR b (mV dec^{-1})	HER b (mV dec^{-1})
Pt_{comm}	3.45 ± .25	3.72 ± .31	32.6 ± .9	35.1 ± 1.1
$PtRu_{comm}$	4.30 ± .39	4.52 ± .41	33.1 ± 1.0	33.6 ± 1.0
Pt_{C-S}	3.77 ± .29	4.05 ± .34	33.5 ± 1.0	33.8 ± 1.0
Pt_{C-S} post 10,000	3.21 ± .23	3.42 ± .26	33.3 ± 1.0	34.1 ± 1.0
$PtRu_{C-S}$	4.60 ± .41	4.64 ± .43	35.1 ± 1.1	34.1 ± 1.1
$PtRu_{C-S}$ post 10,000	4.20 ± .35	4.18 ± .37	33.8 ± 1.0	31.5 ± 1.0

RDE in 0.1 M $HClO_4$, H_2-saturated, 30 ˚C, 10 mV s^{-1}, 1600 rpm

Catalyst	HOR j_o (mA cm^{-2})	HER j_o (mA cm^{-2})	HOR b (mV dec^{-1})	HER b (mV dec^{-1})
Pt_{comm}	1.14 ± .04	1.13 ± .04	30.6 ± .6	32.4 ± .9
$PtRu_{comm}$	1.14 ± .04	1.14 ± .03	33.8 ± .7	33.5 ± .7
Pt_{C-S}	1.06 ± .03	1.03 ± .05	28.3 ± .4	32.4 ± 1.0
Pt_{C-S} post 10,000	1.09 ± .02	1.29 ± .04	28.3 ± .3	31.8 ± .9
$PtRu_{C-S}$	1.11 ± .03	1.16 ± .04	29.6 ± .5	31.3 ± .8
$PtRu_{C-S}$ post 10,000	1.03 ± .03	1.25 ± .04	28.5 ± .4	29.6 ± .7

Note that the theoretical Tafel slope is 30 mV dec^{-1} for a 2-electron reaction where the rate-limiting step is Tafel recombination. Furthermore, the equivalent j_o and b for HER and HOR imply a symmetric charge transfer coefficient (β) of 0.5. All materials tested above exhibit Tafel slopes close to the theoretical value. The similarity between the HOR and HER j_o and b values implies near-symmetric charge transfer for all materials.

Table S3. HER activity determined using chronopotentiometry (CP) and chronoamperometry (CA).

The measurements were performed in H_2-saturated 0.1 M $HClO_4$ at 30˚C under a rotation rate of 2500 rpm. Initial activities were averaged from triplicate electrode mountings. $\eta@j_{geo=10}$ is the overpotential required to drive a geometric current density of 10 mA cm^{-2} as determined by CP measurements. Conversely, $j_{geo}@\eta=50mV$ is the geometric current density achieved at a fixed overpotential of 50 mV as determined by CA measurements. The achieved current densities were also normalized by surface sites (determined from CO-stripping measurements) to obtain $j_{specific}@\eta=50mV$ and by mass of NM loaded to obtain $j_{mass}@\eta=50mV$. The specific activity was used to determine the turnover frequency (TOF@η=50mV), where the TOF is given as mol H_2 per mol of surface sites per second.

Catalyst	$\eta@j_{geo=10}$ (mV)	$j_{geo}@\eta=50mV$ (mA cm^{-2}_{geo})	$j_{specific}@\eta=50mV$ (μA $cm^{-2}_{CO\text{-}ECSA}$)	$j_{mass}@\eta=50mV$ (mA mg^{-1}_{NM})	TOF@η=50mV (s^{-1})
Pt_{comm}	39.4 ± .7	13.1 ± .2	379 ± 33	258 ± 4	0.80 ± 0.08
$PtRu_{comm}$	42.4 ± .8	13.7 ± .3	272 ± 20	269 ± 6	0.65 ± 0.05
$Pt_{C\text{-}S}$	37.5 ± .9	15.1 ± .4	1482 ± 76	740 ± 20	3.53 ± 0.18
$Pt_{C\text{-}S}$ post 10,000	43.8 ± .7	12.4 ± .1	1221 ± 5	610 ± 3	2.91 ± 0.01
$PtRu_{C\text{-}S}$	38.1 ± 1.2	13.9 ± .7	987 ± 58	719 ± 40	2.35 ± 0.14
$PtRu_{C\text{-}S}$ post 10,000	38.2 ± .3	14.4 ± .1	1226 ± 8	742 ± 4	3.01 ± 0.02
Pt_{direct}	148 ± 4	0.45 ± .03	N.R.	N.R.	N.R.
Vulcan Carbon	594 ± 6	0.03 ± .00	N.R.	N.R.	N.R.

N.R. - not reported

Table S4. MOR initial and post-stability steady-state kinetic estimates

Kinetic estimates were obtained from steady-state chronoamperometry measurements performed over 15 min intervals held at fixed potentials. The data is shown in Fig. 3E and fig. S18. Turnover frequencies (TOFs) were estimated from the steady-state activity measurements at 0.45 V and 0.6 V assuming complete 6-electron transfer oxidations normalized by CO-ECSA roughness factors. This assumption is reasonable for $PtRu_{comm}$ and $PtRu_{C\text{-}S}$ at both 0.45 and 0.6 V (*58*). As such, TOF estimates are given as mol CO_2 per mol of surface sites per minute.

Catalyst	TOF@0.45 V Initial (min^{-1})	TOF@0.45 V Post 10,000 and Regeneration (min^{-1})	TOF@0.6 V Initial (min^{-1})	TOF@0.6 V Post 10,000 and Regeneration (min^{-1})
Pt_{comm}	0.00 ± .00	0.00 ± .00	0.96 ± .08	1.11 ± .10
$Pt_{C\text{-}S}$	0.03 ± .00	0.02 ± .00	1.55 ± .07	1.83 ± .08
$PtRu_{comm}$	0.86 ± .06	0.38 ± .03	3.65 ± .26	2.35 ± .17
$PtRu_{C\text{-}S}$	2.20 ± .05	1.80 ± .04	15.87 ± .37	25.69 ± .53

Table S5. Chemical composition of core-shell materials.

Bulk chemical composition determined by ICP and surface chemical composition derived using deconvoluted XPS spectra shown in Figs. S6, S7, S25-27, S29, and Fig. 2B.

	ICP-determined bulk composition			XPS-determined surface composition			Estimated number of ML
Material	NM ratio	TMC ratio	NM:TMC ratio	NM ratio	TMC ratio[1]	NM:TMC ratio	
Au/TiWC	Au	$Ti_{0.10}W_{0.90}$	**6%**	Au	N.R.	**7%**	~ 0.5
Au/TiWC	Au	$Ti_{0.18}W_{0.82}$	**13%**	Au	$Ti_{0.12}W_{0.88}$	**22%**	~ 1
Au/TiWC	Au	$Ti_{0.14}W_{0.86}$	**29%**	Au	N.R.	**37%**	~ 2-3
Pt/TiWC	Pt	$Ti_{0.08}W_{0.92}$	**3%**	Pt	N.R.	**6%**	< 0.5
Pt/TiWC	Pt	$Ti_{0.10}W_{0.90}$	**9%**	Pt	N.R.	**26%**	~ 1
$Pt_{C\text{-}S}$	Pt	$Ti_{0.10}W_{0.90}$	**28%**	Pt	$Ti_{0.10}W_{0.90}$	**49%**	~ 2-3
$Pt/(CuW)_2C$	Pt	$Cu_{0.23}W_{0.77}$	**26%**	Pt	$Cu_{0.22}W_{0.78}$	**52%**	~ 2-3
$PtRu_{C\text{-}S}$	$Pt_{0.67}Ru_{0.33}$	$Ti_{0.11}W_{0.89}$	**27%**	$Pt_{0.76}Ru_{0.24}$	$Ti_{0.10}W_{0.90}$	**43%**	~ 2-3
PtRh/TiWC	$Pt_{0.57}Rh_{0.43}$	$Ti_{0.13}W_{0.87}$	**26%**	$Pt_{0.59}Rh_{0.41}$	$Ti_{0.13}W_{0.87}$	**52%**	~ 2-3
PtIr/TiWC	$Pt_{0.81}Ir_{0.19}$	$Ti_{0.21}W_{0.79}$	**25%**	$Pt_{0.81}Ir_{0.19}$	$Ti_{0.18}W_{0.82}$	**45%**	~ 2-3
PtAu/TiWC	$Pt_{0.93}Au_{0.07}$	$Ti_{0.11}W_{0.89}$	**26%**	$Pt_{0.94}Au_{0.06}$	N.R.	**55%**	~ 2-3
PtAu/TiWC	$Pt_{0.69}Au_{0.31}$	$Ti_{0.18}W_{0.82}$	**27%**	$Pt_{0.73}Au_{0.27}$	$Ti_{0.16}W_{0.84}$	**45%**	~ 2-3

[1] TMC ratio is not reported as in some spectra the Ti 2p signal was not useable to estimate the surface intensity of Ti for reasons discussed in fig. S26.

For multilayer core-shell NM/TMC NPs, the XPS-derived NM:TMC atomic ratio is much higher than the bulk NM:TMC ratio determined by ICP. Consistent with the PXRD data, TEM images, and STEM-EDX maps, this suggests a core-shell configuration in which the NM monolayers screen the XPS signal of the sub-surface TMC core (*61*). Concurrently, the close agreement between the XPS- and ICP-determined concentrations of elements in the bimetallic cores confirms that they are equally screened by the surface NMs. Similarly, the equivalent bimetallic NM composition determined by these two techniques indicates little partitioning of NMs into the carbide core.

Expressed another way, consider a nanoparticle with 4 elements (*a*, *b*, *c*, and *d*), each comprising 25 mol% of the nanoparticle. This value represents the bulk composition that can be determined using ICP. If the nanoparticle is radially isotropic, the surface composition probed by XPS will agree with the bulk composition obtained by ICP and a composition of 25 mol% for each element would be obtained. That is, all surface elements screen the subsurface elements equally. However, if two of the elements, e.g., *a* and *b*, are not radially isotropic, but enriched at the surface (as is expected to occur in a core-shell particle), the XPS data will not agree with the ICP data. The concentrations of *a* and *b* will be higher than 25%, while the concentrations of *c* and *d* will be less than 25% because *a* and *b* now screen the XPS signal of *c* and *d*. The extent of this screening enrichment depends on the thickness of the *a* and *b* surface layer. If the XPS ratio of *a*:*b* is still 1:1, then both *a* and *b* are partitioned comparably at the surface shell in the radial direction. Similarly, if the XPS ratio of *c*:*d* is still 1:1, then both are partitioned comparably at the subsurface core in the radial direction.

Supporting References

1. A. T. Bell, The impact of nanoscience on heterogeneous catalysis. *Science* **299**, 1688-1691 (2003).
2. G. A. Deluga, J. R. Salge, L. D. Schmidt, X. E. Verykios, Renewable hydrogen from ethanol by autothermal reforming. *Science* **303**, 993-997 (2004).
3. J. Zhang, K. Sasaki, E. Sutter, R. R. Adzic, Stabilization of platinum oxygen-reduction electrocatalysts using gold clusters. *Science* **315**, 220-222 (2007).
4. Y. Zhai *et al.*, Alkali-stabilized Pt-OHx species catalyze low-temperature water-gas shift reactions. *Science* **329**, 1633-1636 (2010).
5. L. Zhang *et al.*, Platinum-based nanocages with subnanometer-thick walls and well-defined, controllable facets. *Science* **349**, 412-416 (2015).
6. C. Chen *et al.*, Highly crystalline multimetallic nanoframes with three-dimensional electrocatalytic surfaces. *Science* **343**, 1339-1343 (2014).
7. J. Greeley *et al.*, Alloys of platinum and early transition metals as oxygen reduction electrocatalysts. *Nature Chem.* **1**, 552-556 (2009).
8. P. Strasser *et al.*, Lattice-strain control of the activity in dealloyed core-shell fuel cell catalysts. *Nat Chem* **2**, 454-460 (2010).
9. H. Yang, Platinum-based electrocatalysts with core–shell nanostructures. *Angew. Chem. Int. Ed.* **50**, 2674-2676 (2011).
10. F. Tao *et al.*, Reaction-driven restructuring of Rh-Pd and Pt-Pd core-shell nanoparticles. *Science* **322**, 932-934 (2008).
11. S. Alayoglu, A. U. Nilekar, M. Mavrikakis, B. Eichhorn, Ru-Pt core-shell nanoparticles for preferential oxidation of carbon monoxide in hydrogen. *Nat. Mater.* **7**, 333-338 (2008).
12. C. S. Bonifacio *et al.*, Thermal stability of core–shell nanoparticles: a combined in situ study by XPS and TEM. *Chem. Mater.* **27**, 6960-6968 (2015).
13. C. Cui, L. Gan, M. Heggen, S. Rudi, P. Strasser, Compositional segregation in shaped Pt alloy nanoparticles and their structural behaviour during electrocatalysis. *Nat. Mater.* **12**, 765-771 (2013).
14. C. Wang *et al.*, Correlation between surface chemistry and electrocatalytic properties of monodisperse PtxNi1-x nanoparticles. *Adv. Funct. Mater.* **21**, 147-152 (2011).
15. D. V. Esposito, J. G. Chen, Monolayer platinum supported on tungsten carbides as low-cost electrocatalysts: opportunities and limitations. *Energy Environ. Sci.* **4**, 3900-3912 (2011).
16. I. E. Stephens, A. S. Bondarenko, U. Grønbjerg, J. Rossmeisl, I. Chorkendorff, Understanding the electrocatalysis of oxygen reduction on platinum and its alloys. *Energy Environ. Sci.* **5**, 6744-6762 (2012).
17. J. A. Schaidle, N. M. Schweitzer, O. T. Ajenifujah, L. T. Thompson, On the preparation of molybdenum carbide-supported metal catalysts. *J. Catal.*, (2012).
18. S. T. Oyama, *The Chemistry of Transition Metal Carbides and Nitrides*. (Blackie, Glasgow, 1996).
19. S. Ono, T. Kikegawa, Y. Ohishi, A high-pressure and high-temperature synthesis of platinum carbide. *Solid State Commun.* **133**, 55-59 (2005).
20. R. B. Levy, M. Boudart, Platinum-like behavior of tungsten carbide in surface catalysis. *Science* **181**, 547-549 (1973).

21. L. H. Bennett, J. R. Cuthill, A. J. McAlister, N. E. Erickson, R. E. Watson, Electronic structure and catalytic behavior of tungsten carbide. *Science* **184**, 563-565 (1974).
22. D. V. Esposito, S. T. Hunt, Y. C. Kimmel, J. G. Chen, A new class of electrocatalysts for hydrogen production from water electrolysis: metal monolayers supported on low-cost transition metal carbides. *J. Am. Chem. Soc.* **134**, 3025-3033 (2012).
23. T. G. Kelly, A. L. Stottlemyer, H. Ren, J. G. Chen, Comparison of O−H, C−H, and C−O bond scission sequence of methanol on tungsten carbide surfaces modified by Ni, Rh, and Au. *J. Phys. Chem. C* **115**, 6644-6650 (2011).
24. S. T. Hunt, T. Nimmanwudipong, Y. Roman-Leshkov, Engineering non-sintered, metal-terminated tungsten carbide nanoparticles for catalysis. *Angew. Chem. Int. Ed.* **53**, 5131-5136 (2014).
25. See supporting material on *Science* Online.
26. Y. C. Kimmel, X. Xu, W. Yu, X. Yang, J. G. Chen, Trends in electrochemical stability of transition metal carbides and their potential use as supports for low-cost electrocatalysts. *ACS Catal.* **4**, 1558-1562 (2014).
27. W. Schottky, Über spontane stromschwankungen in verschiedenen elektrizitätsleitern. *Annalen der Physik* **362**, 541-567 (1918).
28. B. Hammer, Y. Morikawa, J. Norskov, CO chemisorption at metal surfaces and overlayers. *Phys. Rev. Lett.* **76**, 2141-2144 (1996).
29. Z. Liu, G. S. Jackson, B. W. Eichhorn, PtSn intermetallic, core-shell, and alloy nanoparticles as CO-tolerant electrocatalysts for H2 oxidation. *Angew. Chem. Int. Ed. Engl.* **49**, 3173-3176 (2010).
30. T. J. Schmidt, H. A. Gasteiger, R. J. Behm, Methanol electrooxidation on a colloidal PtRu-alloy fuel-cell catalyst. *Electrochem. Commun.* **1**, 1-4 (1999).
31. A. K. Singh, Q. Xu, Synergistic catalysis over bimetallic alloy nanoparticles. *ChemCatChem* **5**, 652-676 (2013).
32. R. Michalsky, Y. J. Zhang, A. J. Medford, A. A. Peterson, Departures from the adsorption energy scaling relations for metal carbide catalysts. *J. Phys. Chem. C* **118**, 13026-13034 (2014).
33. S. T. Hunt, T. M. Kokumai, D. Zanchet, Y. Roman-Leshkov, Alloying tungsten carbide nanoparticles with tantalum: impact on electrochemical oxidation resistance and hydrogen evolution activity. *J. Phys. Chem. C* **119**, 13691-13699 (2015).
34. S. T. Hunt, Y. Roman-Leshkov, Reverse microemulsion-mediated synthesis of monometallic and bimetallic early transition metal carbide and nitride nanoparticles. *J. Vis. Exp.* **e53147**, (2015).
35. M. Koenig, J. Grant, Signal-to-noise measurement in X-ray photoelectron spectroscopy. *Surf. Interface Anal.* **7**, 217-222 (1985).
36. T.J. Schmidt, H.A. Gasteiger, G.D. Stab, P.M. Urban, D.M. Kolb, and R.J. Behm, Characterization of High-Surface-Area Electrocatalysts Using a Rotating Disk Electrode Configuration. *J. Electrochem. Soc.* **145**, 2354-2358 (1998).
37. K. Shinozaki, J. W. Zack, R. M. Richards, B. S. Pivovar, S. S. Kocha, Oxygen Reduction Reaction Measurements on Platinum Electrocatalysts Utilizing Rotating Disk Electrode Technique I. Impact of Impurities, Measurement

Protocols and Applied Corrections. *J. Electrochem. Soc.* **162**, F1144-F1158 (2015).
38. K. Shinozaki, J. W. Zack, S. Pylypenko, B. S. Pivovar, S. S. Kocha, Oxygen Reduction Reaction Measurements on Platinum Electrocatalysts Utilizing Rotating Disk Electrode Technique II. Influence of Ink Formulation, Catalyst Layer Uniformity and Thickness. *J. Electrochem. Soc.* **162**, F1384-F1396 (2015).
39. T. Binninger, E. Fabbri, R. Kötz, T. Schmidt, Determination of the electrochemically active surface area of metal-oxide supported platinum catalyst. *J. Electrochem. Soc.* **161**, H121-H128 (2014).
40. K. Elbert *et al.*, Elucidating Hydrogen Oxidation/Evolution Kinetics in Base and Acid by Enhanced Activities at the Optimized Pt Shell Thickness on the Ru Core. *ACS Catal.* **5**, 6764-6772 (2015).
41. J. X. Wang, Y. Zhang, C. B. Capuano, K. E. Ayers, Ultralow charge-transfer resistance with ultralow Pt loading for hydrogen evolution and oxidation using Ru@ Pt core-shell nanocatalysts. *Sci. Rep.* **5**, 1-8 (2015).
42. G. Kresse, J. Furthmüller, Efficient iterative schemes for ab initio total-energy calculations using a plane-wave basis set. *Physical Review B* **54**, 11169-11186 (1996).
43. J. P. Perdew, K. Burke, M. Ernzerhof, Generalized Gradient Approximation Made Simple. *Phys. Rev. Lett.* **77**, 3865-3868 (1996).
44. F. Finocchi, A. Barbier, J. Jupille, C. Noguera, Stability of Rocksalt (111) Polar Surfaces: Beyond the Octopole. *Phys. Rev. Lett.* **92**, 136101 (2004).
45. D. O. Scanlon *et al.*, Surface Sensitivity in Lithium-Doping of MgO: A Density Functional Theory Study with Correction for on-Site Coulomb Interactions. *J. Phys. Chem. C* **111**, 7971-7979 (2007).
46. J. K. Nørskov *et al.*, Trends in the exchange current for hydrogen evolution. *J. Electrochem. Soc.* **152**, J23-J26 (2005).
47. K. T. Butler, C. H. Hendon, A. Walsh, Electronic Chemical Potentials of Porous Metal–Organic Frameworks. *J. Am. Chem. Soc.* **136**, 2703-2706 (2014).
48. B. Hammer, J. K. Nørskov, Electronic factors determining the reactivity of metal surfaces. *Surface Science* **343**, 211-220 (1995).
49. X. Liang, C. Jiang, Atomic layer deposited highly dispersed platinum nanoparticles supported on non-functionalized multiwalled carbon nanotubes for the hydrogenation of xylose to xylitol. *J. Nanopart. Res.* **15**, 1890 (2013).
50. Z. Yan, M. Cai, P. K. Shen, Nanosized tungsten carbide synthesized by a novel route at low temperature for high performance electrocatalysis. *Sci. Rep.* **3**, 1646 (2013).
51. I. J. Hsu, Y. C. Kimmel, X. Jiang, B. G. Willis, J. G. Chen, Atomic layer deposition synthesis of platinum-tungsten carbide core-shell catalysts for the hydrogen evolution reaction. *Chemical Comunications* **48**, 1063-1065 (2012).
52. S. Zhang *et al.*, Monodisperse Core/Shell Ni/FePt Nanoparticles and Their Conversion to Ni/Pt to Catalyze Oxygen Reduction. *J. Am. Chem. Soc.* **136**, 15921-15924 (2014).
53. "Free market commodity prices, monthly, January 1960-June 2015," United Nations Conference on Trade and Development, (2015) http://unctadstat.unctad.org/wds/TableViewer/tableView.aspx?ReportId=28768

54. "Gold Price in a Range of Currencies since December 1978," The World Gold Council, (2015) https://www.gold.org/research/download-the-gold-price-since-1978
55. "Platinum, Palladium, Rhodium, Iridium, Ruthenium Monthly Average Prices between 01 Jun 1992 and 31 Jul 2015," Johnson Matthey, (2015) http://www.platinum.matthey.com/prices/price-charts
56. S. Rudi, C. Cui, L. Gan, P. Strasser, Comparative Study of the Electrocatalytically Active Surface Areas (ECSAs) of Pt Alloy Nanoparticles Evaluated by Hupd and CO-stripping voltammetry. *Electrocatalysis* **5**, 408-418 (2014).
57. J. K. Nørskov, F. Studt, F. Abild-Pedersen, T. Bligaard, *Fundamental concepts in heterogeneous catalysis*. (John Wiley & Sons, 2014).
58. Z. Jusys, J. Kaiser, R. Behm, Composition and activity of high surface area PtRu catalysts towards adsorbed CO and methanol electrooxidation: A DEMS study. *Electrochim. Acta* **47**, 3693-3706 (2002).
59. J. Durst, C. Simon, F. Hasche, H. A. Gasteiger, Hydrogen Oxidation and Evolution Reaction Kinetics on Carbon Supported Pt, Ir, Rh, and Pd Electrocatalysts in Acidic Media. *J. Electrochem. Soc.* **162**, F190-F203 (2014).
60. C. C. McCrory *et al.*, Benchmarking Hydrogen Evolving Reaction and Oxygen Evolving Reaction Electrocatalysts for Solar Water Splitting Devices. *J. Am. Chem. Soc.* **137**, 4347-4357 (2015).
61. D. V. Esposito *et al.*, Low-cost hydrogen-evolution catalysts based on monolayer platinum on tungsten monocarbide substrates. *Angew. Chem. Int. Ed.* **49**, 9859-9862 (2010).